

Contributions of the persistent sodium and M-type potassium currents in the
preBötzinger Complex for breathing rhythm generation

Carlos Aparecido da Silva Junior

Ribeirão Preto, São Paulo, Brazil

Master of Physiological Sciences, Universidade Federal de São Carlos, 2020

Bachelor in Biological Sciences, Universidade Estadual Paulista, 2017

A Dissertation presented to the Graduate Faculty of The College of William and
Mary in Virginia in Candidacy for the Degree of
Doctor of Philosophy

Department of Applied Science

The College of William and Mary in Virginia
August 2024

APPROVAL PAGE


This Dissertation is submitted in partial fulfillment of
the requirements for the degree of

Doctor of Philosophy



Carlos Aparecido da Silva Junior

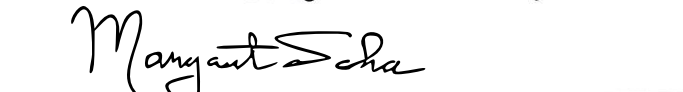
Approved by the Committee, June 2024



Committee Chair
Christopher A. Del Negro, Chancellor Professor, Applied Science
College of William & Mary



Gregory D. Conradi Smith, Professor, Applied Science
College of William & Mary



Margaret S. Saha, Chancellor Professor, Biology
College of William & Mary



Gordon S. Mitchell, Professor, Physical Therapy
University of Florida

COMPLIANCE PAGE

Research approved by

Institutional Animal Care and Use Committee

Institutional Biosafety Committee

Protocol number(s): IACUC-2021-04-20-14958-cadeln

IBC-2022-08-07-15768-mrdegu

Date(s) of approval: 2021-05-09

2023-08-07

ABSTRACT

Vertebrate animals execute different rhythmic motor behaviors such as walking, swallowing, and breathing, and the generation of that rhythmic activity is governed by central pattern generator network (CPGs), which do not require sensory feedback. The central nervous system is endowed with different CPGs responsible for determining the appropriate sequence of muscle activation that leads to the correct behavior expression.

Breathing is an essential rhythmic behavior and drives the gas exchange between the lungs and the ambient air. Unlike most CPGs that are episodic, and generally quiescent in resting conditions, the respiratory network is active continuously throughout life.

The normal breathing cycle is composed by two distinct phases: inspiration and expiration. Inspiration is the inexorable phase and happens due to the active recruitment of the diaphragmatic muscle, while expiration happens passively due to the elastic recoil of the diaphragm and thorax. The CPG for inspiratory activity is the preBöttinger complex (preBötC) in the lower brainstem, and it contains essential excitatory interneurons derived from neuronal progenitor cells that express the *developing brain homeobox 1 (Dbx1)* transcription factor. However, the ion channel mechanisms involved in initiating and terminating rhythmic burst activity *in vivo* remain unsolved. Here, I test the ion channels proposed to orchestrate both mechanisms.

The first chapter of my dissertation evaluates the “pacemaker theory” which suggests that some preBötC neurons express an intrinsic persistent sodium current (I_{NaP}) that gives rise to the voltage-dependent bursting-pacemaker activity, thus driving the inspiratory bursts. I knocked out and knocked down the *Scn8a* that codes for the sodium channel $Nav1.6$ which gives rise to I_{NaP} . I showed that pacemaker activity is no longer present in rhythmic slices of preBötC from neonatal mice; further, juvenile, and adult mice lacking this subunit still generate breathing activity.

The second chapter seeks to understand the role of the M-currents in inspiratory burst termination and opioid-induced respiratory depression. Previous experiments showed that pharmacological blockage of voltage-gated potassium channels from the $Kv7$ family prolongs bursts in a rhythmic slice model of breathing. Surprisingly, I found that genetic knockdown of *Kcnq2* and *Kcnq3* that comprise M-current does not alter ventilation, metabolism and breathing variability of adult mice.

I conclude that *Scn8a*-mediated $Nav1.6$ channels underlies I_{NaP} -driven pacemaker activity in rhythmic slices, and although it contributes to neuronal excitability in preBötC, this feature is dispensable for rhythm generation. Moreover, *Kcnq2/Kcnq3*-mediated $Kv7$ M-currents are not necessary for inspiration-expiration phase transition *in vivo*. These results contribute to understanding the role of specific ion channels in breathing control by using cutting-edge genetic tools, while avoiding unwanted side-effects observed in conventional pharmacological approaches. Moreover, this work shows the importance of whole animal models to understand the multifaceted origin of vital motor behaviors like breathing, which was a missing information not achieved with the use of reduced preparations in the context of ion channel mechanisms for breathing.

TABLE OF CONTENTS

Acknowledgements	iii
Dedications	v
List of Tables	vi
List of Figures	vii
Introduction	1
Chapter 1. Literature review	3
1.1. Historical recapitulation of breathing studies	3
1.2. Basics of breathing	6
1.3. preBötzinger Complex (preBötC) and inspiratory rhythm: physiological and anatomical characterization	12
1.4. Genetics identity of preBötC and the Dbx1 core hypothesis	19
1.5. How is the inspiratory breathing rhythm generated?	24
1.6. How is the inspiratory burst terminated?	34
1.7. References	42
Chapter 2. Role of Nav1.6-mediated persistent sodium current and bursting-pacemaker properties in breathing rhythm generation	55
2.1. Abstract	55
2.2. Introduction	56
2.3. Material & Methods	59
2.4. Results	74
2.5. Discussion	93
2.6. Supplementary Information	105
2.7. References	116
Chapter 3. Evaluating the role of KCNQ ion channels in breathing rhythmogenesis and opioid-induced respiratory depression in adult mice	123
3.1. Abstract	123
3.2. Introduction	124
3.3. Material & Methods	126
3.4. Results	142
3.5. Discussion	157
3.6. Supplementary Information	166

Vita	3.7. References	171
		179

ACKNOWLEDGEMENTS

Getting to the end of this 4-year journey was only possible because of presence of amazing people in my life. Here, I want to express my everlasting gratitude to those who contributed in so many ways for this work to be completed.

First, I want to express my appreciation to my advisor, Chancellor Professor Christopher Del Negro, under whose guidance this research was conducted. Thank you for welcoming in your lab in 2019 and giving me the opportunity to accomplish great things. It had never crossed my mind that one day I would pursue a Ph.D. in the United States. I evaluate our mentor-mentee relationship as very positive and I will be forever indebted to you for believing in me, and for seeing the potential for growth that I did not see. Thank you for your patience, motivation, and constructive criticism throughout this whole time.

I would also like to thank the people from Del Negro's Lab. Big thanks to Professor Maria Cristina (Tina) D. Picardo for her daily commitment to my success. Tina was always supportive; someone I could truly lean on during the hard moments. Thank you for letting me share my frustrations, but also share many moments of good laugh. Thank you for your valuable time and diligence in training me. Thanks to Cam Grover, Ph.D., Subhash Juneja, Ph.D., and Ayanna Limaye for managing the mouse colony. Special thanks to Ayanna and Eva Kalajian for being such great friends. Thanks to Tina Naik for collecting part of the results presented in the first chapter of this thesis.

I want to thank all the Applied Science staff and professors, and the staff from the Reves Center for helping me with the administrative duties and contributing to a better student experience. Special thanks to Rebecca Bliley who welcomed me every single morning and was always so thoughtful. You made each day worth to be in the department. I also wish to thank Chancellor Professor Margaret Saha and Professor Greg Conradi Smith for being part of my committee, and I am honored to have Professor Gordon Mitchell of the University of Florida (BREATHE Center) also evaluating my work.

There are many friends I would like to express my gratitude: those across the seas, back home, and the new ones I had the pleasure to have here. You have always supported, encouraged, and believed in me. Dan, Andrew and Nyckole, words can't express how proud I am to call you friends. You are the family I chose.

I want to take a moment to say thanks to Joshua Moberly. Having met you at this period of my life was incredible. You made the days lighter. Thank you for holding my hand and for believing on me when I couldn't do it myself. Thank you for welcoming me into your family.

My gratitude to Professor Luciane H. G. Batlhão, for she has always set me in the right direction, offering clever guidance. I have learned so much from you.

I owe my deepest gratitude to my parents and grandparents. Lucia Regina Miralha, Carlos Aparecido da Silva, Carlos Roberto da Silva, Francisca de Sales Marques da Silva, Aparecida do Carmo Borges Miralha, and José Oswaldo Borges Miralha. May your names be registered here so time will never forget you. Even knowing that you are not present for my commencement and my defense, I want to say: I did it. And I did it for each one of you. Your love is felt, and I will always carry it with me. I know that I made the decision of breaking new ground without you here, and the distance hurts. But I hope all of you are proud of who I am becoming.

This Ph.D. is dedicated to my parents and family, past and present advisors, friends,
and everyone who have helped me countless times along the way.

LIST OF TABLES

2.1. Linear regression of the ventilation (\dot{V}_E), tidal volume (V_T), respiratory frequency (f_R), air convection requirement ($\dot{V}_E/\dot{V}O_2$) oxygen consumption ($\dot{V}O_2$), inspiratory time (T_I), expiratory time (T_E), and inspiratory drive (V_T/T_I), of wild-type (Dbx1;Scn8a ^{+/+}), heterozygous (Dbx1;Scn8a ^{fl/+}), and homozygous (Dbx1;Scn8a ^{fl/fl}) mice.	83
2.2. Linear regression of the ventilation (\dot{V}_E), tidal volume (V_T), respiratory frequency (f_R), inspiratory time (T_I), expiratory time (T_E), and inspiratory drive (V_T/T_I), of adult mice injected with AAVs carrying non-targeting (control) and <i>Scn8a</i> -targeting shRNA in the preBötC.	92
3.1. <i>Kcnq2</i> expression decreases in glutamatergic preBötC neurons in <i>Kcnq2/Kcnq3</i> -knockdown mice.	144
3.2. <i>Kcnq3</i> expression decreases in glutamatergic preBötC neurons in <i>Kcnq2/Kcnq3</i> -knockdown mice.	145
3.3. Linear regression analysis shows no change in breathing measurements in <i>Kcnq2/3</i> -knockdown (<i>Kcnq2/3</i> -KD) mice.	146
3.4. Inspiratory and expiratory duration, as well as metabolism, do not change in <i>Kcnq2/Kcnq3</i> -knockdown (<i>Kcnq2/3</i> -KD) mice.	148
3.5. Respiratory drive as well as short- and long-term variability changes in <i>Kcnq2/Kcnq3</i> -knockdown (<i>Kcnq2/Kcnq3</i> -KD) mice.	151
3.6. High dose of fentanyl causes OIRD in wild-type mice.	153
3.7. Inspiratory time in control and <i>Kcnq2/Kcnq3</i> -knockdown (<i>Kcnq2/Kcnq3</i> -KD) mice increase in response to fentanyl.	156

LIST OF FIGURES

1.1.	Parasagittal view of the brainstem with dorsal and ventral respiratory column.	9
1.2.	Recordings <i>from en bloc</i> preparation.	12
1.3.	Respiratory motor pattern is perturbed after microsections of neonatal rat medulla <i>in vitro</i> .	14
1.4.	Slice preparation contains the rhythmic microcircuit for breathing.	15
1.5.	Somatostatin-positive preBötC glutamatergic neurons are also NK1R-positive but are not catecholaminergic.	19
1.6.	Spatial organization of postmitotic neurons from ventral progenitor domains of the developing neural tube.	21
1.7.	Dbx1 preBötC neurons are rhythmically active.	23
1.8.	Respiratory neurons in the ventral lateral medulla have distinct pattern of bursting activity.	25
1.9.	Inspiratory preBötC neurons have voltage-dependent bursting pacemaker activity.	28
1.10.	Computational diagram of brainstem respiratory circuits based on the ring model.	36
2.1.	Conditional knockout of Scn8a reduces INaP in glutamatergic preBötC neurons.	75
2.2.	Conditional knockout of Scn8a in glutamatergic neurons precludes pacemaker activity and slows but does not stop inspiratory rhythm.	78
2.3.	Scn8a expression and ventilation in Dbx1;Scn8a are diminished in conditional knockout mice during postnatal development.	81
2.4.	Scn8a-targeting shRNA decreases gene expression.	88
2.5.	Short-hairpin RNA (shRNA) injection in the preBötC does not affect the respiratory variables in unanesthetized adult Vglut2-ires-cre mice.	90

3.1.	shRNA decreases <i>Kcnq2/Kcnq3</i> expression in glutamatergic preBötC neurons.	143
3.2.	<i>Kcnq2/Kcnq3</i> knockdown does not affect breathing.	147
3.3.	Breathing phase and metabolism of <i>Vglut2-ires-cre</i> mice do not change after <i>Kcnq2/Kcnq3</i> knockdown.	149
3.4.	<i>Kcnq2/Kcnq3</i> diminution does not affect respiratory drive and breathing variability.	150
3.5.	Fentanyl causes respiratory depression.	155
3.6.	<i>Vglut2-ires-cre</i> mice only show OIRD at a higher dose of fentanyl.	157

Introduction

Breathing is a vital motor behavior executed by mammals to obtain oxygen necessary for their cellular metabolism as well as eliminate carbon dioxide and balance acid-base levels. The field of respiratory neurobiology is dedicated to unraveling the neural mechanisms underlying this bodily function. Therefore, my dissertation aims to explore the intricates of breathing control at the molecular level.

The first chapter provides a comprehensive literature review of the state of art on breathing control. Focusing on the preBötzinger complex (preBötC), I recapitulate the main findings that have led to our current understanding of how breathing rhythm is initiated, maintained, and terminated by its constituent neurons.

My second chapter presents the findings of my first project, which sought to understand the contributions of the persistent sodium current (I_{NaP}) for inspiratory breathing rhythm generation. My results challenge the long-standing “pacemaker theory” and shows that while I_{NaP} -driven pacemaker activity in preBötC neurons contributes to maintain excitability in the network, which is important for the normal progressive development of breathing *in vivo*, this mechanism is not obligatory for rhythm generation. These findings have already been published in a peer-reviewed journal: **da Silva Junior, C.A.**, Grover, C.J., Picardo, M.C.D., Del Negro, C.A. (2023). Role of Nav1.6-mediated persistent sodium current and bursting-pacemaker properties in breathing rhythm generation. *Cell Reports*, 42. <https://10.1016/j.celrep.2023.113000>.

The third chapter of this dissertation seeks to unravel the role of KCNQ2/KCNQ3-mediated M-currents in the preBötC for burst termination and opioid-induced respiratory depression (OIRD). I show that attenuation of this current *in vivo* does not cause alterations in the timing of inspiration or breathing cycles in general, neither does it prevent or blunt the respiratory depressant effects of the opioid agonist fentanyl. Although the data do not match those obtained in rhythmically active slice preparations containing the preBötC, I do not exclude the possible contribution of M-current on burst termination if higher levels of *Kcnq2/Kcnq3* knockdown are achieved, and its recruitment for OIRD at stronger doses of opioid agonists.

The results presented here provide new understanding of how attenuation of I_{NaP} - and KCNQ-driven mechanisms affect breathing control of neonate, young and adult mice. In the broader context of neural control of breathing, my work also highlights the complexity of translating *in vitro* findings to *in vivo* systems, emphasizing the importance of studying respiratory mechanisms in more physiologically relevant models. It also opens the possibility of exploring alternative synaptic and ion channel mechanisms for how the respiratory rhythm is generated, maintained, and terminated.

Chapter 1: Literature review

1.1. Historical recapitulation of breathing studies

Animals execute different type of motor behaviors, like swimming, walking, chewing, licking, and breathing. The expression of those complex motor behaviors presupposes the existence of cells that can initiate, maintain, and regulate them. Apart from the phylum Porifera, all other phyla, starting at Cnidaria, have a nervous system formed by neurons, its fundamental units, responsible for receiving sensory information and sending motor commands based on electrical signaling (Hill *et al.*, 2012; Liebeskind *et al.*, 2016). Although neurons are assembled in different anatomical structures across the Kingdom Animalia, it is precisely their organization as a functional nervous system that accounts for the complexity observed in animal's physiology and behavior (Hofman, 2012; Liebeskind *et al.*, 2016).

In fact, the behaviors expressed by those animals share similar neural underpinnings, since evolutionary trends point to changes in the complexity of organization of neurons into systems, i.e., with varying degrees of centralization and cephalization, rather than changes in the neurons themselves (Brown, 1914; Hill *et al.*, 2012; Hofman, 2012; Liebeskind *et al.*, 2016). Therefore, from invertebrates to vertebrates, rhythmic motor behaviors are generated by central pattern generator networks (CPGs) (Grillner, 2006; Grillner & El Manira, 2020). Likewise, breathing behavior is controlled by a CPG, whose characteristics are still under constant investigation (Feldman & Kam, 2015; Del Negro *et al.*, 2018; Ashhad *et al.*, 2022).

One could wonder why breathing is a vital physiological process to many animals. Moreover, why a person cannot hold their breath for too long? These questions seem to have always permeated the physiological and anatomical studies throughout the history because the notion of breathing as essential for homeostasis and life itself is old and present in different ancient western cultures. However, the understanding of breathing as a rhythmic process that supplies the body with oxygen necessary for energy production and removes the carbon dioxide produced from cellular metabolism is recent.

Somewhere around 2,000 to 4,000 years B.C., Egyptians, Chinese and Hindu practices already acknowledged the importance of proper breathing and its contributions to the overall body's health. Indeed, millennial practices like *paranayama* ("*prana*", from Sanskrit, means "breath", "vital energy") and *qigong* (from Chinese, means "cultivation of life energy") combine breathing exercises and body movements to bring vitality and healing to those who practice them (West, 2011; Fitzgerald & Cherniack, 2012). Catholic texts similarly bring the notion of breathing and life ("God's breath of life").

Even though much of the history of science was lost or not categorically documented, it is recognized that studies about the respiratory system and the cardiovascular system were always, somehow, associated. The first speculations between respiration and life originated among the Greeks, with Anaximenes and Erasistratus and their ideas about the "pneuma", proposing that air would reach the left ventricle of the heart and combine with the "vital spirit", and then distributed throughout the body. This "pneumatic" theory of respiration is

incorporated and modified by Galen's scheme for blood circulation and remained accepted for over 1,400 years (Fitzgerald & Cherniack, 2012). It is only during the sixteenth and seventeenth centuries that findings from Versalius, Eustachius, Michael Servetus, Marcello Malpighi and William Harvey will bring drastic changes and advancement to our understanding of anatomy and physiology, especially regarding the cardiovascular and respiratory systems (West, 2011; Fitzgerald & Cherniack, 2012).

Experiments from the Oxford Group composed by Robert Boyle, Robert Hooke, Richard Lower and John Mayow exposed animals to reduced air pressures in a chamber, and the results contributed to the idea that air contains a "life-giving" substance needed for life. Nonetheless, it is Antoine Laurent Lavoisier who will later describe the three respiratory gases (oxygen, carbon dioxide, and nitrogen), motivated by experiments from Joseph Priestley who heating red mercuric oxide was able to release "*a gas that caused a candle to burn with a vigorous flame*", and showed that a mouse could survive longer while breathing this air (Fitzgerald & Cherniack, 2012).

Lavoisier provided great contributions to the chemistry developed during the 18th century. With his discovery of an "*eminently respirable air that enters the lung*", he created the term "*oxygine*", which means "acid-producer". Moreover, performing calorimetric experiments with Laplace, they started studying the relationships between combustion and respiration, which led to the idea of a metabolism in animals. Later findings from Lazzaro Spallanzani aids to these

theories by concluding that oxidation and heat production happens in the tissues (West, 2011; Fitzgerald & Cherniack, 2012).

By the end of the 18th century, there was considerable amount of accurate information on the gases of respiration. However, it is only in the 19th century that Le Gallois provides the experimental evidence in rabbits that a region in the medulla near the origin of the vagus nerve was the place for controlling ventilation (Le Gallois, 1812; Fitzgerald & Cherniack, 2012; Cheung, 2013).

Subsequent experiments, also in rabbit, by Flourens using sectioned spinal cord showed that the diaphragm was paralyzed, but mouth and glottis continued rhythm movement, after sectioning was made at the level of the cervical region (Fitzgerald & Cherniack, 2012). Although unknown at that time, it is important to note that the section at the cervical region of rabbits was likely cutting the cranial nerve IV, that innervates the diaphragm, but preserved the cranial nerve XII, that innervates the upper airways.

Even though technical limitations made it difficult to localize the precise region in the medulla generating the breathing rhythm, these two aforementioned findings foretell what contemporary scientists found in ventral respiratory column, in particular and the preBötzinger complex in the ventrolateral medulla.

1.2. Basics of breathing

Progress in science often requires the existence of specific techniques that help the investigators to study a phenomenon, which could not be approached

otherwise. An example is breathing studied *in vitro*. It is only in the 1980's that researchers were able to isolate the brainstem and the spinal cord from newborn rodents in one single preparation, called *en bloc* preparation, preserving cranial and spinal nerves. This brainstem-spinal cord (*en bloc*) preparation, along with thorax, remained rhythmically active *in vitro* while bathed in oxygenated solutions that mimicked the cerebrospinal fluid (Suzue, 1984).

However, before diving into these findings that led to the description of the preBötC, it is important to define a few concepts.

Breathing is a rhythmic process spontaneously initiated in the brainstem. Its main function is to supply the oxygen that will be used in biochemical reactions to produce energy, remove the carbon dioxide produced from cellular metabolism, as well as to balance pH, i.e., the acid-base levels in circulation and in interstitial spaces, including those in the brain and central nervous system.

In mammals, one normal breathing cycle (which is referred to as eupnea, or eupneic breathing) is composed of three phases: inspiration, post-inspiration, and expiration (Bianchi *et al.*, 1995). Inspiration is the preeminent and inexorable phase of this cycle, involving the active contraction of inspiratory pump muscles such as the diaphragm and external intercostal muscles. This phase ventilates the lungs, bringing in the oxygen from outside. Post-inspiration is a conditional phase (i.e., not always present), where concentric contraction of pharyngeal muscles work to slow the releasing of the air from the lungs, combined with eccentric or lengthening contraction of the diaphragm, prolonging gas exchange.

Expiration is the final phase of the breathing cycle, and contrary to inspiration that is always active, expiration can be either passive or active (Pagliardini *et al.*, 2011; Huckstepp *et al.*, 2015), depending on metabolic demand. At rest, expiration occurs passively due to the elastic recoil of inspiratory muscles, as well as the lungs and rib cage in series. However, it becomes active during exercise or when the environmental concentration of CO₂ rises. In those cases, internal intercostals muscles, obliques, rectus abdominis and transversus abdominis are recruited (Huckstepp *et al.*, 2015; Silva *et al.*, 2016; de Britto & Moraes, 2017; Leirão *et al.*, 2018).

The CPG for breathing in the brainstem contains functionally divisible areas that comprise rhythmogenic constituents that drive other motor pattern-forming components (Fig. 1.1). These oscillators initiate and shape the rhythm and the motor pattern of each breath to meet metabolic, biomechanical, and behavioral goals. In a rostral-caudal orientation, at the ventral portion of the brainstem, the Bötzing Complex (BötC), preBötzing complex (preBötC), the rostral ventral respiratory group (cVRG) and the caudal ventral respiratory group (cVRG) make up the Ventral Respiratory Column. Other regions like the postinspiratory complex (PiCo) and the parafacial region (pF) are found adjacent to the ventral respiratory column. On the other hand, the Dorsal Respiratory Column contains the nucleus of the solitary tract (NTS) (Smith *et al.*, 2013; Del Negro *et al.*, 2018).

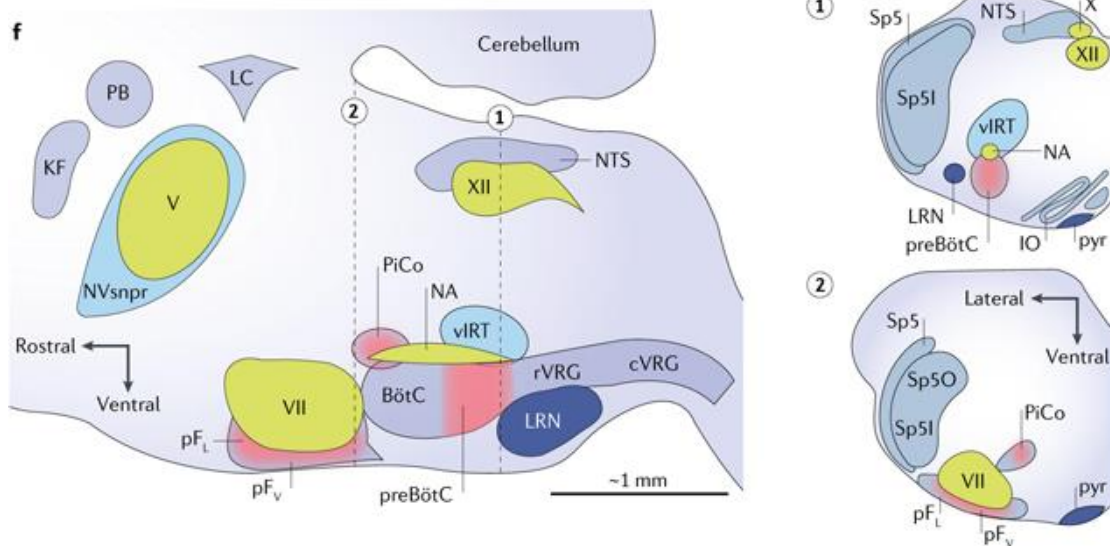


Figure 1.1 – Parasagittal view of the brainstem with dorsal and ventral respiratory column. On the left, known pontine and medullary sites involved in breathing rhythm and pattern formation. Respiratory oscillators (i.e., rhythmogenic sites) are colored in red, whereas cranial motor nuclei involved in controlling airway resistance are shown in yellow. On the right, (1) and (2) insets are transverse sections at the level of the preBötC (dotted line 1) and pF (dotted line 2). preBötzinger Complex (preBötC), parafacial lateral (pFL) and ventral (pFV), postinspiratory complex (PiCo), ventral intermediate reticular formation (vIRT), trigeminal principal sensory nucleus (NVsnpr), hypoglossal motor nucleus (XII), nucleus *ambiguus* (NA), facial motor nucleus (VII), trigeminal motor nucleus (V), rostral ventral respiratory group (rVRG), caudal ventral respiratory group (cVRG), Kölliker-Fuse nucleus (KF), parabrachial nucleus (PB), nucleus of the solitary tract (NTS), Bötzing Complex (BötC), *locus coeruleus* (LC), lateral reticular nucleus (LRN), spinal trigeminal (Sp5), spinal trigeminal sensory nucleus *oralis* (Sp5O) and *interpolaris* (Sp5I), inferior olive (IO), pyramidal tract (pyr). From (Del Negro et al., 2018).

As more attention will be given to inspiratory oscillator, the preBötC, later in this document, it is worthy to comment on PiCo and the pF briefly.

Recently in the history of neurophysiology, PiCo was proposed as an independent oscillator, sufficient and necessary for generating the postinspiratory phase of the respiratory cycle (Anderson *et al.*, 2016; Huff *et al.*, 2023). This region contains interneurons located within the intermediate reticular nucleus and they express markers for glutamatergic and cholinergic transmitter phenotype. Neurons within PiCo are modulated by somatostatin (SST) and opioids, and they

are sensitive to noradrenaline. PiCo is suggested to be a hub in the ventral respiratory column that integrates and mediates laryngeal postinspiratory motor output, and its activity is coordinated with preBötC in a mutually inhibitory configuration (Anderson *et al.*, 2016; Huff *et al.*, 2022, 2023). Bilateral optogenetic activation of this region during inspiration or at the beginning of postinspiration triggers swallowing in anesthetized mice (Huff *et al.*, 2023). Besides of coordinating swallow and breathing, *in vivo* optogenetic stimulation of cholinergic-glutamatergic PiCo neurons increases sympathetic activity in a respiratory phase-dependent manner, suggesting that this region also contributes to respiratory-sympathetic coupling in mice (Karlen-Amarante *et al.*, 2024).

Although there is still debate regarding their distinction, it is proposed that the pF region can be further divided into parafacial ventral (pF_V) and parafacial lateral (pF_L), due to their discrete function and location relative to the facial cranial motor (VII) nucleus. The pF_V, also referred to as the retrotrapezoid nucleus (RTN) (Smith *et al.*, 1989; Nattie & Li, 1995), is a chemosensitive site involved in detecting changes in the CO₂/pH, promoting adjusts in the hypercapnic ventilatory responses (Mulkey *et al.*, 2004; Stornetta *et al.*, 2006; Guyenet & Bayliss, 2022). This area sends excitatory projections to the preBötC to increase the respiratory frequency in situations of high metabolic demand. Its neurons are glutamatergic and express the paired-like homeobox 2B (*Phox2b*) and the atonal homologue 1 (*ATOH1*) genes (Stornetta *et al.*, 2006; Guyenet *et al.*, 2010; Ramanantsoa *et al.*, 2011; Ruffault *et al.*, 2015; Guyenet & Bayliss, 2015, 2022).

The pFL, along with preBötC, makes up for the dual oscillator hypothesis (Mellen *et al.*, 2003; Janczewski & Feldman, 2006; Huckstepp *et al.*, 2015, 2016). While the preBötC is proposed to generate inspiratory rhythm (Smith *et al.*, 1991), the pFL oscillator gives rise to the late expiratory phase (Onimaru & Homma, 2003; Pagliardini *et al.*, 2011; Souza *et al.*, 2020), and its neurons project to expiratory premotor neurons in the caudal ventral respiratory group, which further supports this role (Silva *et al.*, 2016; Del Negro *et al.*, 2018). Since expiration happens passively, it is suggested that its neurons are silent at rest due to inhibitory neurotransmission, but once disinhibited, they can trigger the active expiration (de Britto & Moraes, 2017; Leirão *et al.*, 2018; Flor *et al.*, 2020). Thus, the pFL is a conditional rhythmic oscillator, whose function is tightly coordinated with preBötC and is state dependent (i.e., more active expiration events occur during REM sleep) (Leirão *et al.*, 2018). In fact, the pF and preBötC neurons emerge independently during the embryonic development, but their dual organization is established at the time of the onset of fetal breathing (Onimaru & Homma, 2003; Janczewski & Feldman, 2006; Pagliardini *et al.*, 2011).

Even though the post-inspiration and expiration are controlled by distinct areas in the brainstem, those regions seem to be in coordination with the “master” inspiratory oscillator, the preBötC. Other orofacial behaviors are also coordinated with inspiration to prevent incompatible co-activation of common muscles (Moore *et al.*, 2013, 2014; Kleinfeld *et al.*, 2014). Therefore, as the inexorable and only unconditional active phase of the breathing cycle, the discovery of the underlying

neural mechanisms for inspiratory rhythm generation is a significant topic in the field of the respiratory neurobiology.

1.3. preBötzinger Complex (preBötC) and inspiratory rhythm: physiological and anatomical characterization

Using newborn rodent pups, researchers isolated the brainstem and the spinal cord, along with thorax and cranial and spinal nerve rootlets (Suzue, 1984). This preparation contained the rhythm-generating network, and respiratory-like movements from the thorax, measured using a strain gauge, were recorded in synchrony with motor output activity from phrenic nerve, measured with suction electrodes at C3-C5 roots, suggesting that the motor activity observed corresponded to inspiratory rhythm, because this nerve sends motor information to the diaphragm, leading to its contraction during the inspiratory phase.

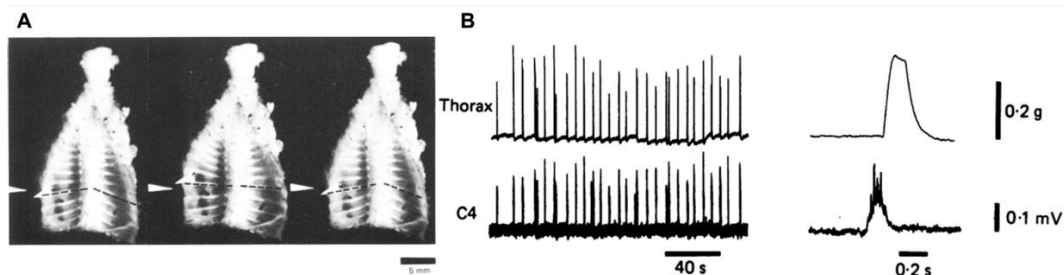


Figure 1.2 – Recordings from *en bloc* preparation. (A) Photographs of the brainstem-spinal cord preparation with thorax attached showing contraction of the intercostal muscles, i.e., respiration-like rhythmic movement of the thorax. Upward dotted lines indicate inspiration-like movements and flat dotted line indicate passive recoil of thorax (expiration). (B) Top trace on the left shows recording of the movements of thorax (monitored by measuring the tension from the distal end of the rib), whereas bottom trace on the left represents electrical activity of ventral root of cranial nerve IV (C4, recorded using a suction electrode). Traces on the right are expanded recording of one single event from the thorax (top) and C4 (bottom). Adapted from (Suzue, 1984).

Having established that inspiratory rhythm is generated in the brainstem, and can be studied *in vitro*, the next step was to identify and localize the specific oscillator region of the brainstem, i.e., the site where the inspiratory rhythmic activity originates.

Using a classical “take it out” methodology, researchers performed serial transections of the brainstem (75 μm -thick cumulative sections removed, Figure 1.3), in rostral to caudal direction (Smith *et al.*, 1991). When sections crossed a critical point of the brainstem, instability and perturbations were observed in the respiratory-like rhythm, up to the point where the phrenic motor discharge was completely eliminated. This experiment indicated that the neurons essential for rhythmogenesis are in the ventral medulla, about 350 μm caudal to the VII nucleus, at the level of the obex (the caudal end of the fourth ventricle). This region was named preBötzinger Complex (preBötC); it was postulated to contain the core oscillator for inspiratory rhythm (Smith *et al.*, 1991). It is worth noting that although the name for this region was bestowed by Smith and colleagues, it corresponds to the anatomical location identified by Flourens, as mentioned above, who used preparations from rabbits and the VIII cranial nerve as a landmark. That is, the description by Flourens, in ~1860, in rabbit is consistent with the region identified by Smith and colleagues in newborn rats, although clearly Smith *et al.* were more precise with boundaries as they localized the preBötC to the ventral and lateral region of the brainstem, immediately ventral to the nucleus *ambiguus* (which Flourens did not do).

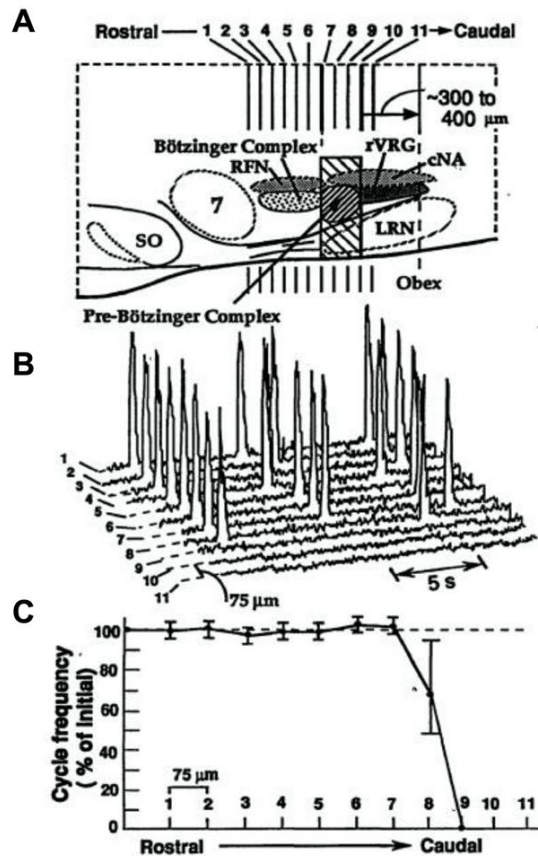


Figure 1.3 – Respiratory motor pattern is perturbed after microsections of neonatal rat medulla in vitro. (A) Parasagittal view of brainstem showing preBötzing complex (preBötC) and adjacent areas. Lines 1 to 11 represent 75 µm-thick serial sections performed in the rostral-caudal orientation. Sections from 7 to 10 contains the preBötC. Superior olive (SO), facial nucleus (7), lateral reticular nucleus (LRN), retrofacial nucleus (RFN), rostral ventral respiratory group (rVRG), caudal (semicompact) division of nucleus *ambiguus* (cNA). **(B)** Traces of C4 discharge at the level of each section. Discharges remained unaltered after sections made from the level of facial nucleus to preBötC. Sections 8 to 10 at the level of preBötC eliminated rhythmic motor output of spinal and cranial nerves. **(C)** Cycle frequency of nerve discharge after serial microsections. Adapted from (Smith *et al.*, 1991).

In further experiments, the authors were able to isolate a transverse medullary section of 500 µm thickness (Figure 1.4), containing the complete rhythmic motor microcircuit, with rhythmogenic interneurons, premotor neurons, and hypoglossal (XII) motor neurons as well as the axons that form the XII nerve (Smith *et al.*, 1991). Using this preparation, it was observed that intracellular recordings from

the preBötC and suction recordings from the XII nerve rootlets were synchronized, consistent with inspiratory rhythms being generated in the preBötC, and then communicated to XII motoneurons to produce nerve bursts of motor output.

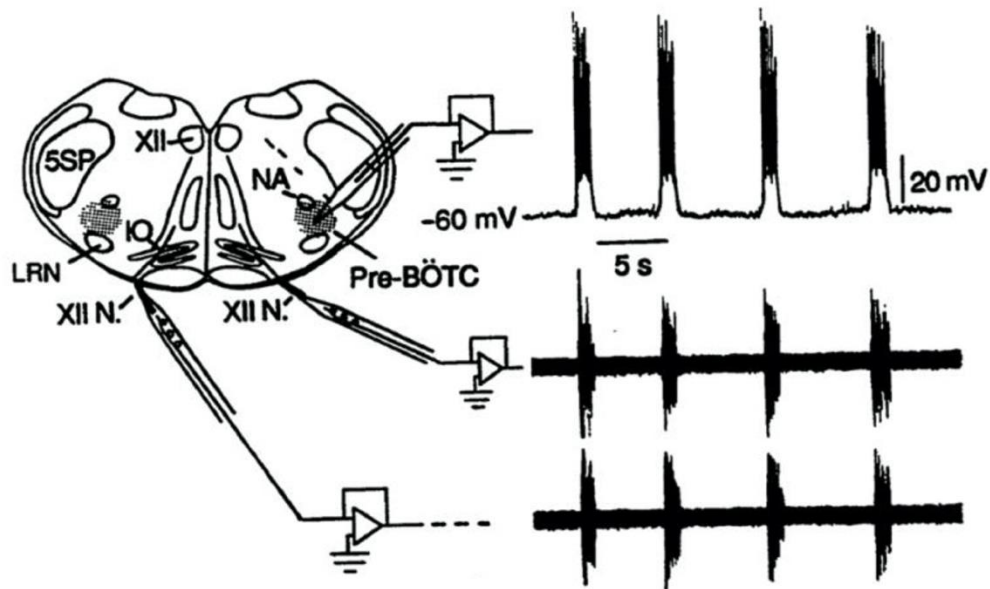


Figure 1.4 – Slice preparation contains the rhythmogenic microcircuit for breathing. 500 μm -thick medullary slice with preBötC (shaded region) shows neuron rhythmic activity from patch-clamp recording synchronized with motor output from cranial nerves. Upper right traces display whole-cell patch-clamp recordings from a rhythmically active preBötC neuron. Middle and lower right traces show respiratory motor discharge recorded bilaterally from hypoglossal nerve roots. nucleus *ambiguus* (NA), spinal trigeminal nucleus (5SP), hypoglossal nucleus (XII), hypoglossal nerve (XII N.), and inferior olive (IO). From (Smith *et al.*, 1991).

Further experiments demonstrated that the preBötC was an essentially rhythmogenic region rather than an area that only contained fibers of passage from a remote rhythmogenic site located elsewhere. These two opposing views were tested by local perturbations in the preBötC. Local application of K^+ (25 mM) in this area depolarized its neurons and increased XII frequency. Conversely, pharmacological blockage of excitatory neurotransmission

transiently slowed and then reversibly eliminated XII rhythmic activity. If the preBötC had been merely a link, then injection of K^+ or synaptic blockade would not have modified rhythmic frequency.

Experiments performed earlier in 1990 had previously mapped the existence of different populations of neurons in the brainstem according to their discharge pattern related to phrenic (C4) motor output. Late expiratory and biphasic expiratory neurons were found, but they were unlikely the source of the inspiratory rhythm because they remained silent during the inspiratory activity of C4. The authors also found a putatively specialized population of neurons that had a pre-inspiratory pattern, discharging before and during the C4 output, and they found a population with just inspiratory activity, discharging only during the C4 activity. The pre-inspiratory and inspiratory populations were thought to be specialized for generating and transmitting the inspiratory rhythm to premotor and motor neurons for inspiratory breathing movements. Even though those neurons were found across the ventral respiratory column, a higher concentration of the pre-inspiratory population matched with preBötC's location, and in parallel, the pre-inspiratory neuron type was not found in adjacent regions like the rVRG caudally, or the predominantly expiratory region Bötzing complex rostrally (Smith *et al.*, 1990). Three important conclusions can be made at this point: the preBötC is specialized in terms of its constituent neurons and their electrical phenotype; the preBötC is inspiratory rhythmogenic; and the preBötC can be studied in slice preparations *in vitro* which retain its rudimentary rhythm- and pattern-generating functionality.

To this point in the history of preBötC studies, the definition of the region and its borders (and constituent neurons) was solely a functional definition. A new frontier for the field of respiratory neurobiology was to discover the set of neuropeptides and neurotransmitters that were involved with modulating preBötC activity, and fortuitously, defining its anatomical boundaries and constituent neuronal identity.

The recognition of importance of the excitatory neurotransmitters for signaling in the preBötC was made using *in vitro* neonatal rat medullary slices and genetic deletion of the vesicular transporter for glutamate. First, in 1993, researchers were able to show that rhythm generation depends on excitatory amino acids, such as glutamate, by blocking non-*N*-methyl-*D*-aspartate (non-NMDA) in slice preparations, which decreased frequency and amplitude of XII nerve bursts (Funk *et al.*, 1993). Later in 2006, it was shown that mutant mice lacking the vesicular glutamate transporter 2 (*Vglut2*, it packages glutamate into the presynaptic vesicles) died after birth because they failed to generate a breathing rhythm. The authors proposed that the neurons in the preBötC did not engage synchronous activation, thus glutamate-mediated signaling is an obligatory component of the rhythm generator (Wallén-Mackenzie *et al.*, 2006).

Histological experiments complemented to the findings that preBötC was formed by glutamatergic neurons, and its neurons expressed neurokinin-1 receptors (NK1R) and μ -opioid receptors (μ ORs). Those receptors modulated rhythm as application of μ ORs agonists, such as DAMGO, and Substance P, an endogenous NK1R ligand, was able to decrease and increase the XII rhythm in

slice preparations, respectively (Gray *et al.*, 1999). Later, it was found that somatostatin (SST) expression also marks the preBötC region, as well the suppression of the activity of SST-expressing neurons in rats resulted in persistent apnea and the animals do not breath without mechanical ventilation (Stornetta *et al.*, 2003; Tan *et al.*, 2008). Immunohistochemistry of that area additionally revealed that SST-expressing neurons in the preBötC are also NK1R-positive, but respiratory glutamatergic neurons in the ventral respiratory column are not catecholaminergic neurons from the C1 region, which are associated with autonomic functions (Stornetta *et al.*, 2003; Kvetnansky *et al.*, 2009). The main conclusion at that point was that, although the preBötC borders were fuzzy, some peptide receptors are useful markers that help to delineate it and may help to identify its constituent rhythmogenic neurons.

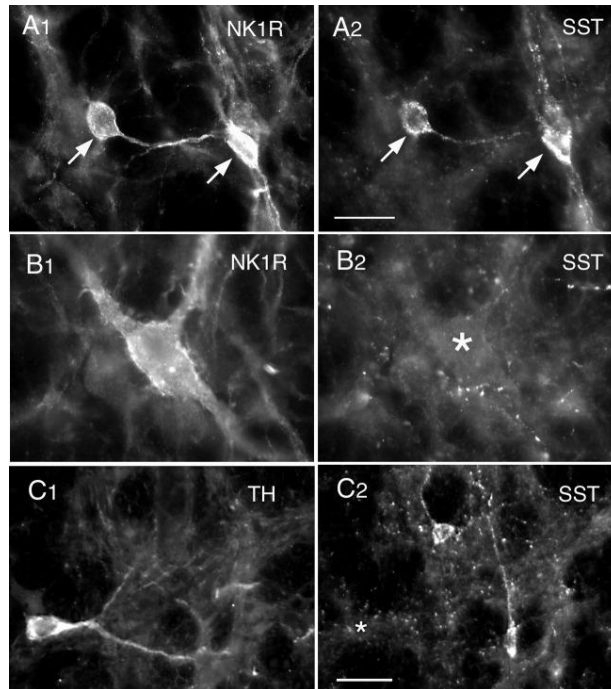


Figure 1.5 – Somatostatin-positive preBötC glutamatergic neurons are also NK1R-positive but are not catecholaminergic. (A) Immunohistochemistry for neurokinin-1 receptors (NK1R) co-localizes with somatostatin-positive preBötC neurons. (B) Some NK1R-positive preBötC neurons are not somatostatin-positive. (C) Immunohistochemistry for Tyrosine Hydroxylase (TH), a marker for catecholaminergic neurons, does not co-localize with somatostatin-positive preBötC neurons in the ventral respiratory column. Arrows point to double-labeled cells, and asterisks indicate absence of double labelling. From (Stornetta *et al.*, 2003).

1.4. Genetics identity of preBötC and the Dbx1 core hypothesis

Peptides and peptide receptors are good, but imperfect, markers for the preBötC.

Given the powerful techniques offered by molecular genetics, an emerging question pertained to whether there any developmental molecular-genetic markers that give rise to rhythmogenic preBötC neurons?

Mammals, as well all other vertebrates, have their brains sharing a common structural organization, presenting three major anterior-posterior divisions: forebrain, midbrain, and hindbrain (Hill *et al.*, 2012). The last contains the medulla where the preBötC is found. At the embryonic states, the neural tube,

which will give rise to the nervous system, comes from the ectoderm tissue, and it shows a highly organized topology with distinct neuronal subtypes generated in a specific order along its dorso-ventral axis (Ribes & Briscoe, 2009). Thus, the neural tube is divided into ventral and dorsal portions according to the expression of sonic hedgehog (SHH, expressed at the floor plate) and bone morphogenic protein (BMP, expressed at the roof plate) signaling molecules, respectively (Briscoe *et al.*, 1999; Alaynick *et al.*, 2011). The expression of those two molecules defines two important classes of transcription factors that will give rise to different cell lineages in the developing neural tube. However, only the ventral portion will be considered here since it leads to the development of motor and autonomic functions.

The expression of SHH protein occurs only from the floorplate, thus the SHH concentration in the neural tube appears in a graded fashion (lower concentrations moving dorsally from floorplate), and that gradient determines canonical pattern of cells in the dorsal-ventral axis of the developing neural tube of vertebrates. The SHH stimulates the Class II of transcription factors and inhibits the Class I, and both classes are mutually inhibitory to one another. These interactions define the borders between the progenitor (p) domains p0, p1, p2, pMN (motor neurons) and p3, in a dorsal to ventral orientation (Ribes & Briscoe, 2009). Post-mitotically, cells from those domains will become V0, V1, V2, MN and V3 neuron populations with sealed fate. As an integral part of regulating the spatial organization of those progenitor domains, the signaling from SHH proteins also establishes the expression profile of various transcription

factors, including *Nkx2.2*, *Olig2*, *Nkx6.1*, *Nkx6.2*, *Dbx1*, *Dbx2*, *Irx3*, *Pax6*, and *Pax7*, some of which – but not all – are class I and II transcription factors (Ribes & Briscoe, 2009).

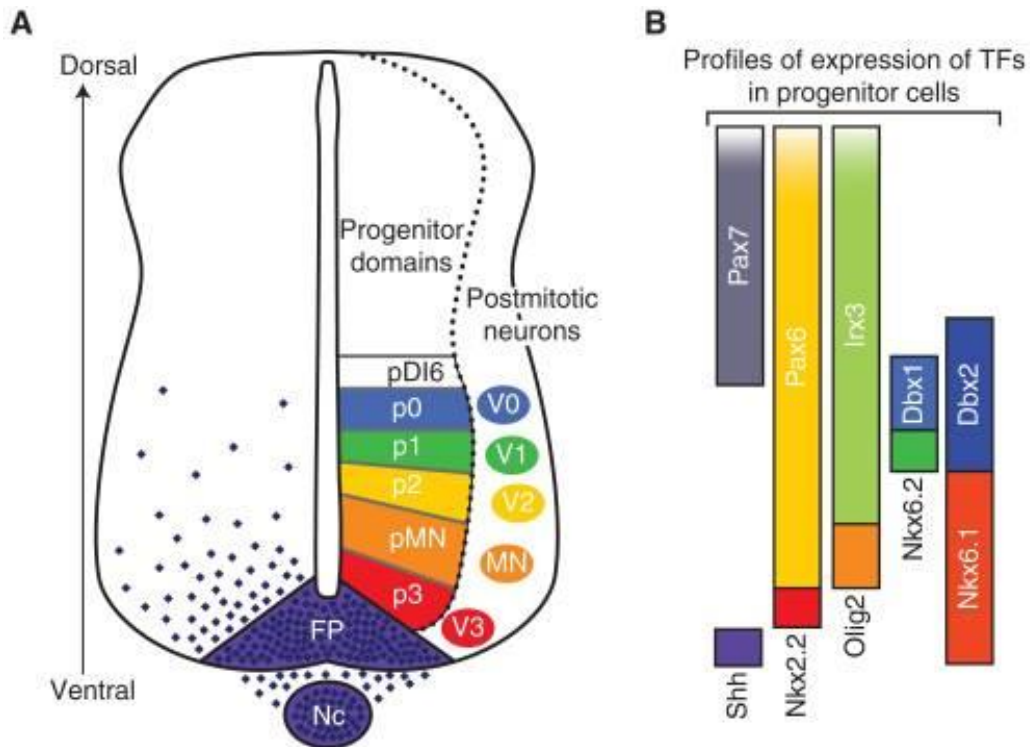


Figure 1.6 – Spatial organization of postmitotic neurons from ventral progenitor domains of the developing neural tube. (A) Six domains of progenitor (p) cells, FP (floor plate), p3, pMN (motor neuron), p2, p1, and p0, organized along the dorsal-ventral axis of the neural tube. Each domain generates a distinct subtype of postmitotic neurons (V0–V3) or motor neurons (MN). Sonic hedgehog (SHH) signaling protein (purple dots) is secreted from the notochord (Nc) and FP. **(B)** Each progenitor cell expresses a specific combination of transcription factors (TFs), including *Nkx2.2*, *Olig2*, *Nkx6.1*, *Nkx6.2*, *Dbx1*, *Dbx2*, *Irx3*, *Pax6*, and *Pax7*. Each TF is color-coded with respect to its determinant population. Note *Dbx1* (light blue) is determinant of V0 postmitotic neurons. From (Ribes & Briscoe, 2009).

The V0 post-mitotic neuron population is defined by the expression of the transcription factor *developing brain homeobox 1* (*Dbx1*), and *Dbx1*-derived neurons of the V0 dorsal (V0_D) population are GABAergic (Gray, 2013; Revill *et al.*, 2015), while in the ventral (V0_V) they express the vesicular glutamate

transporter 2 (*Vglut2*), giving rise to glutamatergic neurons (Lanuza *et al.*, 2004; Garcia-Campmany *et al.*, 2010; Alaynick *et al.*, 2011).

It is known that the ~98% of all the glutamatergic interneurons in the preBötC is derived from embryonic precursors that express *Dbx1* during embryonic days 9.5-12.5 (Bouvier *et al.*, 2010; Gray *et al.*, 2010; Kottick *et al.*, 2017; Wu *et al.*, 2017). In 2001, Pierani *et al.* showed that *Dbx1*-knockout mice, studied in the context of spinal cord research, did not breathe, and have a cyanotic appearance, and thus die at birth (Pierani *et al.*, 2001). According to the “*Dbx1* core hypothesis”, the *Dbx1*-derived preBötC interneurons (henceforth just *Dbx1* neurons) constitute the rhythm-generating core for mammalian inspiratory rhythm (Bouvier *et al.*, 2010; Gray *et al.*, 2010). This hypothesis is further supported by different testable predictions.

The first testable prediction proposes that *Dbx1* interneurons must be rhythmically active (Bouvier *et al.*, 2010; Gray *et al.*, 2010). Using Cre-Lox recombination to produce intersectional *Dbx1*^{CreERT2};*Rosa26*^{tdTomato} mice, i.e., *Dbx1* neurons are colored in red, researchers were able to show that these cells are rhythmically active in slice preparation containing the preBötC (Bouvier *et al.*, 2010; Gray *et al.*, 2010; Picardo *et al.*, 2013).

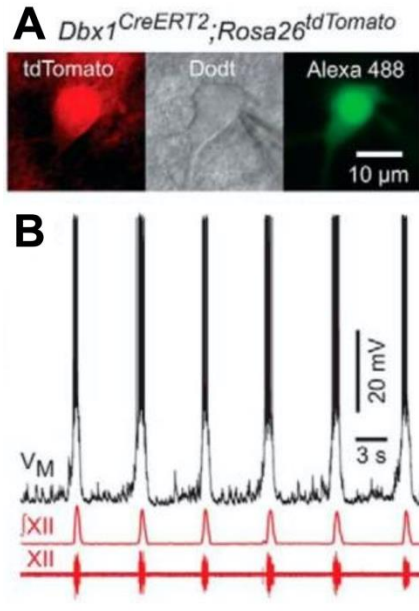


Figure 1.7 – Dbx1 preBötC neurons are rhythmically active. (A) From left to right, microscopic images from *Dbx1^{CreERT2};Rosa26^{tdTomato}* mouse slices show the expression of the reporter (tdTomato) in a Dbx1 neuron, the contrast microscopy (Dapi), and Alexa Fluor 488 introduced via patch pipette. **(B)** Whole-cell patch-clamp recordings show inspiratory bursts (top black trace) in the Dbx1 preBötC neuron in synchrony with XII motor output from field recordings (red traces). Middle trace is the signal integrated from XII raw signal shown at the bottom traces. Adapted from (Kottick & Del Negro, 2015).

The second testable prediction proposed that silencing or killing Dbx1 interneurons would perturb or stop breathing rhythm. This was proved to be the case when laser ablation of ~85 Dbx1 preBötC interneurons decreased the respiratory-like rhythm in slices and led to a reduction of the amplitude (Wang *et al.*, 2014) amplitude. Moreover, experiments carried out using slice preparation (Vann *et al.*, 2016) and adult mice (Vann *et al.*, 2018), showed that photoinhibition of Dbx1 interneurons decreased breathing frequency and amplitude in mice expressing archaerhodopsin, a light activated electrogenic proton pump that produces outward hyperpolarizing current when stimulated by orange light.

Conversely, the third testable prediction anticipated that stimulating Dbx1 interneurons would accelerate inspiratory rhythm. Here, authors stimulated Dbx1 preBötC neurons with blue light in animals expressing channelrhodopsin (ChR2), a light-activated ion channel that depolarizes the neuron in response to wavelengths of light in the blue range. It was observed that the rhythm sped up the XII frequency in slice preparation (Kottick & Del Negro, 2015). Photostimulation also sped up the rhythm and increased ventilation in unanesthetized and lightly sedated adult mice expressing ChR2 in Dbx1 preBötC neurons (Vann *et al.*, 2018)

Heretofore, the framework of scientific evidence showed that the preBötC contains rhythmogenic and pattern (output) related neurons, and those populations of neurons are derived from Dbx1- expressing progenitor cells (p0 and V0). Besides, speeding or slowing the rhythm are strong evidence of the role of that region in rhythmogenesis. However, even though the “Dbx1 core hypothesis” seems to be rational to explain inspiratory rhythm generation, other compelling theories are also suggested.

1.5. How is the inspiratory breathing rhythm generated?

1.5.1. Role of Inhibition

There are different populations of neurons throughout the ventral respiratory column, and they are classified according to their firing patterns regarding the C4 activity, such as early-inspiratory (early-I) (Smith *et al.*, 1990, 1991, 2007). The

pre-I neurons sometimes have a bursting-pacemaker activity. Inspiratory neurons then project to premotor neurons that in turn project to phrenic motoneurons in rostral ventral respiratory group (rVRG), driving the phrenic output, as well as XII motoneurons in the reticular formation that drive airway and tongue movements during inspiration (Revill *et al.*, 2015). In this scenario, pre-I neurons were putative candidates for rhythmogenesis as they presented a bursting pre-inspiratory activity (i.e., their bursts preceded C4 motor output), and bursts during C4 activity.

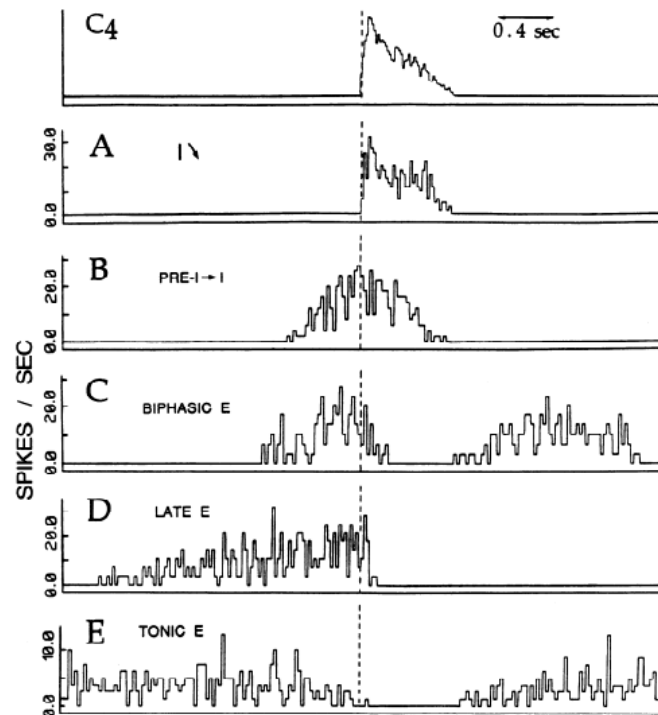


Figure 1.8 – Respiratory neurons in the ventral lateral medulla have distinct pattern of bursting activity. Cycle-triggered average histogram of (A) inspiratory (I), (B) pre-inspiratory (pre-I), (C) biphasic expiratory (biphasic E), (D) late expiratory (late E), and (E) tonic expiratory (tonic E) neurons. Their temporal discharge is shown in relation to motor output from the phrenic nerve (C4). Vertical dashed line in all panels indicates the onset of C4 activity. From (Smith *et al.*, 1990).

Motivated by observations from CPGs controlling rhythmic movements in invertebrates (Stuart & Hultborn, 2008; Grillner & El Manira, 2020), it was suggested that reciprocal inhibition between neurons in the ventral respiratory column would be the rhythmogenic mechanism for breathing (Burns, 1963; Richter *et al.*, 1992; Smith *et al.*, 2007; Rubin *et al.*, 2009; Feldman *et al.*, 2013; Marchenko *et al.*, 2016). This “inhibitory ring” model, analogous to locomotor “half-center” models, proposed that three distinct neuronal populations, one present in the preBötC and two in the BötC, sequentially inhibit each other. Here, enough regenerative inspiratory activity would exceed a threshold and trigger inhibition to terminate inspiration, and that inhibition would consecutively decrease, and a subsequent increment in the activity of excitatory inspiratory neurons would lead to the next cycle. That is, inhibition coming from expiratory neurons (aug-E and post-I) in the BötC terminates one inspiratory burst, enabling the network to generate the next inspiratory burst. Here, the system resets itself and inhibition transforms a subpopulation of excitatory preBötC neurons (pre-I), presumed to be tonically active, into an inspiratory-modulated one (Rubin *et al.*, 2009; Molkov *et al.*, 2010; Feldman *et al.*, 2013). This pre-I population has excitatory neurons with I_{NaP} -dependent endogenous bursting properties, which will be discussed later. The ring model is further supported by findings from *in vitro* and *in situ* preparations (Dutschmann & Paton, 2002; Smith *et al.*, 2007).

However, this mechanism does not seem to be the source of inspiratory rhythmogenesis in the preBötC, neither does it contribute to inspiratory burst termination. The ring model assumes that removal of inhibition should produce

apnea, however *in situ* preparation experiments showed that removal of inhibition raises excitability in preBötC. Moreover, findings from anesthetized adult animals shows that blocking inhibition in the preBötC, either pharmacologically or via photoinhibition, does not stop breathing. Rather, disinhibition abolishes the vagus nerve-mediated Breuer-Hering pulmonary reflex (Janczewski *et al.*, 2013).

Therefore, inhibition is not obligatory for respiratory rhythm generation, but it can modulate the network and shape the respiratory motor output (Feldman & Smith, 1989; Janczewski *et al.*, 2013; Sherman *et al.*, 2015; Baertsch *et al.*, 2018; Fortuna *et al.*, 2019; Hülsmann *et al.*, 2021; Vafadari *et al.*, 2023, 2024).

1.5.2. Pacemaker theory and intrinsic properties of preBötC interneurons

When the preBötC was originally described (Smith *et al.*, 1991), whole-cell patch-clamp recordings and XII nerve recordings were used to initially explore the intrinsic properties of its inspiratory neurons.

Initially, the preBötC inspiratory neurons were held at baseline membrane potentials of approximately -60 mV. At those values, the synaptic drive potentials from an inspiratory neuron and XII motor output showed synchronized activity.

Additional depolarization to -55 mV, by increasing the amount of applied current, facilitated the occurrence of oscillatory bursts in those cells. These bursts were called “ectopic bursts” because they happened in the interval between inspiratory bursts so they could have been attributed to network drive and were not associated with XII output. The occurrence of these events increased as the

membrane was further depolarized, up to the point where the preBötC neuron only exhibited a tonic spiking (Del Negro *et al.*, 2002a).

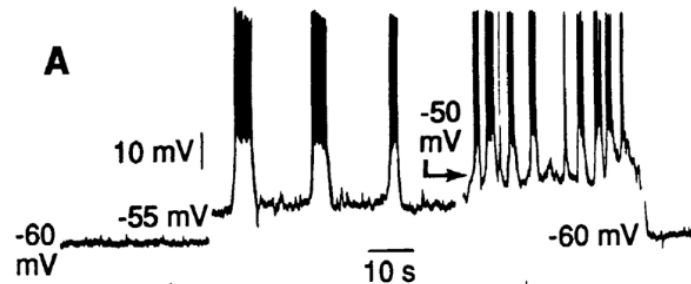


Figure 1.9 – Inspiratory preBötC neurons have voltage-dependent bursting pacemaker activity. Whole-cell patch-clamp recording shows large-amplitude oscillatory bursting activity from a neuron in the preBötC. Bursting activity of the cell was conditional to the membrane voltage, and changed from quiescent (left flat trace), to oscillatory (middle traces), to tonic spiking (right traces) in response to depolarizing current steps. From (Smith *et al.*, 1991).

Activity from the preBötC synchronized with the XII nerve output was regarded, at least in part, to synaptic drive from the network activity during the inspiratory phase. However, the fact that these neurons could generate bursts apparently independently from the network activity was the evidence that they had intrinsic rhythmogenic properties, although those properties could only be observed within a limited range of membrane potentials. Because of this voltage-dependent bursting property, these neurons were called *conditional pacemaker* (Smith *et al.*, 1991, 2007; Del Negro *et al.*, 2002a, 2005). Blocking synaptic transmission pharmacologically *in vitro* did not preclude this conditional bursting-pacemaker activity (Del Negro *et al.*, 2002a, 2005; Peña *et al.*, 2004).

This was enough for researchers to hypothesize that those pacemaker neurons would be the kernel for rhythmogenesis in the preBötC, thus driving an inspiratory burst, and “*pacemaker hypothesis of rhythmogenesis*” was postulated.

One mechanism that accounts for the voltage-dependent bursting-pacemaker activity in those neurons is the persistent sodium current (Johnson *et al.*, 1994; Del Negro *et al.*, 2001, 2002a; Thoby-Brisson & Ramirez, 2001; Ptak *et al.*, 2005; Koizumi & Smith, 2008; Yamanishi *et al.*, 2018). The I_{NaP} can be measured using voltage-ramp protocol, where instead of using an incremental set of step commands to change the membrane voltage, one would slowly increase the voltage in a linearly ramping fashion, for instance from -70 up to +10 mV over several hundred milliseconds or seconds (Chandler *et al.*, 1994), while continually measuring the membrane current. By plotting the evoked current versus the ramped voltage command, a quasi-steady state current-voltage (I-V) curve is obtained. The I-V curve does not follow a linear ohmic relation because it shows a “N” shape, whose region of negative slope resistance starts at approximately -55 mV. This downward deflection of the I-V curve (i.e., negative slope resistance) is due to the activation of I_{NaP} at or around that voltage.

Thus, the *pacemaker hypothesis of rhythmogenesis* proposed that neurons in the preBötC expressing I_{NaP} would drive the network rhythm. Nonetheless, it is important to note that these cellular bursting pacemaker properties rely on the expression of I_{NaP} in concert with a relatively low magnitude leakage K^+ current (I_{K-leak}). Therefore, even though I_{NaP} is expressed ubiquitously in the preBötC, only a small subset of preBötC inspiratory neurons, between 5% to 25%, possess the requisite ratio of I_{NaP} to I_{K-leak} and exhibit voltage-dependent bursting-pacemaker properties (Smith *et al.*, 1991; Butera *et al.*, 1999; Del Negro *et al.*, 2002b,

2002a, 2005; Peña *et al.*, 2004; Pagliardini *et al.*, 2005; Ptak *et al.*, 2005; Koizumi & Smith, 2008b; Yamanishi *et al.*, 2018).

The testable prediction now is: if I_{NaP} -driven conditional bursting pacemaker neurons are obligatory for rhythmogenesis, then removal of this mechanism should slow down or stop the rhythm *in vitro* and *in vivo*.

Several attempts were carried out to test the pacemaker hypothesis, such as perturbing the I_{NaP} mechanism by blocking the current using riluzole, a Na⁺ channel antagonist (Benoit & Escande, 1991; Doble, 1996; Song *et al.*, 1997; Urbani & Belluzzi, 2000), in a perfused bath containing the rhythmically active slice, or via local microinjections.

The required concentration of riluzole to block I_{NaP} is ~20 μ M. When riluzole is microinjected locally in the preBötC, the bursting behavior in all the preBötC pacemaker neurons was abolished, as expected, however, the XII frequency was not affected (Del Negro *et al.*, 2002a, 2005; Pace *et al.*, 2007). However, when riluzole was applied in the bath solution, the XII rhythm was eliminated. This observation was regarded to the effects of riluzole in other areas present in the slice preparation, such as *raphé* that sends excitatory projections to preBötC contributing for the inspiratory drive (Pace *et al.*, 2007).

Congruently, riluzole applied in rhythmic mouse embryo slices at embryonic (E) day 16.5 blocked rhythmic activity, but the same treatment at E18.5 failed to stop the network. Interpretation from these findings indicates that I_{NaP} and bursting-

pacemaker properties are relevant for embryonic network function but ultimately non-essential (Chevalier *et al.*, 2016).

The most parsimonious conclusion from these findings is that I_{NaP} -driven voltage-dependent bursting-pacemaker neurons are not obligatory for inspiratory rhythm generation. However, experiments in rat slices obtained incommensurate results. Application of riluzole and nanomolar concentrations of tetrodotoxin (TTX), another means to block I_{NaP} preferentially, decelerated and then stopped the inspiratory rhythm (Koizumi & Smith, 2008a). Those experiments were used to advocate for the essential role of I_{NaP} .

1.5.3. Finding a new approach to test the pacemaker hypothesis

The results from experiments discussed in the section above led to incompatible conclusions, and distinct groups have proposed that I_{NaP} -driven voltage-dependent bursting-pacemaker neurons is not the underlying mechanism for inspiratory rhythm generation, while others advocate the opposite.

The disparity in the results and the difficulty in making clear whether such mechanism play a role in breathing is due to the use of riluzole and TTX to pharmacologically block I_{NaP} . Application of these drugs can have too many uncontrolled side effects because riluzole blocks I_{NaP} in other areas, it also affects calcium channels, and it diminishes excitatory synaptic transmission by decreasing glutamate release as well as (Doble, 1996; MacIver *et al.*, 1996;

Bellingham, 2011). Regarding those experiments that successfully blocked I_{NaP} and did not stop the rhythm, computational models suggested that I_{NaP} can escape riluzole blockade by being reactivated by transient hyperpolarizing perturbations from inhibitory neurons in the interval between inspiratory bursts (Phillips & Rubin, 2019).

Besides, there was no documented evidence that lack of I_{NaP} in unanesthetized freely behaving animals could also stop or perturb the respiratory frequency. Even though reduced slice preparations are important for understanding the intricates of the microcircuit isolated from feedback systems, *in vivo* experiments are the gold-standard in physiology experiments as they allow for complementary understanding of the respiratory network embed in an intact system. Therefore, a new approach, that could selectively target I_{NaP} and avoid off-target effects *in vivo* was required.

The voltage-gated sodium channels are transmembrane proteins that selectively allow sodium ions to flow into the cell, which causes membrane depolarization. All sodium channels are formed by α -subunit (principal) and β -subunits (auxiliary). The α -subunit is formed by 4 repeated domains (I – IV), and each domain is formed by 6 transmembrane segments. The 4th segment (S4) is the voltage sensor, and the 5th and 6th segments (S5 – S6) are connected by a loop that crosses the membrane, and when the channel is entirely assembled, those loops form the pore. Thus, the α -subunit plays the major role in the channel.

Nine channel isoforms of the α -subunit are known. Therefore, there is a large family of voltage-gated sodium channels, composed of Nav1.1, Nav1.2, Nav1.3, Nav1.4, Nav1.5, Nav1.6, Nav1.7, Nav1.8, and Nav1.9, whose members are all involved in “fast” sodium currents that underlie action potentials, but not necessarily “persistent” sodium currents (Catterall, 1992, 2000; de Lera Ruiz & Kraus, 2015).

Only four subunits (Nav1.1, Nav1.2, Nav1.3, and Nav1.6) are related to sodium currents in brain tissues. The Nav1.4 is primarily expressed in skeletal muscle outside of the Central Nervous System, and the Nav1.5 is abundantly localized to dorsal root ganglions in the Peripheral Nervous System (PNS), and cardiovascular musculature. Nav1.7, Nav1.8 and Nav1.9 are expressed predominantly in the peripheral nervous system (Hille, 2001; de Lera Ruiz & Kraus, 2015), where Nav1.7 is associated with painful stimuli (SD *et al.*, 2013). Nav1.8 and Nav1.9 are notoriously insensitive to TTX (Hille, 2001), and Koizumi *et al.* (2008) indicated that the target ion channel should be equally sensitive to low concentrations of TTX as well as riluzole.

The subunit Nav1.6 is widely expressed throughout the nervous system and can be found in different sites such as nodes of Ranvier, cell bodies, dendrites, and presynaptic terminals. The *Scn8a* gene encodes the Nav1.6 and global null mutations that eliminate *Scn8a* result in severe motor dysfunction, including ataxia and progressive paralysis of hind limbs, and premature death. The loss of these channels also leads to altered electrophysiological function of Purkinje neurons (Burgess *et al.*, 1995; Do & Bean, 2004; Levin *et al.*, 2006). Additionally,

null mutant mice for *Scn8a* show severely diminished I_{NaP} in cerebellar Purkinje cells (Raman *et al.*, 1997).

The role of Nav1.6 in giving rise to I_{NaP} makes this subunit a strong candidate for testing the pacemaker hypothesis for respiratory rhythm generation *in vivo*.

Using genetic techniques that will be discussed later, I hypothesized that complete deletion of the *Scn8a*, thus Nav1.6, via conditional knockout would stop inspiratory bursting rhythmic activity of slices containing the preBötC. Secondly, conditional knockout and conditional knockdown would slow down or stop the breathing frequency of unanesthetized neonate and adult mice.

Therefore, the second chapter challenges the current understanding that I_{NaP} -driven pacemaker neurons in the preBötC are obligatory for rhythmogenesis.

1.6. How is the inspiratory burst terminated?

As previously describe, one complete eupneic breathing cycle in mammals is triphasic, composed by inspiration, postinspiration, and expiration. Because inspiration is active and always present, my dissertation dedicated in understanding the ionic mechanisms underlying this phase both its initiation and termination.

Having discussed so far one mechanism suggested to be involved in initiating breathing and why I sought to test it, as will be demonstrated in Chapter 2, I will also bring attention to the putative ion channel mechanism involved in burst

termination. Henceforth, unless explained otherwise, when “inspiration” is used along with “burst”, this will describe the electrical activity recorded in slice preparations of preBötC, while “inspiration” alone will be used designate the phase *in vivo*.

It is important to note that other properties in the respiratory network may play a major role in rhythmogenesis, initiating and terminating the excitatory drive for breath in the preBötC, as presented above and later in Chapter 2 and Chapter 3. For now, we should assume that there is solid evidence on how inspiratory rhythm is initiated and sustained by the preBötC, but limited emphasis has been given on understanding how it terminates. Therefore, my next project sought to unravel what mechanisms could possibly contribute to ending inspiration, allowing the system transition to expiration.

Although it was ruled out as the essential mechanism for berthing generation, the inhibitory “ring model”, described above, was also used to explain how inspiratory bursts terminate.

According to this model, the I_{NaP} -driven pacemaker neurons in the preBötC comprise the pre-I population and intrinsically generate rhythmic bursting activity. At the same time, the inhibitory early-I population receives excitation from pre-I and inhibits all expiratory neurons in the BötC during expiration. At a certain point in the cycle, the activity in postinspiratory and augmenting expiratory neurons in the BötC is sufficient to inhibit pre-I and early-I, therefore terminating the inspiratory burst (Smith *et al.*, 2007).

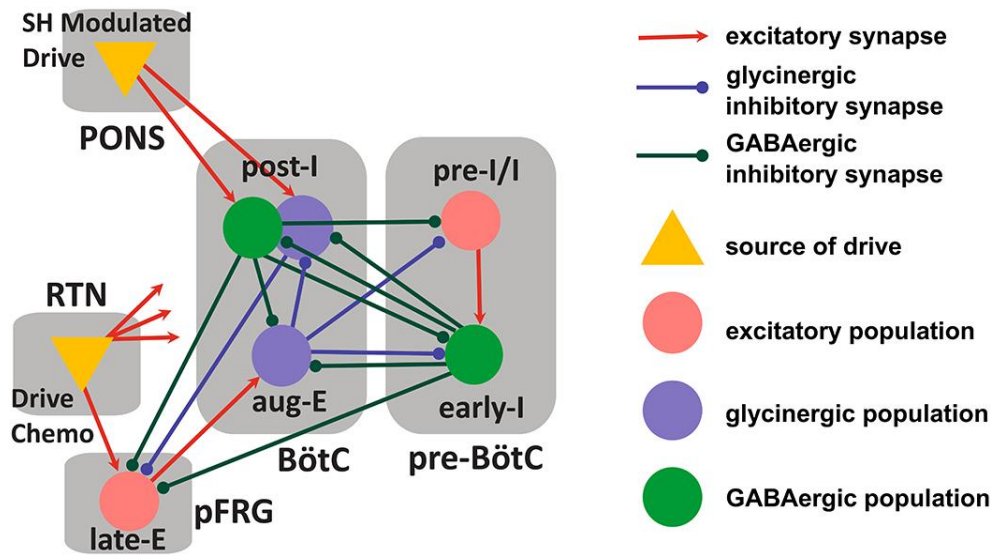


Figure 1.10 – Computational diagram of brainstem respiratory circuits based on the ring model. This model proposes that mutual inhibition between neuronal populations (spheres) in the preBötzinger (preBötC) and the Bötzing (BötC) complexes is essential for respiratory rhythm. Yellow triangles represent sources of tonic excitatory drives. Excitatory and inhibitory synaptic connections are indicated by arrows and small circles, respectively. Color-coded objects indicate the defining neurotransmission for that population, being pink for glutamate, purple for glycine and green for GABA. From left to right, brainstem compartments include RTN: retrotrapezoid nucleus, pFRG: parafacial respiratory group, BötC: Bötzing complex, preBötC: preBötzing complex. Neuronal populations include post-I: post inspirator, aug-E: augmenting expiratory, late-E: late expiratory, pre-I/I: pre-inspiratory/inspiratory, early-I: early inspiratory. From (Flor *et al.*, 2020).

However, this presumption does not seem to be the case, because inspiration still terminates when GABA_A and glycine receptors in the preBötC and BötC are blocked *in vitro*, *in situ*, and *in vivo* (Feldman & Smith, 1989; Hayashi & Lipski, 1992; Janczewski *et al.*, 2013; Sherman *et al.*, 2015; Cregg *et al.*, 2017; Baertsch *et al.*, 2018). Therefore, inhibition only contributes to shape the pattern of respiratory motor output, assuring its stability, but is not obligatory for burst termination (Feldman & Smith, 1989; Kam *et al.*, 2013).

Another mechanism that could contribute for terminating inspiration, at least *in vivo*, is the feedback from the Breuer-Hering inflation reflex (Hering, 1868).

During inspiration, expansion of the lungs increases the activity of slowly adapting pulmonary stretch receptors (SAR) innervating the tracheobronchial tree (Schelegle & Green, 2001; Schelegle, 2003; Lee & Yu, 2014). This signal travels to the nucleus tractus solitarius (NTS) in the brainstem where pump cells receive excitatory monosynaptic connections from SAR (Kubin *et al.*, 2006; Chang *et al.*, 2015). Then, inhibitory second order NTS neurons project to the preBötC and terminates inspiration (Kubin *et al.*, 2006).

Although the Breuer-Hering reflex helps to regulate the timing of inspiration and expiration, it is not the obligatory mechanism used to terminate inspiration because inspiration still terminates in vagotomized mice (Lumsden, 1923; Bonham *et al.*, 1993; Janczewski *et al.*, 2013).

1.6.1. Role of KCNQ-mediated M-currents in burst termination

Inspiratory bursts in preBötC neurons initiate via glutamate transmitter acting on postsynaptic excitatory amino acid receptors. The onset of the burst via recurrent excitation evokes intrinsic conductances based on I_{NaP} and larger magnitude calcium-activated non-specific mixed cation inward (I_{CAN}) currents (Del Negro *et al.*, 2002b, 2002a, 2005; Pace *et al.*, 2007; Ramirez & Baertsch, 2018a; Yamanishi *et al.*, 2018; Picardo *et al.*, 2019). Thus, during an inspiratory burst, Na^+ inward currents (note I_{NaP} and I_{CAN} use Na^+ as the inward charge carrier) are evoked and depolarize preBötC neurons. The depolarizing effect caused by these currents is counterbalanced by outward currents that hyperpolarizes the

membrane potential, which terminates the ongoing excitatory-driven inspiratory burst.

There are several currents that possess suitable activation kinetics that could contribute to terminate the inspiratory burst activity in preBötC, including Na⁺-dependent K⁺ current (I_{K-Na}), ATP-dependent K⁺ current (I_{K-ATP}) and the electrogenic Na⁺/K⁺ ATPase (I_{pump}) current (Del Negro *et al.*, 2009; Krey *et al.*, 2010). One particular outward current that may also contribute to burst termination in the preBötC retained in rhythmic slices, and in breathing phase transitions *in vivo*, is the KCNQ-mediated M-type current.

Distinct from the delayed rectifier currents, the voltage-dependent KCNQ channels underly the M-currents, which were first identified in sympathetic neurons of frogs (Brown & Adams, 1980). They received this name because they are inhibited by stimulation of muscarinic (atropine-sensitive) receptor agonists, such as acetylcholine (Brown & Adams, 1980; Wang & Li, 2016). KCNQ channels are typical K⁺ channels and are composed of four subunits, each one consisting of six transmembrane segments (S1-S6). Characteristically, the subunits encircle a central pore selective to K⁺, formed by the S5 and S6 along with the P-loop domain, and the voltage dependence of this channel is associated with the S4 (Delmas & Brown, 2005; Wang & Li, 2016).

KCNQ channels are part of the voltage-dependent K_v family and are coded by five different genes (KCNQ1-5). The KCNQ1 subunit present minimal levels of expression in the brain and is generally expressed in the heart where it co-

assembles with other proteins and form the cardiac-delayed rectifier-like K⁺ current, and in the inner ear (Robbins, 2001; Wang & Li, 2016). Although it is expressed in the CNS, the subunit KCNQ4 is mostly restricted to areas involved in the central auditory pathway, such as the in outer hair cells of the cochlea and in hair cells of the vestibular apparatus (Kharkovets *et al.*, 2000; Robbins, 2001; Wang & Li, 2016). KCNQ2 and KCNQ3 can be expressed alone but are usually found as heteromultimers and they are proposed to underly the classical M-currents (Wang & Li, 2016; Springer *et al.*, 2021). The role and expression pattern of KCNQ5 are underestimated and have not been elucidated, although it can co-assemble with KCNQ3 (Springer *et al.*, 2021).

M-currents present slow (~500 ms) activating and non-inactivating kinetics, with a subthreshold activation. They open at membrane potentials around -60 mV, below the threshold for action potentials, and reach peak activation above -20 mV (Maljevic *et al.*, 2008; Springer *et al.*, 2021). These voltage-dependent and kinetic properties attribute to KCNQ channels a potential role in shaping neuronal excitability, influencing the resting membrane potential, and firing behavior in various types of neurons. Loss of function mutations in this family are frequently associated with cases of epileptic encephalopathy, such as the benign familial neonatal convulsions (Watanabe *et al.*, 2000; Rogawski & Bazil, 2008; Maljevic *et al.*, 2008), although whether those conditions also feature a breathing phenotype has not been documented.

Previous RNA-seq analysis from our lab demonstrated that KCNQ2 and KCNQ3 subunits are highly expressed in Dbx1 preBötC neurons, whereas KCNQ4,

KCNQ5, and KCNQ1 are less prevalent (Hayes *et al.*, 2017). Therefore, KCNQ2 and KCNQ3 are good candidates to test whether KCNQ-mediated M-currents play a role in bursting termination *in vivo*. Note: in this context we must look for candidate isoforms because we will use genetic technology to perturb the channel expression and function rather than drugs which are usually indiscriminate for subunits.

Previous studies investigated the contributions of M-currents in modulating the preBötC activity by using drugs to activate (retigabine and ICA 69673) and inhibit (XE991 and linopirdine) KCNQ channels. Application of XE991 and linopirdine increased burst duration, while decreasing burst frequency (Wei & Ramirez, 2019; Revill *et al.*, 2021), which would be expected. However, activation of KCNQ channels either by retigabine (Wei & Ramirez, 2019; Revill *et al.*, 2021) or ICA 69673 (Wei & Ramirez, 2019) decreased burst duration and burst frequency in preBötC slices, and it decreased the respiratory frequency of breathing in neonatal and adult mice *in vivo* (Wei & Ramirez, 2019).

Nonetheless, we contend that bath application *in vitro* and intraperitoneal administration *in vivo* of these drugs can have off-target effects, overestimating the real contribution of M-currents.

Thus, my second project hypothesized that if M-currents are important to stop the ongoing excitatory drive to breathe caused by inward depolarizing currents, then (1) lack of function of these channels via conditional knockdown, would increase inspiratory time, while decreasing respiratory frequency *in vivo*. We opted to use

viral-mediated short-harpin (shRNA) knockdown to reduce the expression of *Kcnq2* and *Kcnq3* in glutamatergic preBötC neurons because the use of genetic tools allows for a greater target specificity.

1.7. References

- Alaynick WA, Jessell TM & Pfaff SL (2011). SnapShot: Spinal Cord Development. *Cell* **146**, 178.
- Anderson TM, Garcia AJ, Baertsch NA, Pollak J, Bloom JC, Wei AD, Rai KG & Ramirez JM (2016). A novel excitatory network for the control of breathing. *Nature* **536**, 76–80.
- Ashhad S, Kam K, Del Negro CA & Feldman JL (2022). Breathing Rhythm and Pattern and Their Influence on Emotion. *Annu Rev Neurosci* **45**, 223.
- Baertsch NA, Baertsch HC & Ramirez JM (2018). The interdependence of excitation and inhibition for the control of dynamic breathing rhythms. *Nat Commun* **9**, 1–17.
- Bellingham MC (2011). A review of the neural mechanisms of action and clinical efficiency of riluzole in treating amyotrophic lateral sclerosis: what have we learned in the last decade? *CNS Neurosci Ther* **17**, 4–31.
- Benoit E & Escande D (1991). Riluzole specifically blocks inactivated Na channels in myelinated nerve fibre. *Pflugers Archiv* **419**, 603–609.
- Bianchi AL, Denavit-Saubié M & Champagnat J (1995). Central control of breathing in mammals: neuronal circuitry, membrane properties, and neurotransmitters. *Physiol Rev* **75**, 1–45.
- Bonham AC, Coles SK & McCrimmon DR (1993). Pulmonary stretch receptor afferents activate excitatory amino acid receptors in the nucleus tractus solitarii in rats. *J Physiol* **464**, 725.
- Bouvier J, Thoby-Brisson M, Renier N, Dubreuil V, Ericson J, Champagnat J, Pierani A, Chédotal A & Fortin G (2010). Hindbrain interneurons and axon guidance signaling critical for breathing. *Nat Neurosci* **13**, 1066–1074.
- Briscoe J, Sussel L, Serup P, Hartigan-O'Connor D, Jessell TM, Rubenstein JLR & Ericson J (1999). Homeobox gene Nkx2.2 and specification of neuronal identity by graded Sonic hedgehog signalling. *Nature* **398**, 622–627.
- de Britto AA & Moraes DJA (2017). Non-chemosensitive parafacial neurons simultaneously regulate active expiration and airway patency under hypercapnia in rats. *Journal of Physiology* **595**, 2043–2064.

- Brown DA & Adams PR (1980). Muscarinic suppression of a novel voltage-sensitive K⁺ current in a vertebrate neurone. *Nature* **283**, 673–676.
- Brown TG (1914). On the nature of the fundamental activity of the nervous centres; together with an analysis of the conditioning of rhythmic activity in progression, and a theory of the evolution of function in the nervous system. *J Physiol* **48**, 18.
- Burgess DL, Kohrman DC, Galt J, Plummer NW, Jones JM, Spear B & Meisler MH (1995). Mutation of a new sodium channel gene, *Scn8a*, in the mouse mutant 'motor endplate disease.' *Nat Genet* **10**, 461–465.
- Burns BD (1963). The central control of respiratory movements. *Br Med Bull* **19**, 7–9.
- Butera RJ, Rinzel J & Smith JC (1999). Models of respiratory rhythm generation in the pre-Bötzinger complex. I. Bursting pacemaker neurons. *J Neurophysiol* **82**, 382–397.
- Catterall WA (1992). Cellular and molecular biology of voltage-gated sodium channels. *Physiol Rev*; DOI: 10.1152/physrev.1992.72.suppl_4.s15.
- Catterall WA (2000). From ionic currents to molecular mechanisms: The structure and function of voltage-gated sodium channels. *Neuron* **26**, 13–25.
- Chandler SH, Hsaio CF, Inoue T & Goldberg LJ (1994). Electrophysiological properties of guinea pig trigeminal motoneurons recorded in vitro. *J Neurophysiol* **71**, 129–145.
- Chang RB, Strohlic DE, Williams EK, Umans BD & Liberles SD (2015). Vagal Sensory Neuron Subtypes that Differentially Control Breathing. *Cell* **161**, 622.
- Cheung T (2013). Limits of Life and Death: Legallois's Decapitation Experiments. *J Hist Biol* **46**, 283–313.
- Chevalier M, Toporikova N, Simmers J & Thoby-Brisson M (2016). Development of pacemaker properties and rhythmogenic mechanisms in the mouse embryonic respiratory network. *Elife*; DOI: 10.7554/ELIFE.16125.
- Cregg JM, Chu KA, Dick TE, Landmesser LT & Silver J (2017). Phasic inhibition as a mechanism for generation of rapid respiratory rhythms. *Proc Natl Acad Sci U S A* **114**, 12815–12820.

- Delmas P & Brown DA (2005). Pathways modulating neural KCNQ/M (Kv7) potassium channels. *Nat Rev Neurosci* **6**, 850–862.
- Del Negro CA, Funk GD & Feldman JL (2018). Breathing matters. *Neuroscience* **19**, 351–367.
- Del Negro CA, Johnson SM, Butera RJ & Smith JC (2001). Models of respiratory rhythm generation in the pre-Bötzinger complex. III. Experimental tests of model predictions. *J Neurophysiol* **86**, 59–74.
- Del Negro CA, Kam K, Hayes JA & Feldman JL (2009). Asymmetric control of inspiratory and expiratory phases by excitability in the respiratory network of neonatal mice in vitro. *J Physiol* **587**, 1217.
- Del Negro CA, Koshiya N, Butera RJ & Smith JC (2002a). Persistent sodium current, membrane properties and bursting behavior of pre-Bötzinger complex inspiratory neurons in vitro. *J Neurophysiol* **88**, 2242–2250.
- Del Negro CA, Morgado-Valle C & Feldman JL (2002b). Respiratory rhythm: an emergent network property? *Neuron* **34**, 821–830.
- Del Negro CA, Morgado-Valle C, Hayes JA, Mackay DD, Pace RW, Crowder EA & Feldman JL (2005). Sodium and calcium current-mediated pacemaker neurons and respiratory rhythm generation. *Journal of Neuroscience* **25**, 446–453.
- Do MTH & Bean BP (2004). Sodium currents in subthalamic nucleus neurons from Nav1.6-null mice. *J Neurophysiol* **92**, 726–733.
- Doble A (1996). The pharmacology and mechanism of action of riluzole. *Neurology*; DOI: 10.1212/WNL.47.6_SUPPL_4.233S.
- Dutschmann M & Paton JFR (2002). Glycinergic inhibition is essential for coordinating cranial and spinal respiratory motor outputs in the neonatal rat. *J Physiol* **543**, 643.
- Feldman JL & Kam K (2015). Facing the challenge of mammalian neural microcircuits: Taking a few breaths may help. *Journal of Physiology* **593**, 3–23.
- Feldman JL, Del Negro CA & Gray PA (2012). Understanding the rhythm of breathing: so near yet so far. ; DOI: 10.1146/annurevphysiol040510130049.
- Feldman JL, Del Negro CA & Gray PA (2013). Understanding the rhythm of breathing: so near yet so far. *Annu Rev Physiol* **75**, 423.

- Feldman JL & Smith JC (1989). Cellular mechanisms underlying modulation of breathing pattern in mammals. *Ann N Y Acad Sci* **563**, 114–130.
- Fitzgerald RS & Cherniack NS (2012). Historical perspectives on the control of breathing. *Compr Physiol* **2**, 915–932.
- Flor KC, Barnett WH, Karlen-Amarante M, Molkov YI & Zoccal DB (2020). Inhibitory control of active expiration by the Bötzing complex in rats. *Journal of Physiology* **598**, 4969–4994.
- Fortuna MG, Kügler S & Hülsmann S (2019). Probing the function of glycinergic neurons in the mouse respiratory network using optogenetics. *Respir Physiol Neurobiol* **265**, 141–152.
- Funk GD, Smith JC & Feldman JL (1993). *Generation and Transmission of Respiratory Oscillations in Medullary Slices: Role of Excitatory Amino Acids*.
- Le Gallois JJC (1812). *Expériences sur le principe de la vie, notamment sur celui des mouvemens du coeur, et sur le siège de ce principe ; suivies du Rapport fait à l'Institut sur celles relatives aux mouvemens du coeur, par M. Le Gallois,...* d'Hautel (Paris). Available at: <http://catalogue.bnf.fr> [Accessed May 14, 2024].
- Garcia-Campmany L, Stam FJ & Goulding M (2010). From circuits to behaviour: motor networks in vertebrates. *Curr Opin Neurobiol* **20**, 116.
- Gray PA (2013). Transcription factors define the neuroanatomical organization of the medullary reticular formation. *Front Neuroanat* **7**, 45777.
- Gray PA, Hayes JA, Ling GY, Llona I, Tupal S, Picardo MCD, Ross SE, Hirata T, Corbin JG, Eugenin J & Del Negro CA (2010). Developmental Origin of PreBotzinger Complex Respiratory Neurons. *Journal of Neuroscience* **30**, 14883–14895.
- Gray PA, Reikling JC, Bocchiario CM & Feldman JL (1999). Modulation of respiratory frequency by peptidergic input to rhythmogenic neurons in the preBötzing complex. *Science* **286**, 1566–1568.
- Grillner S (2006). Biological Pattern Generation: The Cellular and Computational Logic of Networks in Motion. *Neuron* **52**, 751–766.
- Grillner S & El Manira A (2020). Current principles of motor control, with special reference to vertebrate locomotion. *Physiol Rev* **100**, 271–320.

- Guyenet PG & Bayliss DA (2015). Neural Control of Breathing and CO₂ Homeostasis. *Neuron* **87**, 946–961.
- Guyenet PG & Bayliss DA (2022). Central respiratory chemoreception. *Handb Clin Neurol* **188**, 37.
- Guyenet PG, Stornetta RL & Bayliss DA (2010). Central respiratory chemoreception. *J Comp Neurol* **518**, 3883–3906.
- Hayashi F & Lipski J (1992). The role of inhibitory amino acids in control of respiratory motor output in an arterially perfused rat. *Respir Physiol* **89**, 47–63.
- Hayes JA, Kottick A, Picardo MCD, Halleran AD, Smith RD, Smith GD, Saha MS & Del Negro CA (2017). Transcriptome of neonatal preBötzinger complex neurones in Dbx1 reporter mice. *Scientific Reports* 2017 7:1 **7**, 1–13.
- Hering E (1868). Die selbststeuerung der Atmung durch den Nervus vagus. *Sitzber Akad Wiss Wien* **57**, 672.
- Hill RW, Wyse GA & Anderson M (2012). *Animal physiology*, 3rd edition. Sinauer Associates, Sunderland.
- Hille B (2001). *Ion Channels of Excitable Membranes*, 3rd edition. Sinauer Associates, Inc, Sunderland.
- Hofman MA (2012). Design principles of the human brain: an evolutionary perspective. *Prog Brain Res* **195**, 373–390.
- Huckstepp RT, Henderson LE, Cardoza KP & Feldman JL (2016). Interactions between respiratory oscillators in adult rats. *Elife*; DOI: 10.7554/eLife.14203.
- Huckstepp RTR, Cardoza KP, Henderson LE & Feldman JL (2015). Role of Parafacial Nuclei in Control of Breathing in Adult Rats. *The Journal of Neuroscience* **35**, 1052.
- Huff A, Karlen-Amarant M, Pitts T & Ramirez JM (2022). Optogenetic stimulation of pre-Bötzinger complex reveals novel circuit interactions in swallowing-breathing coordination. *Proc Natl Acad Sci U S A*; DOI: 10.1073/PNAS.2121095119/-/DCSUPPLEMENTAL.
- Huff A, Karlen-Amarante M, Oliveira LM & Ramirez JM (2023). Role of the postinspiratory complex in regulating swallow–breathing coordination and other laryngeal behaviors. *Elife* **12**, 86103.

Hülsmann S, Hagos L, Eulenburg V & Hirrlinger J (2021). Inspiratory Off-Switch Mediated by Optogenetic Activation of Inhibitory Neurons in the preBötzinger Complex In Vivo. *Int J Mol Sci* **22**, 1–11.

Janczewski WA & Feldman JL (2006). Distinct rhythm generators for inspiration and expiration in the juvenile rat. *J Physiol* **570**, 407–420.

Janczewski WA, Tashima A, Hsu P, Cui Y & Feldman JL (2013). Role of Inhibition in Respiratory Pattern Generation. *The Journal of Neuroscience* **33**, 5454.

Johnson SM, Smith JC, Funk GD & Feldman JL (1994). Pacemaker behavior of respiratory neurons in medullary slices from neonatal rat. *J Neurophysiol* **72**, 2598–2608.

Kam K, Worrell JW, Janczewski WA, Cui Y & Feldman JL (2013). Distinct Inspiratory Rhythm and Pattern Generating Mechanisms in the preBötzinger Complex. *The Journal of Neuroscience* **33**, 9235.

Karlen-Amarante M, Glovak ZT, Huff A, Oliveira LM & Ramirez J-M (2024). Postinspiratory and preBötzinger complexes contribute to respiratory-sympathetic coupling in mice before and after chronic intermittent hypoxia. *Front Neurosci* **18**, 1386737.

Kharkovets T, Hardelin JP, Safieddine S, Schweizer M, El-Amraoui A, Petit C & Jentsch TJ (2000). From the Cover: KCNQ4, a K⁺ channel mutated in a form of dominant deafness, is expressed in the inner ear and the central auditory pathway. *Proc Natl Acad Sci U S A* **97**, 4333.

Kleinfeld D, Deschênes M, Wang F & Moore JD (2014). More than a rhythm of life: Breathing as a binder of orofacial sensation. *Nat Neurosci* **17**, 647.

Koizumi H & Smith JC (2008a). Persistent Na⁺ and K⁺-Dominated Leak Currents Contribute to Respiratory Rhythm Generation in the Pre-Bötzinger Complex In Vitro. *The Journal of Neuroscience* **28**, 1773.

Koizumi H & Smith JC (2008b). Persistent Na⁺ and K⁺-Dominated Leak Currents Contribute to Respiratory Rhythm Generation in the Pre-Bötzinger Complex In Vitro. *The Journal of Neuroscience* **28**, 1773.

Kottick A, Martin CA & del Negro CA (2017). Fate mapping neurons and glia derived from Dbx1-expressing progenitors in mouse preBötzinger complex. *Physiol Rep*; DOI: 10.14814/phy2.13300.

- Kottick A & Del Negro CA (2015). Synaptic Depression Influences Inspiratory-Expiratory Phase Transition in Dbx1 Interneurons of the preBötzinger Complex in Neonatal Mice. *J Neurosci* **35**, 11606–11611.
- Krey RA, Goodreau AM, Arnold TB & del Negro CA (2010). Outward Currents Contributing to Inspiratory Burst Termination in preBötzinger Complex Neurons of Neonatal Mice Studied in Vitro. *Front Neural Circuits*; DOI: 10.3389/FNCIR.2010.00124.
- Kubin L, Alheid GF, Zuperku EJ & McCrimmon DR (2006). Central pathways of pulmonary and lower airway vagal afferents. *J Appl Physiol (1985)* **101**, 618.
- Kvetnansky R, Sabban EL & Palkovits M (2009). Catecholaminergic systems in stress: Structural and molecular genetic approaches. *Physiol Rev* **89**, 535–606.
- Lanuza GM, Gosgnach S, Pierani A, Jessell TM & Goulding M (2004). Genetic Identification of Spinal Interneurons that Coordinate Left-Right Locomotor Activity Necessary for Walking Movements. *Neuron* **42**, 375–386.
- Lee LY & Yu J (2014). Sensory nerves in lung and airways. *Compr Physiol* **4**, 287–324.
- Leirão IP, Silva CA, Gargaglioni LH & da Silva GSF (2018). Hypercapnia-induced active expiration increases in sleep and enhances ventilation in unanaesthetized rats. *Journal of Physiology* **596**, 3271–3283.
- de Lera Ruiz M & Kraus RL, (2015). Voltage-Gated Sodium Channels: Structure, Function, Pharmacology, and Clinical Indications. *J Med Chem* **58**, 7093–7118.
- Levin SI, Khaliq ZM, Aman TK, Grieco TM, Kearney JA, Raman IM & Meisler MH (2006). Impaired motor function in mice with cell-specific knockout of sodium channel Scn8a (NaV1.6) in cerebellar Purkinje neurons and granule cells. *J Neurophysiol* **96**, 785–793.
- Liebeskind BJ, Hillis DM, Zakon HH & Hofmann HA (2016). Complex Homology and the Evolution of Nervous Systems. *Trends Ecol Evol* **31**, 127.
- Lumsden T (1923). Observations on the respiratory centres in the cat. *J Physiol* **57**, 153.
- MacIver MB, Amagasa SM, Mikulec AA & Monroe FA (1996). Riluzole anesthesia: use-dependent block of presynaptic glutamate fibers. *Anesthesiology* **85**, 626–634.

- Maljevic S, Wuttke T V. & Lerche H (2008). Nervous system KV7 disorders: breakdown of a subthreshold brake. *J Physiol* **586**, 1791–1801.
- Marchenko V, Koizumi H, Mosher B, Koshiya N, Tariq MF, Bezdudnaya TG, Zhang R, Molkov YI, Rybak IA & Smith JC (2016). Perturbations of respiratory rhythm and pattern by disrupting synaptic inhibition within pre-Bötzinger and Bötzing complexes. *eNeuro* **3**, 3033–3046.
- Mellen NM, Janczewski WA, Bocchiaro CM & Feldman JL (2003). Opioid-Induced Quantal Slowing Reveals Dual Networks for Respiratory Rhythm Generation. *Neuron* **37**, 821–826.
- Molkov YI, Abdala APL, Bacak BJ, Smith JC, Paton JFR & Rybak IA (2010). Late-Expiratory Activity: Emergence and Interactions With the Respiratory CPG. *J Neurophysiol* **104**, 2713.
- Moore JD, Deschênes M, Furuta T, Huber D, Smear MC, Demers M & Kleinfeld D (2013). Hierarchy of orofacial rhythms revealed through whisking and breathing. *Nature* **497**, 205.
- Moore JD, Kleinfeld D & Wang F (2014). How the brainstem controls orofacial behaviors comprised of rhythmic actions. *Trends Neurosci* **37**, 370–380.
- Mulkey DK, Stornetta RL, Weston MC, Simmons JR, Parker A, Bayliss DA & Guyenet PG (2004). Respiratory control by ventral surface chemoreceptor neurons in rats. *Nat Neurosci* **7**, 1360–1369.
- Nattie EE & Li A (1995). Rat retrotrapezoid nucleus iono- and metabotropic glutamate receptors and the control of breathing. *J Appl Physiol (1985)* **78**, 153–163.
- Onimaru H & Homma I (2003). A novel functional neuron group for respiratory rhythm generation in the ventral medulla. *J Neurosci* **23**, 1478–1486.
- Pace RW, Mackay DD, Feldman JL & del Negro CA (2007). Role of persistent sodium current in mouse preBötzinger Complex neurons and respiratory rhythm generation. *Journal of Physiology* **580**, 485–496.
- Pagliardini S, Adachi T, Ren J, Funk GD & Greer JJ (2005). Fluorescent tagging of rhythmically active respiratory neurons within the pre-Bötzinger complex of rat medullary slice preparations. *J Neurosci* **25**, 2591–2596.

- Pagliardini S, Janczewski WA, Tan W, Dickson CT, Deisseroth K & Feldman JL (2011). Active Expiration Induced by Excitation of Ventral Medulla in Adult Anesthetized Rats. *Journal of Neuroscience* **31**, 2895–2905.
- Peña F, Parkis MA, Tryba AK & Ramirez JM (2004). Differential contribution of pacemaker properties to the generation of respiratory rhythms during normoxia and hypoxia. *Neuron* **43**, 105–117.
- Phillips RS & Rubin JE (2019). Effects of persistent sodium current blockade in respiratory circuits depend on the pharmacological mechanism of action and network dynamics. *PLoS Comput Biol*; DOI: 10.1371/JOURNAL.PCBI.1006938.
- Picardo MCD, Weragalaarachchi KTH, Akins VT & Del Negro CA (2013). Physiological and morphological properties of Dbx1-derived respiratory neurons in the pre-Bötzinger complex of neonatal mice. *Journal of Physiology* **591**, 2687–2703.
- Pierani A, Moran-Rivard L, Sunshine MJ, Littman DR, Goulding M & Jessell TM (2001). Control of interneuron fate in the developing spinal cord by the progenitor homeodomain protein Dbx1. *Neuron* **29**, 367–384.
- Ptak K, Zummo GG, Alheid GF, Tkatch T, Surmeier DJ & McCrimmon DR (2005). Sodium currents in medullary neurons isolated from the pre-Bötzinger complex region. *J Neurosci* **25**, 5159–5170.
- Raman IM, Sprunger LK, Meisler MH & Bean BP (1997). Altered subthreshold sodium currents and disrupted firing patterns in Purkinje neurons of Scn8a mutant mice. *Neuron* **19**, 881–891.
- Ramanantsoa N, Hirsch MR, Thoby-Brisson M, Dubreuil V, Bouvier J, Ruffault PL, Matrot B, Fortin G, Brunet JF, Gallego J & Golidis C (2011). Breathing without CO₂ Chemosensitivity in Conditional Phox2b Mutants. *The Journal of Neuroscience* **31**, 12880.
- Revill AL, Katzell A, Del Negro CA, Milsom WK & Funk GD (2021). KCNQ Current Contributes to Inspiratory Burst Termination in the Pre-Bötzinger Complex of Neonatal Rats in vitro. *Front Physiol* **12**, 626470.
- Revill AL, Vann NC, Akins VT, Kottick A, Gray PA, Del Negro CA & Funk GD (2015). Dbx1 precursor cells are a source of inspiratory XII premotoneurons. *Elife*; DOI: 10.7554/eLife.12301.

- Ribes V & Briscoe J (2009). Establishing and Interpreting Graded Sonic Hedgehog Signaling during Vertebrate Neural Tube Patterning: The Role of Negative Feedback. *Cold Spring Harb Perspect Biol*; DOI: 10.1101/CSHPERSPECT.A002014.
- Richter DW, Ballanyi K & Schwarzacher S (1992). Mechanisms of respiratory rhythm generation. *Curr Opin Neurobiol* **2**, 788–793.
- Robbins J (2001). KCNQ potassium channels: physiology, pathophysiology, and pharmacology. *Pharmacol Ther* **90**, 1–19.
- Rogawski MA & Bazil CW (2008). New Molecular Targets for Antiepileptic Drugs: $\alpha 2\delta$, SV2A, and Kv7/KCNQ/M Potassium Channels. *Curr Neurol Neurosci Rep* **8**, 345.
- Rubin JE, Shevtsova NA, Bard Ermentrout G, Smith JC & Rybak IA (2009). Multiple Rhythmic States in a Model of the Respiratory Central Pattern Generator. *J Neurophysiol* **101**, 2146.
- Ruffault PL, D’Autréaux F, Hayes JA, Nomaksteinsky M, Autran S, Fujiyama T, Hoshino M, Hägglund M, Kiehn O, Brunet JF, Fortin G & Goriadis C (2015). The retrotrapezoid nucleus neurons expressing *Atoh1* and *Phox2b* are essential for the respiratory response to CO₂. *Elife*; DOI: 10.7554/ELIFE.07051.
- Schelegle ES (2003). Functional morphology and physiology of slowly adapting pulmonary stretch receptors. *Anat Rec A Discov Mol Cell Evol Biol* **270A**, 11–16.
- Schelegle ES & Green JF (2001). An overview of the anatomy and physiology of slowly adapting pulmonary stretch receptors. *Respir Physiol* **125**, 17–31.
- SD D-H, Y Y, JA B & SG W (2013). The Na(V)1.7 sodium channel: from molecule to man. *Nat Rev Neurosci* **14**, 49–62.
- Sherman D, Worrell JW, Cui Y & Feldman JL (2015). Optogenetic perturbation of preBötzinger Complex inhibitory neurons modulates respiratory pattern. *Nat Neurosci* **18**, 408.
- da Silva CA, Grover CJ, Picardo MCD & Del Negro CA (2023). Role of NaV1.6-mediated persistent sodium current and bursting-pacemaker properties in breathing rhythm generation. *Cell Rep*; DOI: 10.1016/j.celrep.2023.113000.

Silva JN, Tanabe FM, Moreira TS & Takakura AC (2016). Neuroanatomical and physiological evidence that the retrotrapezoid nucleus/parafacial region regulates expiration in adult rats. *Respir Physiol Neurobiol* **227**, 9–22.

Smith JC, Abdala APL, Borgmann A, Rybak IA & Paton JFR (2013). Brainstem respiratory networks: building blocks and microcircuits. *Trends Neurosci* **36**, 152–162.

Smith JC, Abdala APL, Koizumi H, Rybak IA & Paton JFR (2007). Spatial and Functional Architecture of the Mammalian Brain Stem Respiratory Network: A Hierarchy of Three Oscillatory Mechanisms. *J Neurophysiol* **98**, 3370–3387.

Smith JC, Ellenberger HH, Ballanyi K, Richter DW & Feldman JL (1991). Pre-Bötzinger complex: a brainstem region that may generate respiratory rhythm in mammals. *Science* **254**, 726–729.

Smith JC, Greer JJ, Liu GS & Feldman JL (1990). Neural mechanisms generating respiratory pattern in mammalian brain stem-spinal cord in vitro. I. Spatiotemporal patterns of motor and medullary neuron activity. *J Neurophysiol* **64**, 1149–1169.

Smith JC, Morrison DE, Ellenberger HH, Otto MR & Feldman JL (1989). Brainstem projections to the major respiratory neuron populations in the medulla of the cat. *J Comp Neurol* **281**, 69–96.

Song JH, Huang CS, Nagata K, Yeah JZ & Narahashi T (1997). Differential action of riluzole on tetrodotoxin-sensitive and tetrodotoxin-resistant sodium channels. *J Pharmacol Exp Ther*.

Souza GMPR, Stornetta RL, Stornetta DS, Abbott SBG & Guyenet PG (2020). Differential Contribution of the Retrotrapezoid Nucleus and C1 Neurons to Active Expiration and Arousal in Rats. *The Journal of Neuroscience* **40**, 8683.

Springer K, Varghese N & Tzingounis A V. (2021). Flexible stoichiometry: implications for KCNQ2 and KCNQ3 associated neurodevelopmental disorders. *Dev Neurosci* **43**, 191.

Stornetta R, Rosin D, Wang H, Sevigny C, Weston M & Guyenet PG (2003). A group of glutamatergic interneurons expressing high levels of both neurokinin-1 receptors and somatostatin identifies the region of the pre-Bötzinger complex. *J Comp Neurol* **455**, 499–512.

- Stornetta RL, Moreira TS, Takakura AC, Kang BJ, Chang DA, West GH, Brunet JF, Mulkey DK, Bayliss DA & Guyenet PG (2006). Expression of Phox2b by Brainstem Neurons Involved in Chemosensory Integration in the Adult Rat. *The Journal of Neuroscience* **26**, 10305.
- Stuart DG & Hultborn H (2008). Thomas Graham Brown (1882--1965), Anders Lundberg (1920-), and the neural control of stepping. *Brain Res Rev* **59**, 74–95.
- Suzue T (1984). Respiratory rhythm generation in the in vitro brain stem-spinal cord preparation of the neonatal rat. *J Physiol* **354**, 173–183.
- Tan W, Janczewski WA, Yang P, Shao XM, Callaway EM & Feldman JL (2008). Silencing preBötzinger Complex somatostatin-expressing neurons induces persistent apnea in awake rat. *Nat Neurosci* **11**, 538.
- Thoby-Brisson M & Ramirez JM (2001). Identification of two types of inspiratory pacemaker neurons in the isolated respiratory neural network of mice. *J Neurophysiol* **86**, 104–112.
- Urbani A & Belluzzi O (2000). Riluzole inhibits the persistent sodium current in mammalian CNS neurons. *European Journal of Neuroscience* **12**, 3567–3574.
- Vafadari B, Oku Y, Tacke C, Harb A & Hülsmann S (2024). In-vivo optogenetic identification and electrophysiology of glycinergic neurons in pre-Bötzinger complex of mice. *Respir Physiol Neurobiol*; DOI: 10.1016/J.RESP.2023.104188.
- Vafadari B, Tacke C, Harb A, Grützner AA & Hülsmann S (2023). Increase of breathing rate mediated by unilateral optogenetic inactivation of inhibitory neurons in the preBötzinger Complex in vivo. *Respir Physiol Neurobiol*; DOI: 10.1016/J.RESP.2023.104032.
- Vann NC, Pham FD, Dorst KE & Del Negro CA (2018). Dbx1 Pre-Bötzinger Complex Interneurons Comprise the Core Inspiratory Oscillator for Breathing in Unanesthetized Adult Mice. *eNeuro*; DOI: 10.1523/ENEURO.0130-18.2018.
- Vann NC, Pham FD, Hayes JA, Kottick A & Del Negro CA (2016). Transient Suppression of Dbx1 PreBötzinger Interneurons Disrupts Breathing in Adult Mice ed. Arenkiel B. *PLoS One* **11**, e0162418.
- Wallén-Mackenzie Å, Gezelius H, Thoby-Brisson M, Nygård A, Enjin A, Fujiyama F, Fortin G & Kullander K (2006). Vesicular glutamate transporter 2 is required for central respiratory rhythm generation but not for locomotor central pattern generation. *Journal of Neuroscience* **26**, 12294–12307.

Wang JJ & Li Y (2016). KCNQ potassium channels in sensory system and neural circuits. *Acta Pharmacol Sin* **37**, 25.

Wang X, Hayes JA, Revill AL, Song H, Kottick A, Vann NC, LaMar MD, Picardo MCD, Akins VT, Funk GD & Del Negro CA (2014). Laser ablation of Dbx1 neurons in the pre-Bötzinger complex stops inspiratory rhythm and impairs output in neonatal mice. *Elife* **3**, e03427.

Watanabe H, Nagata E, Kosakai A, Nakamura M, Yokoyama M, Tanaka K & Sasai H (2000). Disruption of the epilepsy KCNQ2 gene results in neural hyperexcitability. *J Neurochem* **75**, 28–33.

Wei AD & Ramirez JM (2019). Presynaptic Mechanisms and KCNQ Potassium Channels Modulate Opioid Depression of Respiratory Drive. *Front Physiol* **10**, 1407.

West JB (2011). History of respiratory gas exchange. *Compr Physiol* **1**, 1509–1523.

Wu J, Capelli P, Bouvier J, Goulding M, Arber S & Fortin G (2017). A V0 core neuronal circuit for inspiration. *Nat Commun* **8**, 544.

Yamanishi T, Koizumi H, Navarro MA, Milesco LS & Smith JC (2018). Kinetic properties of persistent Na⁺ current orchestrate oscillatory bursting in respiratory neurons. *J Gen Physiol* **150**, 1523–1540.

Chapter 2: Role of Nav1.6-mediated persistent sodium current and bursting-pacemaker properties in breathing rhythm generation

2.1. Abstract

Inspiration is the inexorable active phase of breathing. The brainstem preBötzinger Complex (preBötC) gives rise to inspiratory neural rhythm but its underlying cellular and ionic bases remain unclear. The longstanding “pacemaker hypothesis” posits that persistent Na⁺ current (I_{NaP}) that gives rise to bursting-pacemaker properties in preBötC interneurons is essential for rhythmogenesis. We tested the pacemaker hypothesis by conditionally knocking out and knocking down the *Scn8a* (Nav1.6) gene in core rhythmogenic preBötC neurons. Deleting *Scn8a* substantially decreased I_{NaP} and abolished bursting-pacemaker activity, which slowed inspiratory rhythm in vitro and negatively impacted the postnatal development of ventilation. Diminishing *Scn8a* via genetic interference had no impact on breathing in adult mice. We argue that *Scn8a*-mediated I_{NaP} is not obligatory, but it influences the development and rhythmic function of the preBötC. The ubiquity of I_{NaP} in respiratory brainstem interneurons could underlie breathing-related behaviors such as neonatal phonation or rhythmogenesis in different physiological conditions.

2.2. Introduction

Breathing behavior consists of rhythmic movements that ventilate the lungs, which are initiated by a central pattern generator network in the brainstem.

Inspiration is the inexorable active phase of breathing and emanates from the preBötzinger Complex (preBötC), a specialized site in the ventrolateral medulla (Smith *et al.*, 1991; Feldman & Kam, 2015; Del Negro *et al.*, 2018; Ashhad *et al.*, 2022b). Its core rhythmogenic interneurons are excitatory, i.e., glutamatergic (Funk *et al.*, 1993; Wallén-Mackenzie *et al.*, 2006), derived from precursors cells expressing the transcription factor *Developing Brain Homeobox 1 (Dbx1)* (Bouvier *et al.*, 2010; Gray *et al.*, 2010; Picardo *et al.*, 2013).

Coincident with discovery of the preBötC, a subset of interneurons expressing voltage-dependent bursting properties (Smith *et al.*, 1991) was hypothesized to constitute the oscillatory kernel of the preBötC, thus forming the “pacemaker hypothesis” of rhythmogenesis (Johnson *et al.*, 1994b). Cellular bursting-pacemaker properties depend principally on persistent Na⁺ current (I_{NaP}) being expressed at sufficient magnitude in concert with a relatively low magnitude leakage K⁺ current (I_{K-leak}). Thus, even though I_{NaP} is expressed ubiquitously in the preBötC, only 5-15% of its constituent neurons with the requisite ratio of I_{NaP} to I_{K-leak} , exhibit bursting-pacemaker activity (Smith *et al.*, 1991; Butera *et al.*, 1999; Del Negro *et al.*, 2002b, 2002a, 2005; Peña *et al.*, 2004; Ptak *et al.*, 2005; Koizumi & Smith, 2008a; Yamanishi *et al.*, 2018).

Whether I_{NaP} and bursting-pacemaker properties contribute to inspiratory rhythmogenesis has not been resolved. Several attempts used Na⁺ channel

antagonists like riluzole and tetrodotoxin (TTX) at low doses to block I_{NaP} and thus test the pacemaker hypothesis but yielded incongruent results followed by incompatible interpretations. Riluzole and TTX applied in a neonatal rat slice model of breathing decelerated and then stopped the inspiratory rhythm, which supports the idea that I_{NaP} and bursting-pacemaker properties are obligatory for rhythmogenesis (Koizumi & Smith, 2008a). Similar experiments in neonatal mouse slices showed that rhythm cessation was irreversible (Phillips *et al.*, 2022). Riluzole applied in rhythmic mouse embryo slices at embryonic day 16.5 (E16.5) stopped inspiratory rhythmic activity, although the same treatment at E18.5 failed to stop it, from which the authors conclude that I_{NaP} and bursting-pacemaker properties are relevant for embryonic preBötC function but ultimately non-essential (Chevalier *et al.*, 2016). Different groups working with neonatal mouse slices found that riluzole and TTX abolished the voltage-dependent bursting-pacemaker behavior in preBötC neurons, as expected, but those drugs did not affect the inspiratory frequency (Peña *et al.*, 2004; Del Negro *et al.*, 2005; Pace *et al.*, 2007b), indicating that I_{NaP} and bursting pacemaker activity are superfluous from the standpoint of rhythmogenesis.

Those contradictory reports leave unsolved the cellular bases of inspiratory rhythmogenesis. Thus, to resolve the question one must identify the flaws of past studies and adopt a new approach to avoid them. In that regard, the confounding issues associated with past studies are attributable to pharmacological blockers with promiscuous and nonselective effects. Riluzole depresses excitatory transmission via inhibiting glutamate release as well as postsynaptic receptor

activity (Doble, 1996; MacIver *et al.*, 1996; Bellingham, 2011), which could be the actual cause of riluzole-induced rhythm cessation in some experiments, rather than attenuation of I_{NaP} . In the experiments where riluzole did not stop the rhythm, a modeling study argues that I_{NaP} can escape riluzole blockade by being reactivated via transient hyperpolarizing perturbations from inhibitory neurons in the interval between inspiratory bursts, which would rule out any interpretation of those experiments from the standpoint of blocking I_{NaP} (Phillips & Rubin, 2019).

In addition to the inconclusive pharmacological studies *in vitro*, we still lack categorical experiments *in vivo* that can interrogate the role of I_{NaP} , and thus bursting-pacemaker properties, in awake animals from neonatal to adult stages of development. Thus, new approaches, using genetic tools to selectively target I_{NaP} in the core rhythmogenic population and avoid off-target effects are required to elucidate the role, or lack thereof, of this ionic mechanism in rhythmogenesis.

I_{NaP} is a feature of the voltage-gated sodium channel 1.6 (Nav1.6), encoded by the *Scn8a* gene (Raman *et al.*, 1997; Smith *et al.*, 1998; Burbidge *et al.*, 2002; Do & Bean, 2004*b*; Enomoto *et al.*, 2007; Chen *et al.*, 2008; Zybura *et al.*, 2021). Deletion of *Scn8a* causes a 70-76% reduction in I_{NaP} in null mice (Raman *et al.*, 1997; Do & Bean, 2004*b*). Therefore, although Nav1.1, Nav1.2, Nav1.3, Nav1.6, and Nav1.9 are expressed in rhythmogenic preBötC neurons (Ptak *et al.*, 2005; Hayes *et al.*, 2017; David *et al.*, 2022; Kallurkar *et al.*, 2022), Nav1.6 (*Scn8a*) is the most promising candidate target for genetic manipulation to evaluate the role of I_{NaP} and bursting-pacemaker properties in rhythmogenesis.

Therefore, we attenuated *Scn8a* (Nav1.6) expression in core inspiratory rhythmogenic preBötC neurons via short hairpin RNA (shRNA) silencing technology (conditional knockdown) and precluded *Scn8a* expression in *Dbx1*-derived neurons (hereafter: *Dbx1* neurons), including those in preBötC, using intersectional mouse genetics (conditional knockout). We predict that if I_{NaP} and bursting-pacemaker properties underlie or significantly contribute to inspiratory rhythmogenesis, then *Scn8a* diminution should decelerate, stop, or otherwise perturb breathing in awake intact neonatal and adult mice, as well as in rhythmically active slice preparations.

2.3. Materials & Methods

2.3.1. Mice

Animals were housed in colony cages maintained on a 12 h:12 h light/dark cycle with controlled humidity and temperature at 24° C. They were fed *ad libitum* on a standard commercial mouse diet (Teklad Global Diets, Envigo, Indianapolis, IN, USA) with free access to water. Cages were furnished with several forms of enrichment.

The Institutional Animal Care and Use Committee at William & Mary (IACUC-2021-04-20-14958-cadeln) and the Institutional Biosafety Committee (IBC-2019-09-02-13765-mrdegu) approved these protocols, which conform to policies of the Office of Laboratory Animal Welfare (National Institutes of Health), the National

Research Council (National Research Council, 2011), as well as the ARRIVE guidelines 2.0 (Percie du Sert *et al.*, 2020).

In vivo behavioral experiments. For our conditional knockout model, we crossed *Dbx1*^{Cre} mice (Bielle *et al.*, 2005) with mice featuring a floxed allele of *Scn8a*, *Scn8a*^{fl/+}, and *Scn8a*^{fl/fl}, in which *LoxP* sites flank the first coding exon of *Scn8a*. The floxed allele generates normal Nav1.6 but following Cre-Lox recombination Nav1.6 is deleted completely (Levin & Meisler, 2004). The offspring (*Dbx1*;*Scn8a* mice) were housed with their dams up to postnatal (P) day 21 (P21). We measured ventilation in *Dbx1*;*Scn8a* male and female mice from the neonatal stage (P0) to early adulthood (P21) in 1-h bouts during which the animals were transiently removed from their home cages.

We also measured ventilation in *Vglut2-ires-cre* mice of both sexes, all within the age range of 10–14 weeks, after conditional knockdown of the *Scn8a* with a Cre-dependent shRNA virus surgically delivered into the preBötC. These mice express Cre recombinase in glutamatergic neurons. *Vglut2* and *Dbx1* are markers for the same preBötC population (Bouvier *et al.*, 2010; Gray *et al.*, 2010). Thus, one can use either *Dbx1*^{Cre} or *Vglut2-ires-cre* mice to manipulate inspiratory rhythmogenic neurons of the preBötC.

In vitro electrophysiology and imaging experiments. Using intersectional mouse genetics (a Cre-driver crossed with one or more Cre-responder strains), we knocked-out *Scn8a* and expressed a fluorescent marker in *Vglut2*-expressing neurons. We always employed *Scn8a*^{fl/fl} or *Scn8a*^{fl/+} mice to delete *Scn8a*. For

patch-clamp experiments we additionally used a Cre-responder strain dubbed Ai9 that expresses the fluorescent marker tdTomato. For multi-photon imaging experiments, we additionally used a Cre-responder strain dubbed Ai148 that expresses the genetically encoded Ca²⁺ indicator GCaMP6f.

Therefore, we maintained four distinct lines of double Cre-responders:

Ai9;Scn8a^{fl/fl} and Ai9;Scn8a^{fl/+} as well as Ai148;Scn8a^{fl/fl} and Ai148;Scn8a^{fl/+}. We also maintained a line of Cre-driver-and-responder mice: Vglut2-ires-cre;Scn8a^{fl/+}. The offspring of double Cre-responder mice and Cre-driver-and-responder mice inherited either single- or double-floxed copies of *Scn8a* alleles from each parent. For simplicity, we use the nomenclature Vglut2;Ai9;Scn8a to refer to mice used in patch-clamp experiments and Vglut2;Ai148;Scn8a for mice used in multi-photon imaging experiments. The investigators conducted the experiments blind to mouse genotype.

2.3.2. Electrophysiology

Mouse pups at P0-2 were anesthetized by hypothermia, consistent with the American Veterinary Medical Association guidelines for euthanasia (Leary *et al.*, 2020). We removed the neuraxis from the pons to lower cervical spinal cord within 2 min and submerged it in ice-cold artificial cerebrospinal fluid (aCSF) containing (in mM): 124 NaCl, 3 KCl, 1.5 CaCl₂, 1 MgSO₄, 25 NaHCO₃, 0.5 NaH₂PO₄, and 30 dextrose. The aCSF was aerated continuously with 95% O₂ and 5% CO₂. We trimmed the neuraxis and glued the dorsal surface of the

brainstem onto an agar block (exposing the ventral side). The block and brainstem were affixed rostral side up within a vibratome (Campden Instruments 7000 smz-2, Leicester, UK) while perfusing with aerated ice-cold aCSF. We cut a single transverse slice 450-500 μm thick with preBötC on its rostral surface (Ruangkittisakul *et al.*, 2014).

Slices from *Vglut2;Ai9;Scn8a* mice were held in place and perfused with aCSF (28° C) at 2-4 $\text{mL}\cdot\text{min}^{-1}$ in a recording chamber on a fixed-stage upright microscope equipped with a water-immersion objective (63X, 1.0 numerical aperture). The external K^+ concentration ($[\text{K}^+]_{\text{ext}}$) in the aCSF was raised from 3 to 9 mM, which facilitates robust inspiratory rhythm and XII motor output. We recorded XII motor output using suction electrodes fabricated from borosilicate glass pipettes (OD: 1.2 mm, ID: 0.68 mm) fire-polished to a diameter of $\sim 100 \mu\text{m}$. XII motor output was amplified by 2,000 and band-pass filtered (300-1000 Hz).

We identified tdTomato-expressing neurons using epifluorescence microscopy. Then, whole-cell patch-clamp recordings were performed on those neurons while under visual control using infrared-enhanced differential interference contrast microscopy. Patch pipettes with tip resistance of 4-6 $\text{M}\Omega$ were fabricated from capillary glass (OD: 1.50 mm, ID: 0.86 mm) and filled with solution containing (in mM): 110 CsCl, 5 NaCl, 20 tetraethylammonium-chloride (TEA-Cl), 10 EGTA, 10 HEPES, 1.2 CaCl_2 . We employed a patch-clamp amplifier (EPC10, HEKA Electronic, Holliston, MA, USA) to record membrane current at a gain of 5x or 10x in voltage clamp. All signals were low pass filtered (1 kHz) and digitally acquired at ≥ 4 kHz in PatchMaster software.

Membrane capacitance (C_M) was determined from the integral of the leak-subtracted transient capacity current ($\int I_C$) evoked by a series of 15-ms hyperpolarizing voltage-step commands (V_{com}) applied within 10 mV of holding potential (V_{hold}), using the formula $Q_M = \int I_C$ for each V_{com} . C_M is determined from the slope of the plot of Q_M versus ΔV_M (where ΔV_M is $V_{com} - V_{hold}$) for the series of step commands according to the capacitor law $C_M = V_M \div Q$.

We measured the quasi-steady-state current-voltage (IV) relationship generated by a slow voltage ramp (50 mV/s) between -70 and $+10$ mV.

2.3.3. Multi-photon imaging

We imaged cytosolic Ca^{2+} concentration in neurons contained in slices from Vglut2;Ai148;Scn8a mice. Similarly, $[K^+]_{ext}$ was raised from 3 to 9 mM and slices were held in place and perfused with aCSF ($28^\circ C$) at $2-4 \text{ mL}\cdot\text{min}^{-1}$ in a recording chamber on a fixed-stage multi-photon laser-scanning confocal microscope (Thorlabs, Newton, NJ, USA) equipped with a water-immersion objective (20x, 1.0 numerical aperture). Illumination was provided by an ultrafast tunable laser with a power output of 1050 mW at an emission wavelength of 970 nm, where pulse frequency was 80 MHz and pulse duration was 100 fs (Coherent Chameleon Discovery, Santa Clara, CA, USA). We scanned the preBötC in a raster pattern and used a non-descanned photomultiplier tube to detect reflected light, which was digitally reassembled into images via software. Each frame consisted of a two-way raster scan with a resolution of 256×256 pixels ($116 \times$

116 μm). We collected fluorescence time series data at 15 Hz using ThorImage LS 4.1 software and then analyzed the data using MATLAB 2021a.

To analyze a time series, we first calculated the average fluorescence intensity for all pixels in each frame. Mean fluorescence intensity as a function of time showed periodic network activity. We used the 95% confidence interval (CI) of cycle periods to define the high frequency (short cycle period) and low frequency (long cycle period) limits of a window in frequency space. Next, we performed Fast Fourier transforms of the time series for each pixel. The maximum power from the previously defined window in frequency space was mapped to the corresponding pixel in a new, processed two-dimensional image.

We calculated the mean and standard deviation of the power from each pixel in the new processed image. Rhythmically active pixels exhibited power far greater than the average. Therefore, all pixels with intensity less than mean + 2*SD were set to zero. The remaining contiguous pixel sets, whose area exceeds 8 μm^2 , were retained as regions of interest (ROIs). The Ca^{2+} fluorescence changes within those ROIs, obtained from the original time series, were calculated using the equation $\frac{(F_i - F_o)}{F_o}$, i.e., $\frac{\Delta F}{F_o}$, where F_i is the instantaneous average fluorescence intensity for all pixels within a given ROI and F_o is the average fluorescence intensity of all pixels within that same ROI averaged over the entire time series.

2.3.4. Simulations

We simulated the preBötC neuron model by Butera and colleagues (Butera *et al.*, 1999), specifically model 1 that features a slowly inactivating I_{NaP} . The equations are fully listed in the original publication. Numerical integration was performed by MATLAB (ode45) running a Runge-Kutta 4 method with a variable time step.

2.3.5. Ventilation measurements

Neonatal to juvenile mice. We measured ventilation (\dot{V}_E) in neonatal (P0-9) and juvenile (P12-18) Dbx1;Scn8a mice using a dual-chamber barometric method, which is advantageous for newborn animals with limited thermogenesis (Mortola & Frappell, 2013). Two chambers made of graduated syringes were interconnected via a polyethylene tube. The first chamber housed the mouse and was kept in a water bath to maintain an internal temperature of $\sim 37^\circ\text{C}$, measured by a temperature sensing transponder (BioTherm13, Biomark, Idaho, USA). The second reference chamber was kept outside of the water bath at room temperature ($\sim 25^\circ\text{C}$), having its temperature measured by a digital thermometer, and was connected to a differential pressure transducer (Spirometer, ADInstruments, Colorado Springs, CO, USA) to measure breathing-related pressure oscillations. We adjusted chamber size by moving the syringe plunger to fit closely to the body: 9 mL for mice at age P0, 10 mL at P3-5, 12 mL at P7-9, 25 mL at P12, and 30 mL at P15-18. Air flow through the chambers was maintained at $80\text{ mL}\cdot\text{min}^{-1}$ for mice at ages P0-9, $100\text{ mL}\cdot\text{min}^{-1}$ for mice at age

P12, and 120 mL.min⁻¹ for mice at age P15-18, controlled via the suction pump of a gas analyzer (ADInstruments) and measured using a flowmeter (PFMV530-1, SMCpneumatics, Noblesville, IN, USA) in series with the gas analyzer. Pressure changes due to breathing were sampled at 1 kHz by a PowerLab (ADInstruments) analog-to-digital converter for digital storage and analysis. Mice were placed in the first chamber for a minimum acclimation period of 30 min. \dot{V}_E was measured at 30, 40, and 50 min of elapsed time, where the airflow was interrupted for 2 min and the chamber open only to the pressure transducer. The average of the 3 bouts was reported. Calibration of the tidal volume was done by injecting a known volume of air in the first chamber after the third recording bout.

Early adulthood and adult mice. We measured \dot{V}_E in P21 and adult mice (10-14 weeks old) using flow-through whole-body plethysmography (Mortola & Frappell, 1998). A 300 mL experimental chamber (SCIREQ, Emka Technologies, Québec, Canada) was ventilated with an air mixture (21% O₂ and N₂ balance). Inlet flow was maintained at 250 mL.min⁻¹, controlled by a flowmeter, and outlet flow was maintained at 250 mL.min⁻¹ by a suction pump coupled to the chamber. A fractional leak was introduced into this system to provide better control of the pressure inside the chamber. Thus, this system behaved as if it were sealed for time varying signals with frequency exceeding 0.5 Hz (Jacky, 1978; Mortola & Frappell, 1998, 2013). Body temperature was measured by an indwelling sensor (BioTherm13), ambient temperature was measured by a general-purpose liquid-in-glass thermometer, and chamber temperature was monitored using a digital thermometer. The chamber was connected to a differential pressure transducer

to measure pressure oscillations due to breathing, which were sampled at 1 kHz by a PowerLab for storage and analysis. Mice were placed in the chamber for a minimum acclimation period of 30 min. \dot{V}_E was recorded continuously for additional 30 min. We analyzed 3 bouts of 2 min each and averaged them.

For neonatal (P0-9), juvenile (P12-18), early adulthood (P21) and adult (10-14 weeks old) experiments, we measured two respiratory variables: respiratory frequency (f_R , in breaths per minute, i.e., bpm) and tidal volume (V_T , in mL), the latter calculated using the Drorbaugh-Fenn (Drorbaugh & Fenn, 1955) formula:

$$V_T = \frac{V_K \left(\frac{P_T}{P_K} \right) \times T_B (P_B - P_C)}{T_B (P_B - P_C) - T_A (P_B - P_R)}$$

where V_T is the tidal volume; V_K is the volume of air injected into the animal chamber for calibration; P_T is the pressure deflection associated with the volume of breathed air; P_K is the pressure deflection associated V_K ; T_B is body temperature (in Kelvin, K); P_B is barometric pressure (in mm Hg); P_C is the vapor pressure of water in the animal chamber (in mm Hg); T_A is the air temperature inside the chamber; and P_R is the water vapor pressure at T_B . We present V_T with respect to body mass as a fraction of 100 grams. We obtained P_C and P_R from an appropriate lookup table.

\dot{V}_E was calculated as the product of f_R and V_T . \dot{V}_E and V_T were presented at T_B and ambient barometric pressure, presuming that the air was fully saturated with water vapor (BTPS, stands for **B**ody **T**emperature, **P**ressure, water **S**aturated).

For neonatal mice, the V_K was typically a step volume change of 0.15 mL. For

juvenile and adult mice, V_k was typically 0.3 mL delivered in 5 sets of 20 oscillatory injections at a rate matching the breathing frequency.

2.3.6. Metabolic measurements

Metabolic rate was inferred by indirect calorimetry, which consisted of measuring oxygen consumption ($\dot{V}O_2$) in an open respirometry system using a flow-through (pull mode), configuration where air is drawn into a gas analyzer (ADInstruments) (Mortola, 1984; Cummings *et al.*, 2011). For the dual-chamber system used for neonates (P0-9) and juvenile (P12-18), flow to the gas analyzer was 80, 100, or 120 mL.min⁻¹ depending on age. For the flow-through whole-body plethysmography used for P21 and adult mice, flow to the gas analyzer was 120 mL.min⁻¹. In both configurations, the air was dried through a 10-cm Drierite column (W.A. Hammond Drierit Co. Ltd, Xenia, OH, USA) before passing through the analyzer. We calibrated the gas analyzer using standard room air (20.95% O₂ and 0.03% CO₂) and carbogen mixture (95% O₂ and 5% CO₂). Air was continuously sampled by the gas analyzer and digitally acquired at 1 kHz by PowerLab and LabChart software.

Oxygen consumption was calculated using the following formula (Koteja, 1996):

$$\dot{V}O_2 = \frac{Fl \times (F_{iO_2} - F_{eO_2})}{(1 - F_{iO_2}) \times (1 - RQ)}$$

where FI is the input flow rate, F_{iO_2} is fraction of inspired O_2 ; F_{eO_2} is the fraction of expired O_2 . The respiratory quotient (RQ) is the ratio of carbon dioxide released to oxygen consumed $\frac{\dot{V}CO_2}{\dot{V}O_2}$, which is generally 0.85 for standard mouse diet. The $\dot{V}O_2$ is expressed as a fraction of 100 grams under **Standard conditions of Temperature, Pressure, and Dry air (STPD)**.

2.3.7. Surgical procedures

shRNA injections in the preBötC. We administered a Cre-dependent Adeno-associated virus of serotype 9 (AAV9) carrying a FLEX (flip-excision) construct with a synapsin promoter, and *mCherry* fluorescent protein for glutamatergic neuron identification, on a miR30 backbone (Dow *et al.*, 2012; Chang *et al.*, 2013). The virus also carried a short-hairpin RNA (shRNA) targeting 3 sequences of *Scn8a* mouse gene (NCBI Gene ID: 20273): TTGTCCTGAACACACTATTTA; CTTGACTGGGAGGAGTATAT; TGCCTTGAGACACTACTATTT. Recombination occurred in the presence of *Cre*, which reversed the sequences and led to *mCherry* and shRNA expression.

Mice were anesthetized via isoflurane (5% v/v for induction, and 2% v/v for maintenance), and positioned in a stereotaxic frame. The skull was exposed, aseptically cleaned, and then two holes were drilled at the coordinates: $-6.9-6.8$ mm caudal to bregma, ± 1.2 mm lateral to midline, at a depth of -5.2 mm from the brain surface (Picardo *et al.*, 2019). We injected 50 nL of the virus into the

preBötC using a 30-gauge 0.5 μ L Hamilton Neurosyringe (Hamilton Company, Reno, NV, USA).

Implantation of temperature sensors. We monitored body temperature of P21 mice and adult (10-14 weeks old) mice using a temperature sensing transponder (BioTherm 13) with dimensions 2.12 mm x 13 mm. We inserted the probe in the abdominal cavity via laparotomy after isoflurane anesthesia (5% v/v for induction, and 2% v/v for maintenance), and shaving and cleaning the skin with chlorhexidine (2%) and alcohol (70%). The procedure was completed in ≤ 10 min.

2.3.8. Molecular assays

RNAscope. We used RNAscope Multiplex Fluorescent V2 Assay (Advanced Cell Diagnostics, i.e., ACDBio, Newark, CA, USA) to assess the expression of *Scn8a* transcripts in juvenile *Dbx1;Scn8a* and adult *Vglut2-ires-cre* injected mice. Mice were deeply anesthetized with isoflurane, then perfused through the right atrium with a phosphate-buffered saline solution (PBS) 0.1x, followed by 4% paraformaldehyde (PFA). Their brains were removed and kept in 4% PFA at 4° C overnight (~18 h). For *Dbx1;Scn8a* mice, fixed brains were sectioned at 30 μ m using a vibratome and only 3 sections/animal at bregma levels -7.04 mm, -6.92 mm and -6.8 mm were used for RNAscope. Sections were then saved in a well plate with Tris-buffered saline solution with Tween 20 (TBST) 0.5x, for maximum of 48 h at 4° C and then used for multiplex *in situ* hybridization. For *Vglut2-ires-cre* mice, we also used fixed brains sectioned at 30 μ m in duplicate through the

preBötC. The first replica was used to assess virus expression (*mCherry*) under the fluorescent microscope (Axioscope 5 Upright Microscope, ZEISS). The second replica was saved in a well plate with TBST 0.5x, for maximum of 48 h at 4° C and then used for multiplex *in situ* hybridization. Assays for Dbx1;Scn8a and Vglut2-ires-cre were not run concurrently.

Slices from Dbx1;Scn8a and Vglut2-ires-cre mice were pre-treated equally and followed the same RNAscope protocol. On the first day, sections were washed in TBST 0.5x, mounted onto superfrost slides, and then subjected to a pre-treatment protocol for fixation, dehydration, and target recovery. On the second day, slices were incubated with protease plus for 30 min at 40° C and then incubated in RNAscope oligonucleotide probes for their respective genes of interest, for 2 h at 40° C. For Dbx1;Scn8a samples, we used probes for *Scn8a* and *Even-skipped homeobox 1 (Evx1)*, the latter being a post-mitotic cell marker for *Dbx1* neurons. For Vglut2-ires-cre injected mice, we used probes for *Scn8a* and *mCherry*, the latter being used to identify transduced glutamatergic neurons. Tissues were then processed using the Multiplex Fluorescent Reagent Kit V2 Assay (ACDBio). Fluorescent probes Opal 520 (1:1500), for *Scn8a*, and Opal 690 (1:1500), for *Evx1* and mCherry, were also used. Finally, slides were incubated for 30 s with DAPI, covered with ProLong Gold Antifade Mountant (Invitrogen, Waltham, MA), and coverslipped.

Sections were visualized under the four channel, upright laser-scanning confocal microscope (Cerna, ThorLabs) using a 40x objective (numerical aperture 0.25 µm), and images were acquired using the ThorImage LS 4.1 software.

Genotyping mice (Scn8a^{fl/+}, Scn8a^{fl/fl}, Dbx1^{Cre}, and Vglut2-ires-cre). Genomic DNA from ear or tail was collected and PCR was used to assess genotype. For Scn8a^{fl/+} and Scn8a^{fl/fl} mice, two primers were used: forward: GTG TGT GAT TCT CAA CAG TGG GTT, and reverse: GTC TGT AAG AAG GCC TGA AAG TGA. For Dbx1^{Cre} mice, we used one primer for the wild-type allele: forward: GAG GAT GAG GAA ATC ACG GTG, and reverse: GCA AGG AAA TGT CTC TGG GAC; For the mutant Cre allele, the following primers were used: forward: GTC CAA TTT ACT GAC CGT ACA CC, and reverse: GTT ATT CGG ATC ATC AGC TAC ACC. For Vglut2-ires-cre mice, we used the primers forward: CGG TAC CAC CAA ATC TTA CGG, CAT GGT CTG TTT TGA ATT CAG and reverse: ATC GAC CGG TAA TGC AGG CAA.

2.3.9. Quantification and statistical analysis

Ventilation of Dbx1;Scn8a and Vglut2-ires-cre mice. We plotted respiratory measurements as a function of post-natal age or days post-shRNA injection. We performed linear-regression analyses to obtain the best-fit slope (m) and coefficient of determination (r^2) along with the 95% confidence interval (CI) for each relationship (Graphpad Prism, La Jolla, CA). We used an F-test to evaluate the slope of the respiratory measures versus age or day post-shRNA. If there is no relationship, i.e., slope is zero, then the F statistic returns a *P* value quantifying the likelihood of obtaining a slope deviating from zero.

Body and lung mass. We recorded the body mass of the mice every day before recording ventilation. We plotted their body mass as a function of post-natal age or days post-shRNA injection, performing linear regression analyses as described above. We removed and weighed the lungs of Vglut2-ires-cre mice on the last day of experiments. Differences between lung masses of experimental groups were evaluated using Student's t-test.

mRNA quantification for Vglut2-ires-cre mice and site of injection. The amount of mRNA per glutamatergic preBötC neuron in Vglut2-ires-cre mice was assessed using the open-source software Quantitative Pathology (QuPath) (Bankhead *et al.*, 2017). *mCherry* expression was used to delineate the borders of glutamatergic neurons for subsequent transcript quantification. Each dot inside of a mCherry-positive neuron represents a single transcript. The threshold for detection of cells and transcripts remained fixed throughout the analyzes. We quantified the transcripts on ~6 non-overlapping images per section. Approximately 17 neurons were captured in each picture. Those images were analyzed separately and then averaged, forming one data point per section. We analyzed ~9 sections per mouse and the transcript count for each section was plotted in a univariate scatterplot with the effect size (difference between means) and its 95% confidence interval, i.e., estimation statistics (Calin-Jageman & Cumming, 2019), which includes an unpaired t-test.

The extent of virus expression was evaluated in Vglut2-ires-cre mice. Transverse sections of the brainstem were imaged in a 6 x 4 array at 10x magnification. Tiles were then reassembled using open-source software ImageJ (Schindelin *et al.*,

2012). The virus expression area on sections from individual mice were superimposed onto a section redrawn from the adult mouse brain atlas (Paxinos & Franklin, 2019).

For all statistical tests we applied a significance threshold of $\alpha = 0.05$. Means are reported \pm standard deviation (SD).

2.4. Results

2.4.1. Conditional *Scn8a* knockout reduces I_{NaP} in glutamatergic preBötC neurons

We performed whole-cell patch-clamp recordings from *Vglut2*-expressing preBötC neurons in *Vglut2;Ai9;Scn8a* mice, which reflects the intersection of a *Vglut2*-ires-cre driver strain and two Cre-responder strains: a tdTomato reporter (*Ai9*) for cell identification (Figure 2.1A) as well as a strain where the first exon of *Scn8a* is flanked by *LoxP* sites allowing for conditional gene deletion (Levin & Meisler, 2004).

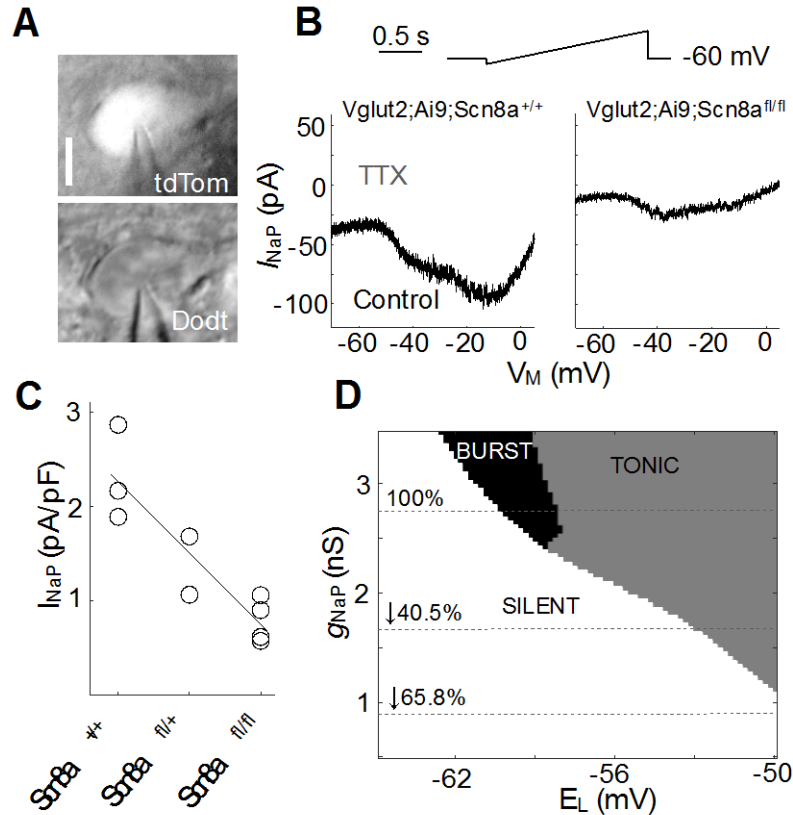


Figure 2.1. Conditional knockout of *Scn8a* reduces I_{NaP} in glutamatergic preBötC neurons. (A) Vglut2-expressing neurons in the preBötC identified via tdTomato (tdTom or Ai9) fluorescence (upper panel) and with differential interference contrast imaging (Dodt, lower panel) during patch-clamp recording. Calibration bar shows 10 μ m. (B) Voltage-ramp commands (upper panel) applied during patch-clamp recordings and quasi-steady-state current-voltage (IV) curves (lower panels) from glutamatergic neurons in Vglut2;Ai9;Scn8a^{+/+} (left) and Vglut2;Ai9;Scn8a^{fl/fl} (right) mouse slices. Gray lines show I-V curves after TTX application. (C) Plot of peak I_{NaP} versus mouse genotype: Vglut2;Ai9;Scn8a^{+/+}, Vglut2;Ai9;Scn8a^{fl/+}, and Vglut2;Ai9;Scn8a^{fl/fl}. Gray circles show individual neuron measurements; horizontal gray line shows the mean for each group. The genotype label is shortened for display convenience. (D) Plot of the behavior of a mathematical model of a canonical preBötC bursting-pacemaker neuron for different values of persistent Na⁺ conductance (g_{NaP}) and the reversal potential of a K⁺-dominated leakage current (E_L). Three activity states are shown according to the ratio between g_{NaP} and E_L : silent (white area), bursting (black area); and tonically spiking (gray area). Horizontal dotted lines show the behaviors supported by the model when g_{NaP} is decreased from its standard value.

We isolated Na⁺ currents using a patch pipette solution containing Cs⁺ as well as a bathing solution containing TEA and Cd²⁺. Vglut2;Ai9;Scn8a^{+/+} wild type mice (Figure 2.1B, left) showed a quasi-steady-state current-voltage (I-V) curve (black

line) whose region of negative slope resistance initiated at approximately -57 mV, the base of the I_{NaP} activation curve (Del Negro *et al.*, 2002a; Koizumi & Smith, 2008a). The I-V curve from $Vglut2;Ai9;Scn8a^{fl/fl}$ mice showed a region of negative slope resistance that initiated at approximately -57 mV but with much less peak inward current (Figure 2.1B, right, black line). TTX blocked the region of negative slope resistance completely as expected for I_{NaP} (Figure 2.1B, grey lines). I_{NaP} measured 2.30 ± 0.50 pA.pF $^{-1}$ in $Vglut2;Ai9;Scn8a^{+/+}$ mice (N = 3), 1.37 ± 0.43 pA.pF $^{-1}$ in $Vglut2;Ai9;Scn8a^{fl/+}$ mice (N = 2, a 40.5% reduction), and 0.79 ± 0.23 pA.pF $^{-1}$ in $Vglut2;Ai9;Scn8a^{fl/fl}$ mice (N = 3, a 65.6% reduction). Linear regression analysis returned a slope of -0.16 pA.pF $^{-1}$ per deleted *Scn8a* allele, which is significantly nonzero ($r^2 = 0.78$, $p = 0.003$) (Figure 2.1C). The coefficient of determination (r^2) demonstrates that 78% of the diminution of I_{NaP} is attributable to loss of *Scn8a*. We infer that *Scn8a* (Nav1.6) predominantly gives rise to I_{NaP} in glutamatergic preBötC neurons, although other isoforms of TTX-sensitive Na $^+$ channels (Nav1.1, Nav1.2, Nav1.3, and Nav1.9) also contribute to the persistent current measured by voltage-ramp commands.

Next, we examined how 40.5% and 65.6% reductions in I_{NaP} would affect the behavior of preBötC bursting-pacemaker neurons according to the canonical mathematical model (Butera *et al.*, 1999) (Figure 2.1D). With persistent Na $^+$ conductance (g_{NaP}) at its standard value of 2.8 nS, the model neuron exhibits silent, bursting, and tonic spiking states depending on excitability governed by the reversal potential of I_{K-leak} (E_L). However, reducing the conductance by either 40.5% or 65.6% prevents bursting-pacemaker activity regardless of E_L ; only

silent and tonic spiking states are then possible. These simulations suggest that bursting-pacemaker behavior would not be possible in glutamatergic preBötC neurons following I_{NaP} reductions in Vglut2;Ai9;Scn8a^{fl/+} and Vglut2;Ai9;Scn8a^{fl/fl} mice.

2.4.2. Conditional Scn8a knockout precludes bursting-pacemaker activity in glutamatergic preBötC neurons but inspiratory rhythmogenesis perdures at lower frequency

We used multi-photon imaging to measure cytosolic Ca²⁺ in glutamatergic preBötC neurons in rhythmic slices from Vglut2;Ai148;Scn8a mice (Figure 2.2). This mouse reflects the intersection of the Vglut2-ires-cre driver strain and two Cre-responder strains: the first (Ai148) features the genetically encoded Ca²⁺ indicator GCaMP6f and the second is the *Scn8a* conditional knockout strain.

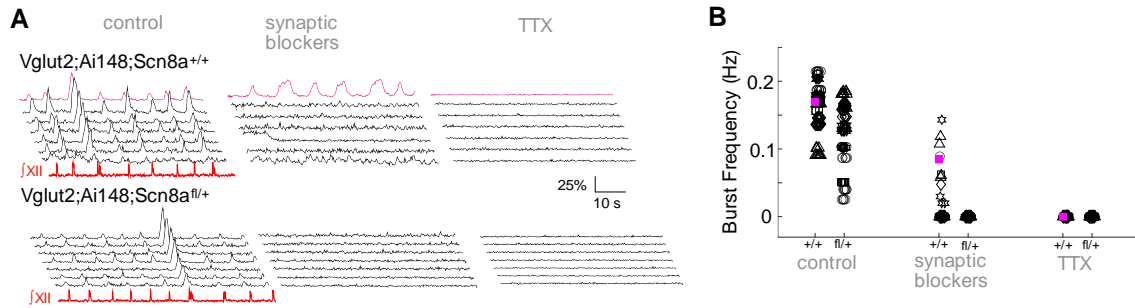


Figure 2.2. Conditional knockout of *Scn8a* in glutamatergic neurons precludes pacemaker activity and slows but does not stop inspiratory rhythm. (A) Calcium activity in glutamatergic preBötC neurons from Vglut2;Ai148;Scn8a^{+/+} (wild-type, upper panels) and Vglut2;Ai148;Scn8a^{fl/+} (heterozygous, lower panels) mouse slices. Multi-photon imaging traces are displayed with the inspiratory motor output activity from the XII cranial nerve (lower trace, red). Each black trace represents one preBötC neuron, and the magenta trace refers to a single neuron also shown in magenta in panel B. From left to right, neuronal activity was recorded under three different conditions: control (left) with standard ACSF bathing solution, ionotropic synaptic receptor blockers (middle), and TTX (right). **(B)** Burst frequency of neurons from Vglut2;Ai148;Scn8a^{+/+} (+/+) and Vglut2;Ai148;Scn8a^{fl/+} (fl/+) mouse slices. Translucent gray symbols represent single neurons; all neurons from the same slice were assigned the same symbol. The magenta symbol represents the neuron with the magenta trace in panel A. As in panel A, from left to right, neuronal activity was recorded under three different conditions: control, ionotropic synaptic receptor blockers, and TTX. The genotype label is shortened for display convenience. The control condition reflects collective activity of all neurons in sync in a rhythmic slice. The synaptic blockers condition shows the subset of neurons with bursting-pacemaker activity after synaptic isolation, but most of the neurons remain quiescent. In TTX, all neurons were quiescent.

We recorded the activity of multiple neurons simultaneously in

Vglut2;Ai148;Scn8a^{+/+} slices (wild-type: with both alleles of *Scn8a* intact) and

Vglut2;Ai148;Scn8a^{fl/+} slices (heterozygous: with only one *Scn8a* allele intact),

while monitoring inspiratory-related motor output from the hypoglossal (XII)

cranial nerve. Conditional full knockout Vglut2;Ai148;Scn8a^{fl/fl} pups were not

viable. In control conditions, rhythmically active glutamatergic neurons

discharged in sync with XII output in wild-type (Figure 2.2A, upper panel) and

heterozygous (Figure 2.2A, lower panel) mouse slices. The frequency in

Vglut2;Ai148;Scn8a^{+/+} slices measured 0.17 ± 0.034 Hz ($n = 114$ neurons in $N =$

5 slices) whereas the frequency in *Vglut2;Ai148;Scn8a^{fl/+}* slices measured 0.12 ± 0.049 Hz ($n = 98$ neurons in $N = 5$ slices), which was significantly different ($p = 1 \times 10^{-14}$) (Figure 2.2B). These data show that slices from both genotypes produce inspiratory rhythm, but that loss of one allele of *Scn8a* in glutamatergic neurons depresses the baseline frequency of the inspiratory rhythm.

Next, we imaged the same neurons after adding a cocktail of ionotropic synaptic receptor antagonists (in μM): 10 CNQX, 10 APV, 5 strychnine, and 5 picrotoxin. Stopping ionotropic receptor-mediated synaptic transmission in *Vglut2;Ai148;Scn8a^{+/+}* slices silenced the XII nerve output and a large fraction of the glutamatergic preBötC neurons. Nevertheless, 12 different glutamatergic neurons from 5 different slices (11% of 114 neurons imaged) continued to generate rhythmic fluorescence transients (Figure 2.2A, middle-upper panel) at frequencies ranging from 0.05 to 0.15 Hz (Figure 2.2B). Rhythmic changes in fluorescence at these frequencies, following blockade of synaptic activity, is the signature of cellular bursting-pacemaker activity in the preBötC (Koshiya & Smith, 1999). In contrast, no neuron remained rhythmically active in *Vglut2;Ai148;Scn8a^{fl/+}* slices in the presence of the cocktail of synaptic blockers (Figure 2.2A, B) indicating a lack of bursting-pacemaker behavior in glutamatergic neurons following a single *Scn8a* allele deletion. Next, 1 μM TTX application stopped rhythmic activity of bursting subset of neurons in *Vglut2;Ai148;Scn8a^{+/+}* slices, which indicates that their bursting-pacemaker activity depended on I_{NaP} (Figure 2.2A, B).

2.4.3. Breathing continues with impairments and locomotion is ataxic in *Dbx1;Scn8a* conditional knockout mice

Molecular assays. We examined breathing in *Dbx1;Scn8a* mice, which reflects the intersection of a *Dbx1*^{Cre} driver strain (Bielle *et al.*, 2005) with the *Scn8a* conditional knockout strain, in which offspring lack *Scn8a* expression in *Dbx1*-derived neurons. We chose to use the *Dbx1*^{Cre} driver because it affects a smaller subset of neurons throughout the nervous system compared to the *Vglut2-ires-cre* strain, yet the *Dbx1*^{Cre} driver strain will cause *LoxP* recombination in interneurons that comprise the rhythmogenic preBötC core, wherein *Dbx1* and *Vglut2* demarcate the same preBötC neurons (Bouvier *et al.*, 2010; Gray *et al.*, 2010). Genotype was confirmed via PCR post hoc (Figure S2.1). We assessed *Scn8a* expression via multiplex *in situ* hybridization at the end of the ventilatory measurements in *Dbx1;Scn8a*^{+/+}, *Dbx1;Scn8a*^{fl/+}, and *Dbx1;Scn8a*^{fl/fl} mice (Figure 2.3A and Figure S2.2). Core preBötC neurons were identified via transcription factor *Even-Skipped Homeobox 1 (Evx1)*, which is expressed post-mitotically in *Dbx1*-derived neurons (Moran-Rivard *et al.*, 2001; Hayes *et al.*, 2017). We observed *Scn8a* co-expression with *Evx1* in sections obtained from *Dbx1;Scn8a*^{+/+} and *Dbx1;Scn8a*^{fl/+} mice, whereas no *Scn8a* was detectable in *Evx1*-expressing neurons in sections from *Dbx1;Scn8a*^{fl/fl} mice (Figure 2.3A and Figure S2.2). We did not quantify the difference in expression between *Dbx1;Scn8a*^{+/+} and *Dbx1;Scn8a*^{fl/+} mouse sections because patch-clamp recordings (Figure 2.1C) provided a direct measure of *I*_{NaP} diminution following single and double allele *Scn8a* deletion in core preBötC neurons.

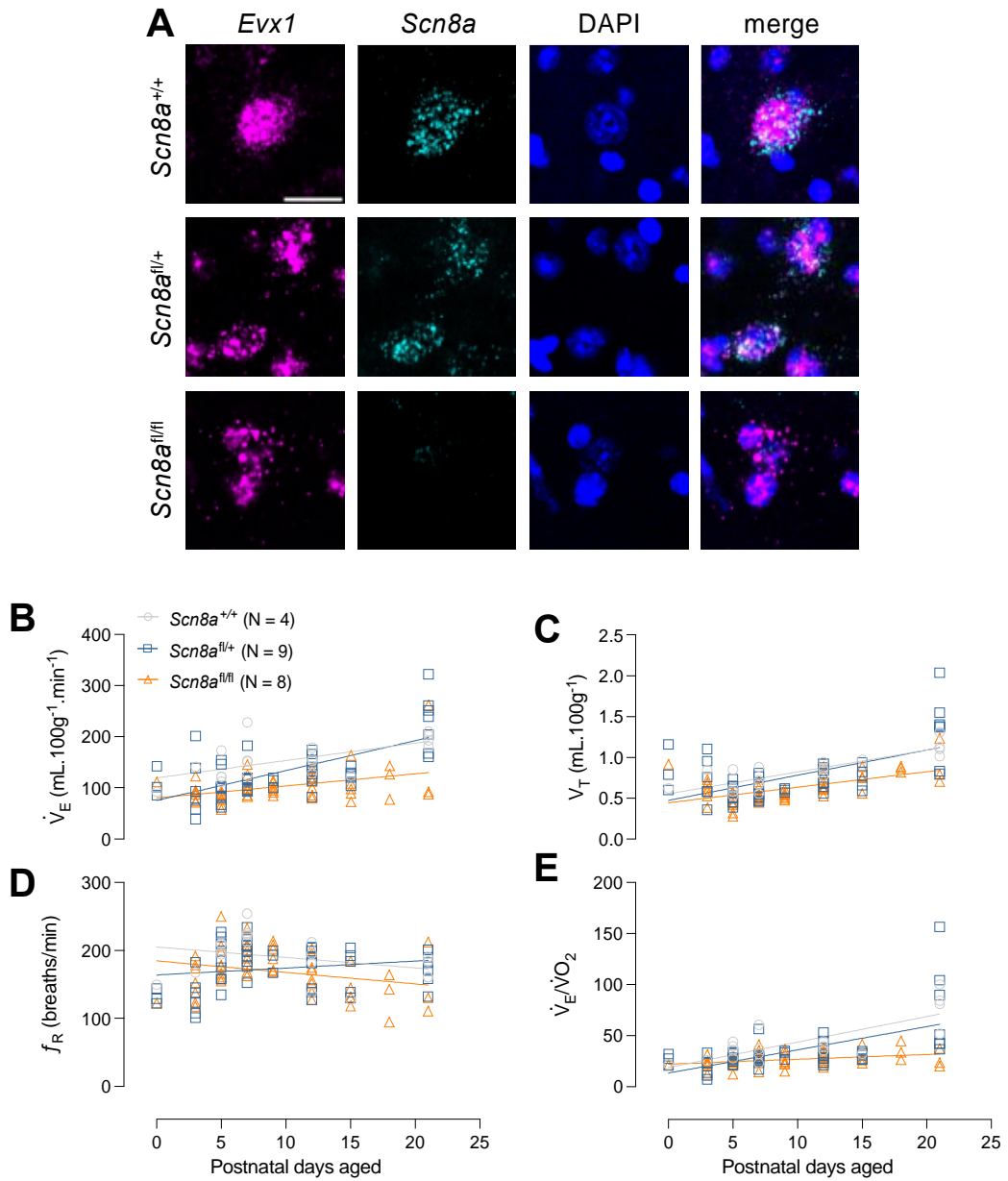


Figure 2.3. *Scn8a* expression and ventilation in *Dbx1;Scn8a* are diminished in conditional knockout mice during postnatal development. (A) RNAscope images showing transcripts of *Evx1* (magenta, first column) and *Scn8a* (cyan, second column). DAPI (blue, third column) shows nuclear staining. The images were merged (fourth column) for colocalization. From top to bottom, representative sections were acquired from *Dbx1;Scn8a*^{+/+}, *Dbx1;Scn8a*^{fl/+}, and *Dbx1;Scn8a*^{fl/fl} mice, respectively. The genotype label is shortened for display convenience. Calibration bar shows 20 μ m. (B–E) Respiratory variables of *Dbx1;Scn8a*^{+/+} (gray), *Dbx1;Scn8a*^{fl/+} (blue), and *Dbx1;Scn8a*^{fl/fl} (orange) mice, measured from P0–P21: ventilation (\dot{V}_E) in panel B, tidal volume (V_T) in panel C, breathing frequency (f_R) in panel D, and the air convection requirement (\dot{V}_E/\dot{V}_{O_2}) in panel E. The genotype labels are shortened for display convenience. Each open symbol represents one individual animal and continuous lines represent linear regression analyses for each group.

Respiratory variables. We measured ventilation (\dot{V}_E), tidal volume (V_T), respiratory frequency (f_R), and the air convection requirement ($\dot{V}_E/\dot{V}O_2$) in Dbx1;Scn8a mice from postnatal (P) day 0 up to early adulthood (P21) (Figure S2.3 shows plethysmography traces). Figure 2.3B-E and Table 2.1 present the linear regression analyses for the respiratory measurements in each group. \dot{V}_E increased with age in all the three groups (i.e., the slope of the regression line was significantly nonzero) (Figure 2.3B, Table 2.1). The increase in \dot{V}_E during postnatal development was due to an increase in the V_T for each group (Figure 2.3C, Table 2.1) because f_R did not change during the observation period (Figure 2.3D, Table 2.1). $\dot{V}_E/\dot{V}O_2$ also increased during postnatal development in all groups of mice (Figure 2.3E, Table 2.1). Oxygen consumption ($\dot{V}O_2$) decreased in Dbx1;Scn8a^{+/+} control mice but $\dot{V}O_2$ did not change during the postnatal observation period in Dbx1;Scn8a^{fl/+} and Dbx1;Scn8a^{fl/fl} mice (Figure S2.4A, Table 2.1).

Table 2.1 – Linear regression of the ventilation (\dot{V}_E), tidal volume (V_T), respiratory frequency (f_R), air convection requirement ($\dot{V}_E/\dot{V}O_2$) oxygen consumption ($\dot{V}O_2$), inspiratory time (T_I), expiratory time (T_E), and inspiratory drive (V_T/T_I), of wild-type ($Dbx1;Scn8a^{+/+}$), heterozygous ($Dbx1;Scn8a^{fl/+}$), and homozygous ($Dbx1;Scn8a^{fl/fl}$) mice. Measurements were performed from postnatal (P) day 0 up to P27-28. r^2 : coefficient of determination. \dot{V}_E is in units of $\text{mL}\cdot\text{min}^{-1}\cdot 100\text{g}^{-1}$. V_T is in units of $\text{mL}\cdot 100\text{g}^{-1}$. f_R is in units of $\text{breaths}\cdot\text{min}^{-1}$. $\dot{V}_E/\dot{V}O_2$ is unitless. $\dot{V}O_2$ is in units of $\text{mL}\cdot\text{min}^{-1}\cdot 100\text{g}^{-1}$. T_I and T_E are in units of s. V_T/T_I is in units of $\text{mL}\cdot\text{s}^{-1}\cdot 100\text{g}^{-1}$. All slopes (m) are calculated per day of observation, i.e., $\text{unit}\cdot\text{d}^{-1}$.

	$Dbx1;Scn8a^{+/+}$ (N = 4)			$Dbx1;Scn8a^{fl/+}$ (N = 9)			$Dbx1;Scn8a^{fl/fl}$ (N = 8)		
	m	r^2	p	m	r^2	p	m	r^2	p
\dot{V}_E	3.41	0.38	$4.85 \times 10^{-3*}$	5.86	0.45	$7.74 \times 10^{-8*}$	2.37	0.16	$3.59 \times 10^{-3*}$
V_T	0.03	0.71	$6.53 \times 10^{-6*}$	0.03	0.35	$5.43 \times 10^{-6*}$	0.02	0.34	$8.47 \times 10^{-6*}$
f_R	-1.53	0.10	0.19	1.02	0.04	0.18	-1.69	0.07	0.06
$\dot{V}_E/\dot{V}O_2$	2.49	0.58	$1.39 \times 10^{-4*}$	2.28	0.35	$5.20 \times 10^{-6*}$	0.47	0.13	0.01*
$\dot{V}O_2$	-0.09	0.44	$1.90 \times 10^{-3*}$	-0.03	0.02	0.29	-0.01	0.002	0.75
T_I	3.94×10^{-3}	0.48	0.13	-2.66×10^{-3}	0.08	0.09	1.21×10^{-4}	2.19×10^{-4}	0.92
T_E	-1.13×10^{-3}	0.02	0.79	-7.11×10^{-3}	0.29	$8.00 \times 10^{-4*}$	3.51×10^{-3}	0.08	0.04*
V_T/T_I	0.06	0.11	0.51	0.23	0.54	$4.70 \times 10^{-7*}$	0.11	0.13	0.01*

*Indicates the slope “m” significantly deviates from zero.

We assessed whether there was an effect of genotype, i.e., whether respiratory development differed between the groups, by comparing the slopes of the regression lines for each of the respiratory variables analyzed. We detected a significant effect of genotype on \dot{V}_E ($p = 0.015$) and $\dot{V}_E/\dot{V}O_2$ ($p = 0.0007$), suggesting that although \dot{V}_E and $\dot{V}_E/\dot{V}O_2$ increased in all three groups during development, $Dbx1;Scn8a^{fl/fl}$ mice increased less than $Dbx1;Scn8a^{fl/+}$ or $Dbx1;Scn8a^{+/+}$ mice (Figure 2.3B and E).

We also detected a significant effect of genotype on f_R ($p = 0.037$), but the interpretation is not straightforward because none of the groups exhibited statistically significant change in f_R during development (the slope of each group’s regression line was ostensibly zero). The groupwise difference in the

regression lines is probably because Dbx1;Scn8a^{fl/+} mice presented a positive slope, whereas Dbx1;Scn8a^{fl/fl} and Dbx1;Scn8a^{+/+} mice had a negative slope, which results in statistically significant disparity between groups (Figure 2.3D). We detected no effect of genotype on V_T ($p = 0.25$, Figure 2.3C) and $\dot{V}O_2$ ($p = 0.23$, Figure S2.4A).

The inspiratory time (T_I), expiratory time (T_E), and the inspiratory drive (V_T/T_I) were also measured and analyzed (Figure S2.4B-D, Table 2.1). We detected no changes in T_I during postnatal development for any of the groups and no significant effect of genotype ($p = 0.08$, Figure S2.4B). T_E did not change during postnatal development in Dbx1;Scn8a^{+/+} mice. Paradoxically, T_E decreased in Dbx1;Scn8a^{fl/+} mice yet T_E increased in Dbx1;Scn8a^{fl/fl} mice during postnatal development, resulting in a significant genotype effect ($p = 0.0004$, Figure S2.4C). We do not consider these effects to be physiologically relevant because the changes in T_E were both on the order of 4–7 ms per day, which is relatively small compared to the typical ~350 ms breathing cycle. Lastly, V_T/T_I did not change during postnatal development in Dbx1;Scn8a^{+/+} mice, but it increased significantly in Dbx1;Scn8a^{fl/+} and Dbx1;Scn8a^{fl/fl} mice. These developmental disparities in V_T/T_I did not result in a significant effect of genotype ($p = 0.072$, Figure S2.4D) so it is not clear whether V_T/T_I disparities can be attributed to conditional *Scn8a* deletion.

Locomotion. Dbx1;Scn8a^{fl/fl} mice developed locomotor ataxia that became apparent after age P10. When placed in the prone position, Dbx1;Scn8a^{fl/fl} mice remained immobile or dragged their hind legs in tandem rather than execute left-

right alternating steps (Video S1). Dbx1;Scn8a^{fl/+} and Dbx1;Scn8a^{+/+} mice moved normally without any obvious locomotor phenotype throughout postnatal development (Video S2).

Survival analysis. Zero out of four Dbx1;Scn8a^{+/+} mice died whereas two out of nine Dbx1;Scn8a^{fl/+} mice died and five out of eight Dbx1;Scn8a^{fl/fl} mice died during postnatal development (Figure S2.5A). The hazard ratio for premature death was 2.81 for the homozygous Dbx1;Scn8a^{fl/fl} mice with respect to heterozygous Dbx1;Scn8a^{fl/+} mice. Hazard ratio cannot be computed with respect to Dbx1;Scn8a^{+/+} control mice because none died. We reject the null hypothesis that the survival curves of Dbx1;Scn8a^{fl/fl} and Dbx1;Scn8a^{fl/+} mice are identical based on a log-rank (Mantel-Cox) method of comparison ($p = 0.04$), which means that homozygous conditional knockout mice are more likely to die prematurely compared to mice from other groups.

Body mass. Dbx1;Scn8a^{+/+} and Dbx1;Scn8a^{fl/+} mice gained body mass during postnatal development at the rate expected for mice with a C57BL/6 background (which typically gain 0.5 g per day, RRID:IMSR_JAX:000664) attaining an average body mass of 13.1 ± 0.7 g (Dbx1;Scn8a^{+/+}) and 11.6 ± 1.8 g (Dbx1;Scn8a^{fl/+}) at the end of the observation period (Figure S2.5B). Their body masses at the end of the observation period were well within the 95% confidence intervals for C57BL/6 mice published by the Jackson Laboratory (Bar Harbor, ME). Dbx1;Scn8a^{fl/fl} mice gained body mass too, reaching 6.03 ± 2.7 g by the end of the observation period (Figure S2.5B), but their rate of body mass gain and final body mass are outside the 95% confidence intervals for C57BL/6 mice.

Therefore, there was a significant effect of genotype on gain of body mass during postnatal development ($p = 1.2 \times 10^{-6}$).

These data and statistics suggest that single deletion of *Scn8a* from Dbx1 neurons has a negligible impact on breathing frequency and its development and maturation from birth to early adulthood. However, removal of both *Scn8a* alleles from Dbx1 neurons has a negative impact on development of ventilation and air convection, and it results in a severe locomotor phenotype predominantly affecting the hindlimbs. The changes in ventilation and locomotion appear to impede development including augmentation of body mass, and the resulting phenotype is often fatal.

2.4.4. Breathing is unimpaired after conditional knockdown of Scn8a in glutamatergic preBötC neurons

We performed virus microinjections in the preBötC of Vglut2-ires-cre adult mice (Figure S2.6A) to attenuate *Scn8a* expression in core rhythmogenic neurons. The AAV in the experimental group carried a Cre-dependent shRNA sequence targeting *Scn8a*. The AAV in the control group carried a non-targeting shRNA sequence consisting of the same nucleotides but in a scrambled order. Both viruses carried the Cre-dependent fluorescent tag *mCherry* for *post hoc* identification of the microinjection site and transduced neurons.

We detected mCherry-expressing neurons adjacent to well-established landmarks that co-localize with the preBötC such as the loop of the inferior olive (IO_{loop}), the semi-compact division of the nucleus ambiguus (NA_{sc}), and the fourth ventricle near obex (Figure S2.6B) (Ruangkittisakul *et al.*, 2014; Paxinos & Franklin, 2019). The *mCherry* expression was detected from Bregma levels –6.8 mm to –7.1 mm, encompassing the anterior-posterior range of the preBötC. *mCherry* expression was densest near the ventral border of the brainstem where preBötC is located and it diminished dorsally in the reticular formation, which hosts output-related inspiratory neurons and dedicated inspiratory premotor neurons (Figure S2.6C) (Koizumi & Smith, 2008a; Revill *et al.*, 2015).

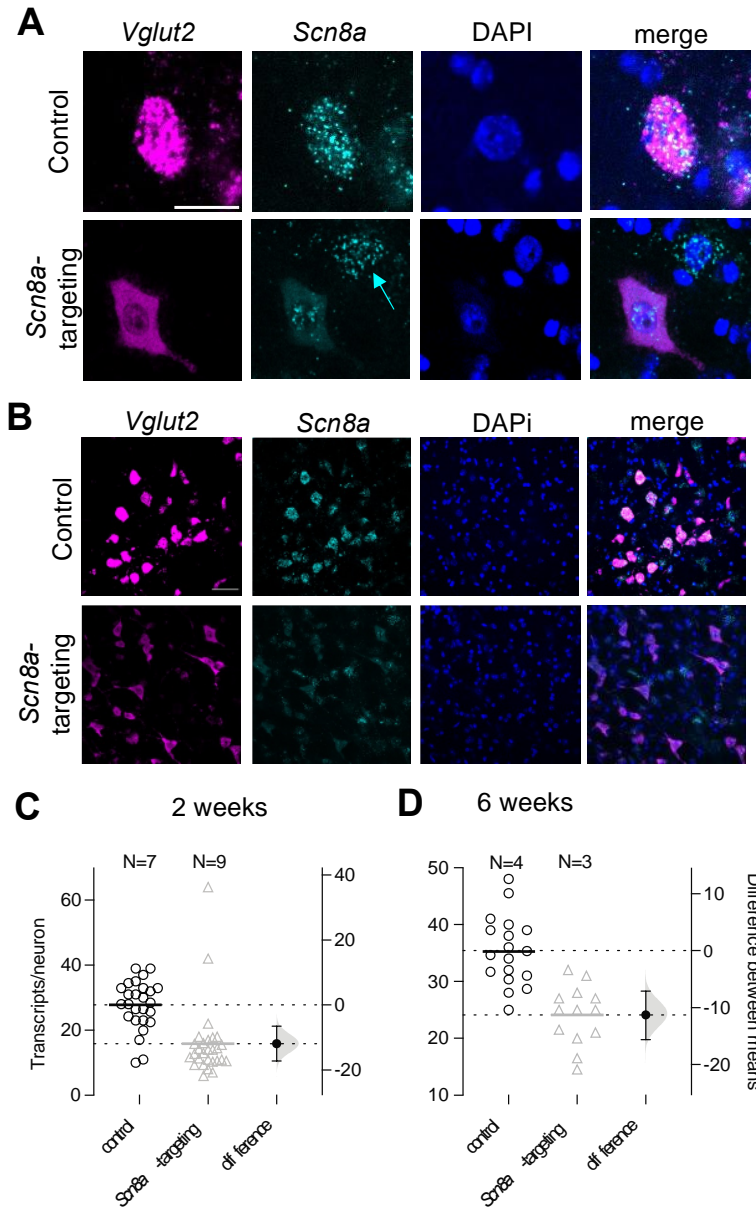


Figure 2.4. *Scn8a*-targeting shRNA decreases gene expression. (A and B) Coronal sections of RNAscope performed in *Vglut2*-ires-cre mice injected with non-targeting shRNA sequence (control, first row) or *Scn8a*-targeting shRNA sequence (second row). (A) *mCherry*-positive glutamatergic (*Vglut2*) neurons (magenta, first column). Other columns (left to right) show *Scn8a* (cyan), DAPI-stained nuclei (blue), and the merge of the three previous images, respectively. The cyan arrow on the second picture of the *Scn8a*-targeting group indicates abundant *Scn8a* transcripts in a neuron not transduced with AAV9. Calibration bar shows 20 μ m. (B) lower magnification images organized as in panel (A). Calibration bar shows 50 μ m. **(C and D)** Dot-scatter plots with effect size (i.e., estimation statistics showing the difference in means with 95% confidence intervals). The number of the *Scn8a* transcripts per preBötC neuron in sections from control mice (black open circles) and in mice injected with *Scn8a*-targeting shRNA (gray open triangles) groups at two (C) and six weeks (D) after AAV9 injection. Each symbol represents one section, which is displayed with mean number of transcripts for all sections and all mice. Black filled circle shows the difference in the means with 95% confidence intervals and a superimposed normal distribution reflecting these data (gray).

We measured *Scn8a* expression via multiplex *in situ* hybridization in glutamatergic preBötC neurons of mice injected with *Scn8a*-targeting and non-targeting shRNA (Figure 2.4A, B and Figure S2.7). Transcript counts, based on puncta that represent single transcript copies visible via RNAscope detection, differ visibly between control and *Scn8a*-targeting shRNA-injected mice. For example, in Figure 2.4A, the cyan arrow in the lower panel shows *Scn8a* expression in a non-glutamatergic neuron from the experimental group that exceeds *Scn8a* expression of an adjacent virus-transduced glutamatergic neighbor and is commensurate with *Scn8a* expression in the virus-transduced glutamatergic neuron from the control group shown in the upper panel.

We quantified *Scn8a* expression using the same detection threshold across all sections and mice (Figure 2.4C, D). We excluded clusters of puncta from this analysis because the number of transcripts in a cluster is unknowable. Mice injected with *Scn8a*-targeting shRNA showed significantly lower *Scn8a* expression compared to control mice at two and six weeks following AAV injection (two weeks: 15.9 ± 11.5 neuron⁻¹ vs. 27.8 ± 7.6 neuron⁻¹, $p = 4.7 \times 10^{-5}$; six weeks: 24.1 ± 5.2 neuron⁻¹ vs. 35.4 ± 6.1 neuron⁻¹, $p = 8.0 \times 10^{-6}$). In both cases *Scn8a* expression decreased by ≥ 11 transcripts per neuron (11.9 neuron⁻¹ for the two-weeks group and 11.3 neuron⁻¹ for the six-weeks group). The effect size, i.e., the mean difference in *Scn8a* expression, is shown with 95% confidence intervals (Figure 2.4C, D, right axes).

We monitored \dot{V}_E , V_T , and f_R every 3-4 days for 7 weeks in another cohort of *Vglut2-ires-cre* mice microinjected in the preBötC with AAVs carrying *Scn8a*-targeting (N = 11) and non-targeting control shRNA (N = 7) (Figure S2.8 shows plethysmography traces). Figure 2.5 and Table 2.2 present the linear regression analyses for both groups.

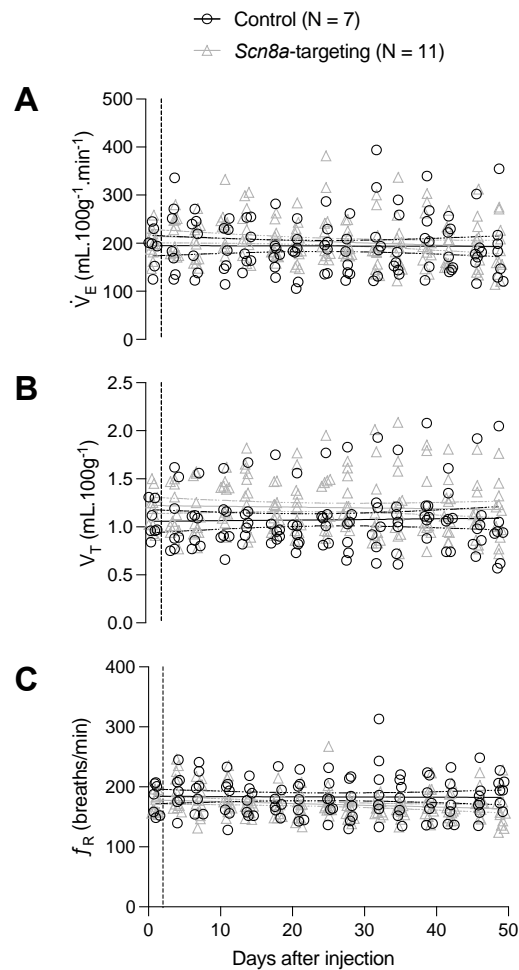


Figure 2.5 – Short-harpin RNA (shRNA) injection in the preBötC does not affect the respiratory variables in unanesthetized adult *Vglut2-ires-cre* mice. (A–C) Respiratory variables of mice injected with a non-targeting (control, black open circles) or *Scn8a*-targeting (gray open triangles) shRNA sequence, measured for 49 days after the injection: ventilation (\dot{V}_E) in panel a, tidal volume (V_T) in panel B, and breathing frequency (f_R) in panel D. Vertical dashed lines indicate the day of the injection. Individual symbols represent measurements from a single mouse. Horizontal continuous lines show linear regression; dashed lines show the 95% confidence intervals for the regression lines.

Ventilation did not change compared to the baseline values of each group; the slope of both regression lines did not deviate from zero. Additionally, there was no evidence of a treatment effect because the slopes of \dot{V}_E vs. days post-injection did not differ between groups ($p = 0.30$, Figure 2.5A). Similarly, V_T remained unaffected following microinjection and we did not observe a treatment effect between control and *Scn8a*-targeting groups ($p = 0.57$, Figure 2.5B).

We observed no changes in f_R for control mice, whereas f_R decreased in the *Scn8a*-targeting group. The change was relatively small ($m = -0.30$ breaths per min per day, a 5.5% change in f_R overall) and the regression analysis returned a low coefficient of determination ($r^2 = 0.035$), which means that only 3.5% of the decrease in f_R , the dependent variable, can be attributed to *Scn8a* attenuation, the independent variable. Furthermore, there was no treatment effect when comparing the slopes of f_R vs. days post-injection between groups ($p = 0.25$, Figure 2.5C). Given the small coefficient of determination, small effect size, and lack of treatment effect, we infer that the decrease in f_R in the *Scn8a*-targeting group is not physiologically meaningful.

Table 2.2 – Linear regression of the ventilation (\dot{V}_E), tidal volume (V_T), respiratory frequency (f_R), inspiratory time (T_I), expiratory time (T_E), and inspiratory drive (V_T/T_I), of adult mice injected with AAVs carrying non-targeting (control) and *Scn8a*-targeting shRNA in the preBötC. R^2 : coefficient of determination. \dot{V}_E is in units of $\text{mL}\cdot\text{min}^{-1}\cdot 100\text{g}^{-1}$. V_T is in units of $\text{mL}\cdot 100\text{g}^{-1}$. f_R is in units of $\text{breaths}\cdot\text{min}^{-1}$. T_I and T_E are in units of s. V_T/T_I is in units of $\text{mL}\cdot\text{s}^{-1}\cdot 100\text{g}^{-1}$. All slopes (m) are calculated per day of observation, i.e., $\text{unit}\cdot\text{d}^{-1}$.

	Control (N = 7)			<i>Scn8a</i> -targeting (N = 11)		
	m	r^2	p	m	r^2	p
\dot{V}_E	-0.02	3.33×10^{-5}	0.95	-0.47	0.02	0.06
V_T	6.36×10^{-4}	8.50×10^{-4}	0.77	-8.44×10^{-4}	0.002	0.58
f_R	-0.03	2.47×10^{-4}	0.87	-0.30	0.04	0.02*
T_I	-4.08×10^{-3}	0.11	0.0007*	1.70×10^{-3}	0.005	0.37
T_E	7.67×10^{-4}	0.04	0.04*	4.09×10^{-4}	0.02	0.09
V_T/T_I	0.05	0.03	0.06	-5.57×10^{-4}	6.02×10^{-6}	0.98

*Indicates the slope “m” significantly deviates from zero.

We further analyzed T_I , T_E , and V_T/T_I . The itemized linear regression analyses are presented in Figure S2.9 and Table 2.2. T_I in the control group decreased following microinjection, but T_I in the *Scn8a*-targeting group did not change. This disparity resulted in a treatment effect between groups ($p = 0.02$, Figure S2.9A). Conversely, the control group showed a statistically significant increase in T_E whereas there was no change in T_E in the *Scn8a*-targeting group. There was no treatment effect regarding T_E ($p = 0.4$, Figure S2.9B). The T_I and T_E changes in the control group are small in effect size and the coefficients of determination are small too. The control group was not subject to gene attenuation, *Scn8a* or any

other known gene because the scrambled nucleotide sequence for the control shRNA does not match any known mouse gene, so we do not consider the changes in T_I and T_E to be physiologically meaningful for evaluating the role of I_{NaP} or the pacemaker hypothesis. Lastly, we observed no changes in inspiratory drive for either group during the post-injection period and we did not observe any treatment effect ($p = 0.09$, Figure S2.9C).

In addition to ventilation measurements, we assessed the body and wet lung masses of the *Scn8a*-targeting shRNA-injected and non-targeting shRNA-injected control mice to evaluate whether *Scn8a* manipulation affected general health or pulmonary physiology (Figure S2.10). The slope of the body mass vs. day post-injection of the *Scn8a*-targeting group deviated from zero ($m = 0.062 \text{ g}\cdot\text{d}^{-1}$, $r^2 = 0.077$, $p = 0.008$) but we did not observe a treatment effect when compared to its control ($p = 0.83$) (Figure S2.10A). Given the lack of treatment effect and small (7.7%) coefficient of determination, it remains unclear how a gain in body mass in these mice could be attributable to *Scn8a* attenuation. Additionally, the wet lung mass did not differ between groups at the end of the study, either unscaled (Figure S2.10B, $p = 0.95$) or scaled to body mass (Figure S2.10C, $p = 0.74$) suggesting no major differences in pulmonary tissue.

2.5. Discussion

The preBötC contains the essential microcircuits for inspiration, the inexorable phase of the respiratory cycle; Dbx1-derived glutamatergic neurons constitute its

rhythmogenic core (Del Negro *et al.*, 2018; Ramirez & Baertsch, 2018*b*, 2018*a*; Ashhad *et al.*, 2022*b*). Knowing the site and cellular point of origin for inspiratory breathing movements is important, but a comprehensive explanation of the behavior must address the cellular and ion channel-level mechanisms of rhythmogenesis. Since the discovery of the preBötC there has been consistent enthusiasm for a rhythmogenic mechanism that depends on I_{NaP} and bursting-pacemaker neurons, i.e., the pacemaker hypothesis. In its contemporary form, the pacemaker hypothesis acknowledges an integral role for excitatory synaptic interactions to synchronize bursting-pacemaker neurons and modify their collective dynamics, but nonetheless is predicated on an essential rhythmogenic role for I_{NaP} .

Evaluating the pacemaker hypothesis has been fraught with controversy because of experimental caveats and limitations associated with drugs that antagonize I_{NaP} . Here, rather than fine-tune drug application protocols or relitigate debates about how to interpret drug-based experiments with mixed outcomes, we sought an alternative approach to test the pacemaker hypothesis that avoids the inherent limitations and ambiguities of pharmacology. We employed genetic technologies that reduce or eliminate the Na^+ channel isoform giving rise to I_{NaP} in core preBötC neurons without off-target effects on other ion channel types or excitatory synaptic transmission.

The widely disseminated report describing the preBötC showed that a subset of its constituent interneurons express voltage-dependent bursting properties, which the authors described as “consistent with the hypothesis that conditional

bursting-pacemaker neurons are the kernel for rhythmogenesis.” Nevertheless, that statement was accompanied by a proviso regarding what evidence would constitute proof that pacemaker neurons are rhythmogenic in neonates and an acknowledgment that developmental changes might modify the rhythmogenic mechanism in adult animals (Smith *et al.*, 1991). The present study, besides evaluating the pacemaker hypothesis in its original and contemporary forms, also addresses the developmental criterion.

Using *Scn8a* conditional knockout mice, we measured inspiratory rhythm in slices from neonatal mice to evaluate the first criterion, i.e., whether pacemaker neurons are rhythmogenic neonatally. Two ionic mechanisms underlie bursting-pacemaker activity in preBötC neurons. The first is I_{NaP} and the second is Ca^{2+} -activated nonspecific cationic current (I_{CAN}) (Smith *et al.*, 1991; Johnson *et al.*, 1994b; Thoby-Brisson & Ramirez, 2001b; Del Negro *et al.*, 2002a, 2005; Peña *et al.*, 2004; Phillips *et al.*, 2022). We now know that I_{CAN} , mediated by Trpm4 ion channels, is important for inspiratory output pattern rather than rhythmogenesis (Koizumi *et al.*, 2018; Picardo *et al.*, 2019; Phillips *et al.*, 2022). Therefore, we confined our analysis to the role of I_{NaP} , targeting Nav1.6 channels encoded by *Scn8a* that constitute I_{NaP} in many neuron types (Raman *et al.*, 1997; Smith *et al.*, 1998; Zybura *et al.*, 2021), including core preBötC neurons (Ptak *et al.*, 2005; Hayes *et al.*, 2017; David *et al.*, 2022; Kallurkar *et al.*, 2022).

We deleted *Scn8a* from Vglut2-expressing neurons, which are synonymous with Dbx1 neurons in the preBötC and form its rhythmogenic core. Voltage-clamp analyses in glutamatergic neurons showed a 41% and 66% reduction in I_{NaP} for

single and double *Scn8a* allele deletion, respectively. Our results are commensurate with previous reports showing 67–76% reduction of I_{NaP} in *Scn8a* mutant and null mice (Raman *et al.*, 1997; Maurice *et al.*, 2001; Do & Bean, 2004*b*). According to the canonical mathematical model, also reproduced here, a preBötC pacemaker neuron does not exhibit bursting following 41% or 66% reductions in I_{NaP} . However, there is some persistent inward current in glutamatergic preBötC neurons following double *Scn8a* allele deletion, and we propose that residual current is most likely ‘window’ current generated by non-Nav1.6 channel isoforms. Indeed, window current is truly persistent as it results from the overlap of steady-state activation and inactivation curves. Nonetheless, voltage-dependent bursting requires rapid (on the order of 1-10 ms) subthreshold I_{NaP} activation followed by its slow inactivation (on the order of 300-1000 of ms). Therefore, window current, without the requisite voltage- and time-dependent properties, cannot contribute to cyclical initiation and termination of cellular bursts. Rather, Na⁺ window current provides a source of tonic excitability akin to Nalcn channels (Lu *et al.*, 2007; Ren, 2011) that could influence network excitability and thus rhythmic frequency (we return to this point below).

preBötC neurons express I_{NaP} ubiquitously (Rybak *et al.*, 2003; Ptak *et al.*, 2005; Pace *et al.*, 2007*b*) but bursting-pacemaker activity is sparse because it depends on sufficient I_{NaP} expression as well as the ratio of I_{NaP} relative to K⁺-dominated leak current (I_{Leak}) (Butera *et al.*, 1999; Del Negro *et al.*, 2002*a*; Purvis *et al.*, 2007; Koizumi & Smith, 2008*a*). We assessed the size of the glutamatergic preBötC neuron subpopulation with bursting-pacemaker properties in rhythmic

neonatal *Vglut2;Ai148;Scn8a^{+/+}* mouse slices. Rhythmic fluorescent transients in the absence of synaptic transmission and inspiratory rhythm, which define bursting-pacemaker activity (Koshiya & Smith, 1999), were present in 11% of glutamatergic preBötC neurons. Previous estimates reported the pacemaker neuron subpopulation to constitute ~5% (P0-P5 and P8-P10 mice) (Del Negro *et al.*, 2005) or 16-29% (P1-P15 mice) (Peña *et al.*, 2004; Pagliardini *et al.*, 2005) of the preBötC. Our data fall within that range. In slices from *Vglut2;Ai148;Scn8a^{fl/+}* mice with only one *Scn8a* allele expressed in glutamatergic neurons, we detected no bursting-pacemaker neurons whatsoever. Those imaging data, as well as patch-clamp analysis in combination with computational modeling, provide unambiguous evidence that *Vglut2;Ai148;Scn8a^{fl/+}* mouse slices are devoid of neurons with bursting-pacemaker activity, regardless of I_{K-Leak} expression. Nevertheless, inspiratory rhythm persisted in *Vglut2;Ai148;Scn8a^{fl/+}* mouse slices, which demonstrates that rhythmogenesis does not require I_{NaP} -mediated bursting-pacemaker activity. Strictly speaking, the pacemaker hypothesis should be rejected according to the first criterion.

Nevertheless, I_{NaP} is relevant because it regulates excitability. Indeed, *Vglut2;Ai148;Scn8a^{fl/+}* mouse slices generated slower inspiratory frequency compared to *Vglut2;Ai148;Scn8a^{+/+}* mouse slices. The most parsimonious explanation is that I_{NaP} contributes inward current that depolarizes constituent rhythmogenic neurons and the net effect is to increase the frequency of inspiratory rhythm.

We also evaluated the pacemaker hypothesis from the perspective of the second criterion described above, which addresses the potential for developmental changes in rhythmogenic mechanisms. We measured breathing from birth through adulthood in unanesthetized mice engineered to remove *Scn8a*-mediated I_{NaP} specifically in *Dbx1*-derived neurons, including those that constitute the preBötC core.

The conditional knockout approach deleted *Scn8a* (Nav1.6) from *Dbx1* neurons. We measured eight respiratory variables during development. Here, we focus on interpreting the variables in which there was a significant effect of genotype in the regression analyses because intergroup disparities can reveal what role *Scn8a* (Nav1.6) and thus I_{NaP} play in breathing rhythmogenesis as it develops. The clearest effects were on ventilation and the air convection requirement, which increased during postnatal development in all the groups. However, the increase was incommensurate such that *Dbx1;Scn8a^{fl/fl}* mice lacking *Scn8a* in *Dbx1* neurons increased \dot{V}_E and $\dot{V}_E/\dot{V}O_2$ at a lower rate compared to *Dbx1;Scn8a^{fl/+}* and *Dbx1;Scn8a^{+/+}* mice with one or both copies of *Scn8a* in *Dbx1* neurons. We conclude that I_{NaP} plays the same role that we identified in slices, namely that it depolarizes rhythmogenic preBötC neurons, but *in vivo* the net effect is to enhance ventilation and air convection rather than frequency *per se*. Absent *Scn8a*-mediated I_{NaP} in core preBötC neurons, these key respiratory variables still develop but not as robustly as when one or both *Scn8a* alleles are expressed.

Respiratory frequency did not change for any group during development. Inspiratory time did not change either. Oxygen consumption decreased in wild type mice but did not change in mice with single or double *Scn8a* deletions in *Dbx1* neurons. We can offer no coherent interpretation for these latter data since the change in oxygen consumption occurred in the control group only. Expiratory time did not change in control mice; it decreased in single *Scn8a* knockout mice, yet it increased in double *Scn8a* knockout mice. Again, it is challenging to find a coherent interpretation for these data since the effect of removing one versus two alleles are in opposition. Unaccompanied by changes in f_R and T_I , it is impossible to attribute changes in T_E to modification of *Scn8a* and attendant cellular properties of preBötC neurons. There was no effect of genotype with respect to inspiratory drive, so the increase in V_T/T_I during development for *Dbx1;Scn8a^{fl/+}* and *Dbx1;Scn8a^{fl/fl}* mice cannot be attributed to manipulation of *Scn8a* expression in *Dbx1* neurons.

During juvenile to adult stages of development *Dbx1;Scn8a^{fl/fl}* mice developed a severe locomotor phenotype partially reminiscent of allelic *Scn8a* mutations (Meisler *et al.*, 2001, 2004) that nullify Nav1.6 expression and cause hindlimb ataxia and discoordination with a failure to thrive. In contrast, *Dbx1;Scn8a^{fl/+}* mice showed no locomotor phenotype and grew at a rate commensurate with *Dbx1;Scn8a^{+/+}* mice and the background C57BL/6 strain from JAX. Germline *Scn8a* mutations affect motoneurons and muscles, whereas our conditional knockout model only affects *Dbx1* interneurons. The locomotor phenotype in *Dbx1;Scn8a^{fl/fl}* mice probably results, at least in part, from deficits in excitability

and repetitive spiking capabilities resulting from Nav1.6 deletion in *Dbx1*-derived canonical V0 neurons of the ventral lumbar spinal cord that govern left-right stepping movements (Talpalar *et al.*, 2013; Kiehn, 2016). A thorough analysis of the locomotor phenotype is beyond the scope of this report focused on breathing-related consequences of conditional *Scn8a* deletion. Because the surviving pups were able to breathe throughout development, the failure to thrive and elevated risk of premature death is likely attributable to deficits of locomotion and sensorimotor integration rather than respiratory insufficiency, although the diminished developmental increase in ventilation and air convection could only exacerbate morbidity and mortality in *Dbx1;Scn8a^{fl/fl}* mice.

The conditional knockdown approach attenuates *Scn8a* (Nav1.6) in glutamatergic neurons limited to the area of virus injection, which avoids the caveat of affecting *Dbx1* neurons in the spinal cord and higher brain. Conditional knockdown is also advantageous because the perturbation occurs at the adult stage, when the preBötC is already fully developed. The downside is that knockdown is incomplete; *Scn8a* expression is diminished but not eliminated. RNAscope quantification indicated that shRNA-mediated *Scn8a* knockdown exceeds 40%, which is sufficient I_{NaP} reduction to preclude bursting-pacemaker activity in preBötC neurons as mathematical modeling and imaging in *Vglut2;Ai148;Scn8a^{fl/+}* slices demonstrated.

Adult mice injected with *Scn8a*-targeting shRNA showed no perturbations of any breathing variables. The injected AAV volumes infected glutamatergic neurons throughout the entire preBötC, even spilling out beyond its borders, so we are

confident that negative behavioral results cannot be attributed to insufficient infection of glutamatergic preBötC neurons. In fact, a potential caveat is infection of neurons within the intermediate reticulation dorsal to preBötC including inspiratory-related hypoglossal premotor neurons (Koizumi *et al.*, 2008; Revill *et al.*, 2015) and whisking oscillator neurons intimately linked with breathing (Moore *et al.*, 2013; Takatoh *et al.*, 2022). If we had observed any form of ataxic breathing that could be attributable, at least in part, to airway patency effects, then a parsimonious explanation would include off-target effects of shRNA that diminish Nav1.6, and thus I_{NaP} -mediated excitability and spiking capabilities, of hypoglossal premotor neurons that impede or disrupt laminar air flow throughout the breathing cycle or during the postinspiration phase specifically. This was not the case, however; we did not observe any breathing-related ataxia.

Neither conditional knockout nor knockdown affected breathing frequency, in contrast to the slice experiments where single-copy *Scn8a* elimination in *Dbx1* neurons slowed down inspiratory rhythm. Why the disparity *in vivo*? Excitatory inputs to the preBötC coming from numerous regions of the intact brain (Yang *et al.*, 2020) can elevate baseline excitability and are active in unanesthetized mice but absent in slices. Further, the preBötC receives feedback from central and peripheral chemoreceptors *in vivo* that also elevate excitability (Del Negro *et al.*, 2018; Guyenet *et al.*, 2019). In awake mice, the removal of *Scn8a* and thus I_{NaP} is probably too small a perturbation to affect breathing frequency in comparison to other active inputs and sensory feedback that regulate preBötC excitability and

thus maintain breathing frequency. In slices, the contributions of *Scn8a*-mediated I_{NaP} to baseline excitability, and thus frequency, are more apparent.

What crucial function(s) might I_{NaP} and bursting-pacemaker activity provide to the preBötC and brainstem breathing-related microcircuits? First, I_{NaP} in core preBötC neurons is required for normal augmentation of ventilation and air convection during postnatal development. Second, the present study does not exclude the possibility that I_{NaP} may be essential in a context where either cellular pacemaker properties or an additional enhancement in excitability is necessary to keep breathing viable, like in gasping (Paton *et al.*, 2006). In this interpretive framework, I_{NaP} and cellular pacemaker properties could be considered redundant rhythmogenic support mechanisms available to be recruited outside of normal physiological circumstances. Third, a rhythmogenic network dubbed the intermediate reticular oscillator (iRO) exists at the margin of, and partially overlaps, the preBötC. The iRO generates rhythmic cries in neonatal mice, which are well coordinated with breathing and appear to depend on I_{NaP} -dependent bursting-pacemaker activity (Wei *et al.*, 2022). Whereas I_{NaP} -mediated bursting-pacemaker neurons were first identified and associated with the inspiratory preBötC, these properties are ubiquitous in the ventral medulla (Rybak *et al.*, 2003) and may in fact be obligatory for rhythmogenesis of neonatal crying rather than breathing *per se*.

Regarding inspiratory rhythm, we favor an essential emergent-network mechanism of rhythmogenesis in which bursting-pacemaker neurons can be embedded but are not obligatory. The core mechanism probably involves a

subset of glutamatergic *Dbx1* neurons with common intrinsic membrane properties (Rekling *et al.*, 1996; Picardo *et al.*, 2013; Kallurkar *et al.*, 2020), which synchronize during the inter-inspiratory interval, activate output-pattern related neurons to form inspiratory bursts (Kam *et al.*, 2013; Ashhad & Feldman, 2020; Kallurkar *et al.*, 2020) that ultimately drive inspiratory breathing movements. Even if preBötC bursting-pacemaker neurons are not breathing rhythmogenic, I_{NaP} may be important to regulate breathing development, produce coordinated cries in neonates, support or generate rhythmogenesis in different physiological contexts, as well as influence baseline excitability – in conjunction with other sources of drive – in the preBötC under normal physiological conditions.

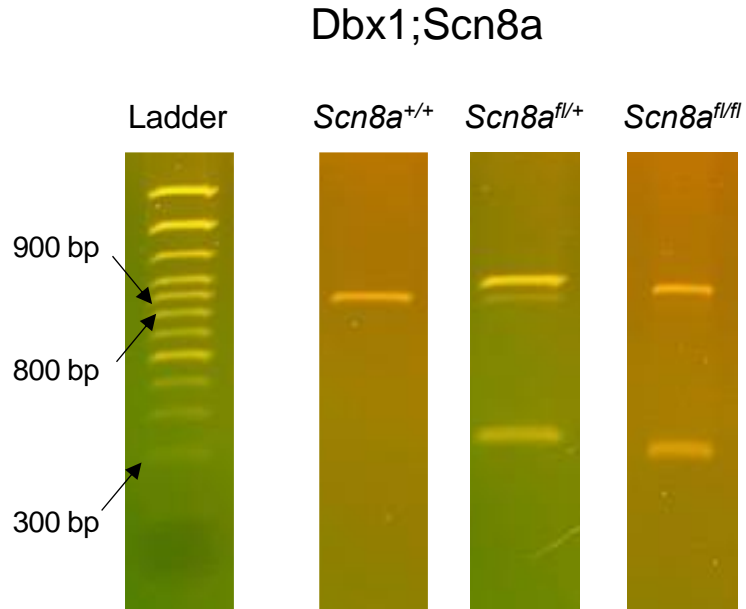
2.5.1. Limitations of the study

Cre-Lox recombination in *Dbx1*;*Scn8a* conditional knockout mice affects *Dbx1*-derived cells throughout the brain and CNS, leading to locomotor deficits that ultimately impaired normal growth. Consequently, it was impossible to record ventilation in ages older than P21 because homozygous *Dbx1*;*Scn8a*^{fl/fl} mice died. That limitation can be offset using a complementary strategy like shRNA-mediated conditional knockdown, targeting the same gene, but only in the intended preBötC core neuron population. We recorded ventilation following knockdown in adult mice but there were two limitations. First, virus spread to glutamatergic neurons outside the preBötC, some of which have respiratory pattern-related functionality. Second, shRNA knockdown diminished but did not

preclude gene expression, yet the effect was enough to significantly reduce *Scn8a* expression. Nevertheless, in tandem, our two complementary experimental approaches refute the long-standing hybrid pacemaker hypothesis of inspiratory rhythmogenesis, which is predicated on obligatory I_{NaP} and bursting-pacemaker properties. We offer a nuanced view of I_{NaP} and its role in breathing rhythmogenesis: it influences preBötC function by ordinarily boosting excitability and its influence pertains to the normal development of the ventilation perinatally.

2.6. Supplementary Information

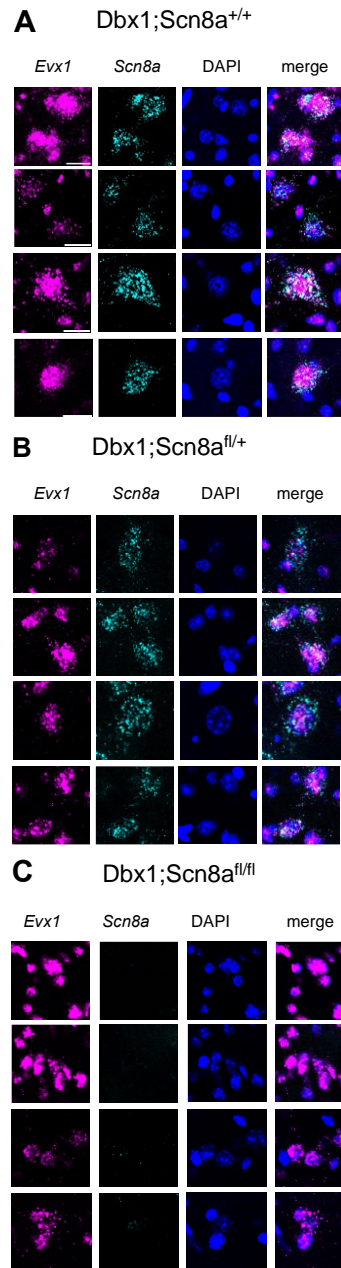
Figure S2.1



Supplementary Figure 2.1 | PCR genotyping of Dbx1;Scn8a conditional knockout mice. Related to Figure 2.3.

First lane shows a ladder with base pair (bp) sizes for reference. Second, third and fourth lanes show characteristic band pattern according to mouse genotype. Wild-type Dbx1;Scn8a^{+/+} mice (second lane) exhibit only one band at 800 bp, which reflects the wild-type *Scn8a* allele. Heterozygous Dbx1;Scn8a^{fl/+} mice (third lane) show a band at 900 bp, reflecting the floxed *Scn8a* allele in non-*Dbx1*-derived cells, a band at 300 bp, reflecting the recombined allele in *Dbx1*-derived neurons, as well as a band at 800 bp reflecting the wild-type *Scn8a* allele. Homozygous Dbx1;Scn8a^{fl/fl} mice (fourth ladder) show one band at 900 for the floxed *Scn8a* allele in non-*Dbx1*-derived cells and a band at 300 bp for the recombined allele in *Dbx1*-derived neurons, but no bands at 800 bp because the wild-type *Scn8a* allele is not present.

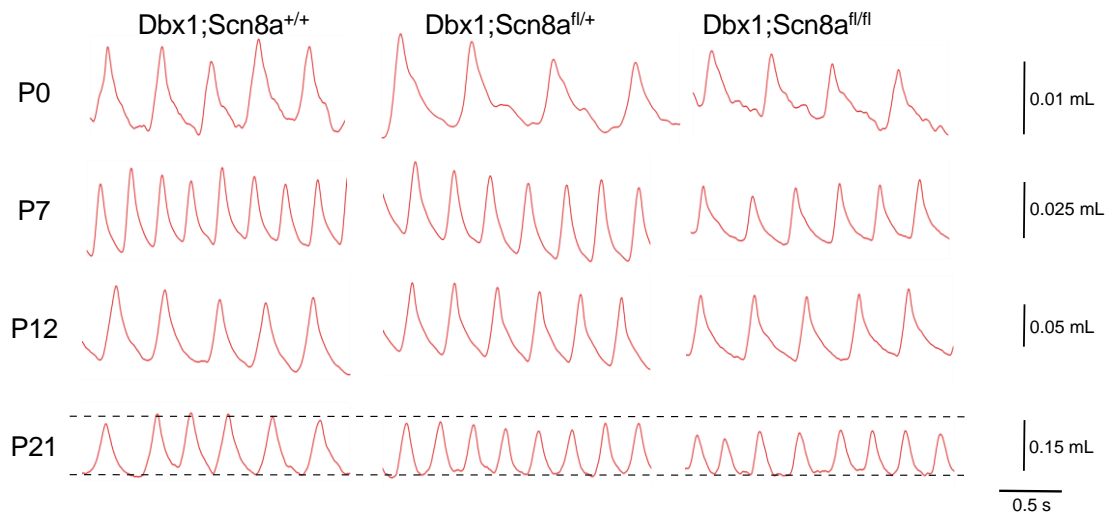
Figure S2.2



Supplementary Figure 2.2 | *in situ* hybridization showing *Scn8a* transcripts. Related to Figure 2.3.

A, B, C Photomicrographs of the RNAscope for transcripts of *Even-Skipped Homeobox 1* (*Evx1*, magenta, first column), *Scn8a* (cyan, second column), DAPI (blue, third column) and the merge of the three previous images (fourth column). RNAscope was performed in **(A)** wild-type (Dbx1;Scn8a^{+/+}), **(B)** heterozygous (Dbx1;Scn8a^{fl/+}), and **(C)** homozygous (Dbx1;Scn8a^{fl/fl}) mice at the postnatal (P) day 27–28. Calibration bars (20 μ m) in panel A apply to all images.

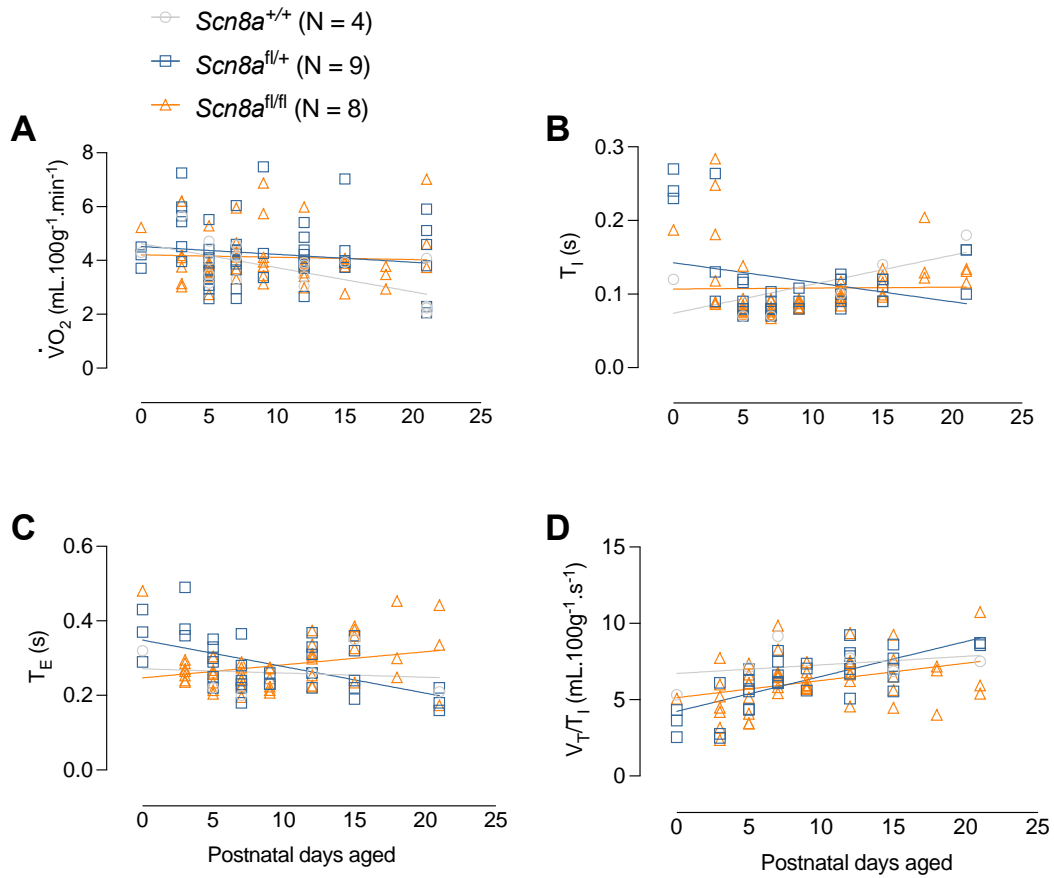
Figure S2.3



Supplementary Figure 2.3 | Conditional *Scn8a* knockout does not stop breathing but affects ventilation developmentally. Related to Figure 2.3.

Representative traces (red lines) of raw ventilatory measurements in *Dbx1;Scn8a^{+/+}* (wild-type, first column), *Dbx1;Scn8a^{fl/+}* (heterozygous, second column), and *Dbx1;Scn8a^{fl/fl}* (homozygous, third column) mice recorded at room air conditions (20.95% O₂ and 0.03% CO₂). Traces were sampled from specific postnatal (P) ages at P0, P7, P12 and P21. Upward deflections represent inspiration. Horizontal dashed lines at P21 show the upper and lower limits of the ventilatory signals. Calibration bars for the volume are shown to the right with time calibration.

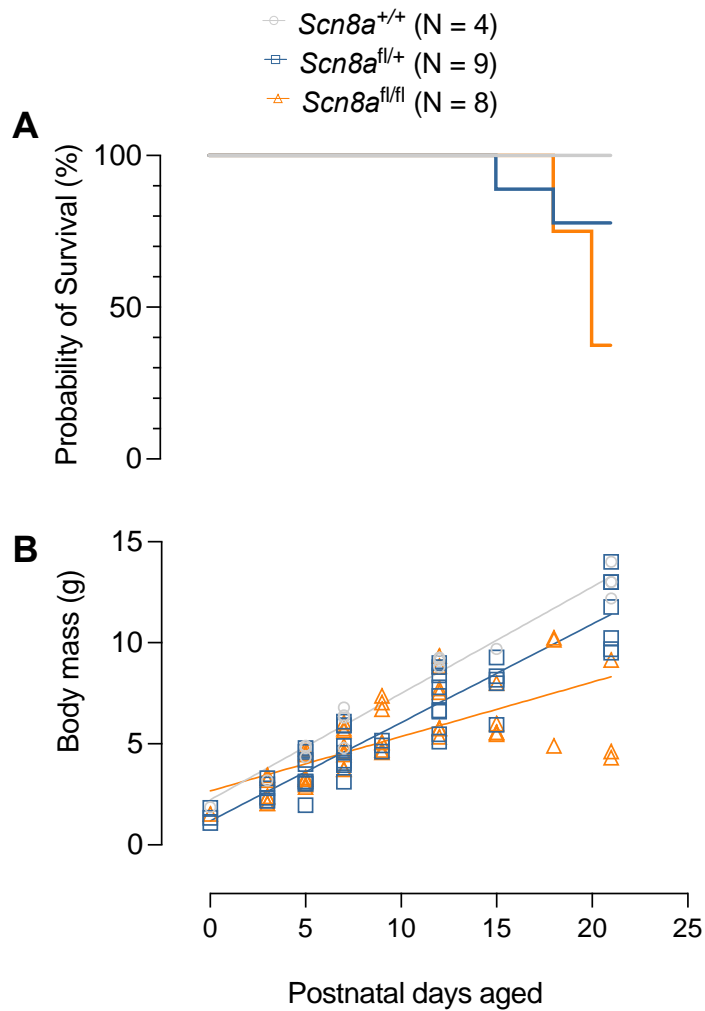
Figure S2.4



Supplementary Figure 2.4 | Breathing measurements in *Scn8a* conditional knockout mice. Related to Figure 2.3.

A, B, C, D Respiratory variables measured in *Dbx1*;*Scn8a*^{+/+} mice (wild-type, gray open circles), *Dbx1*;*Scn8a*^{fl/+} mice (heterozygous, blue open squares), and *Dbx1*;*Scn8a*^{fl/fl} mice (homozygous, orange open triangles) from P0-P21. **(A)** Oxygen consumption ($\dot{V}O_2$), **(B)** inspiratory time (T_I), **(C)** expiratory time (T_E), and **(D)** inspiratory drive (V_T/T_I). Open symbols represent individual animals. Continuous lines represent linear regression analyses for each mouse group. Genotype labels are shortened for display convenience.

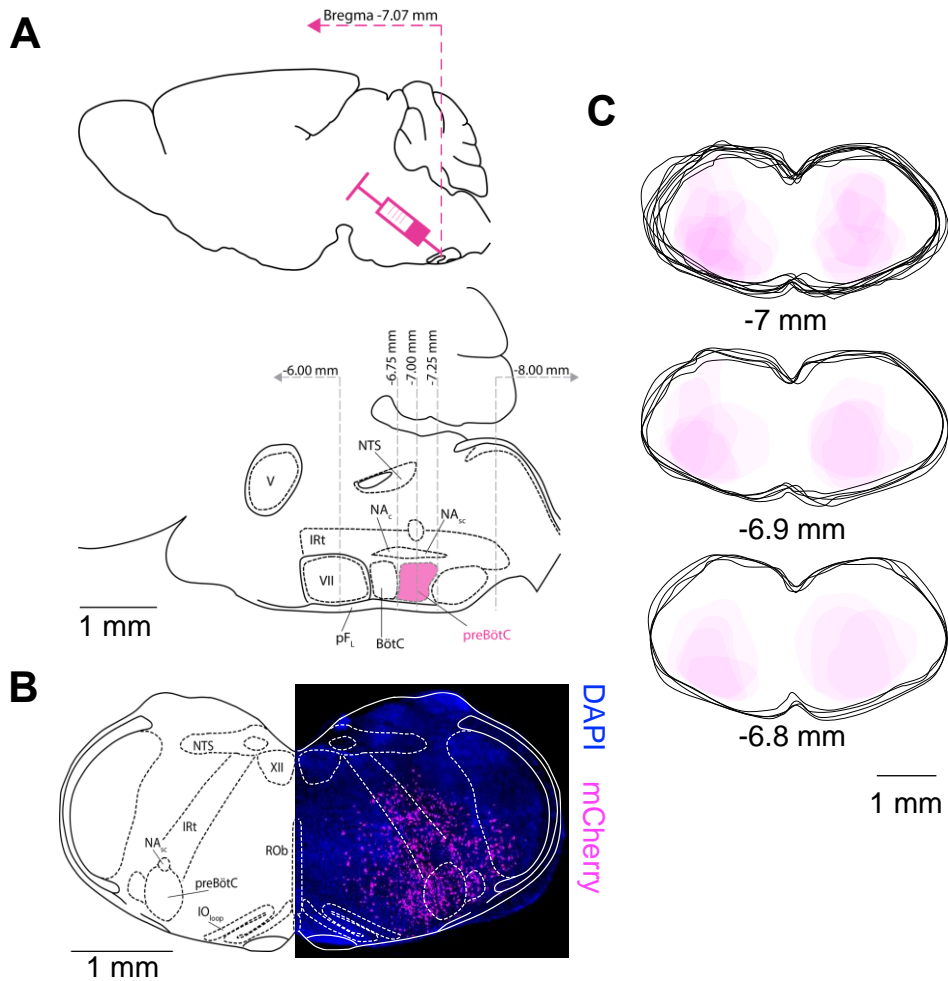
Figure S2.5



Supplementary Figure 2.5 | Survival analysis and body mass of *Scn8a* conditional knockout mice. Related to Figure 2.3.

- A** Survival analysis curves during the postnatal observation period (P0-P21) in *Dbx1;Scn8a*^{+/+} mice (wild-type, gray line), *Dbx1;Scn8a*^{fl/+} mice (heterozygous, blue line), and *Dbx1;Scn8a*^{fl/fl} mice (homozygous, orange line). The genotype labels are shortened for display convenience.
- B** Body mass in *Dbx1;Scn8a*^{+/+}, *Dbx1;Scn8a*^{fl/+}, and *Dbx1;Scn8a*^{fl/fl} mice during the observation period (P0-P21). Open symbols represent individual animals. Continuous lines represent linear regression analyses for each mouse group. Genotype labels are shortened for display convenience.

Figure S2.6

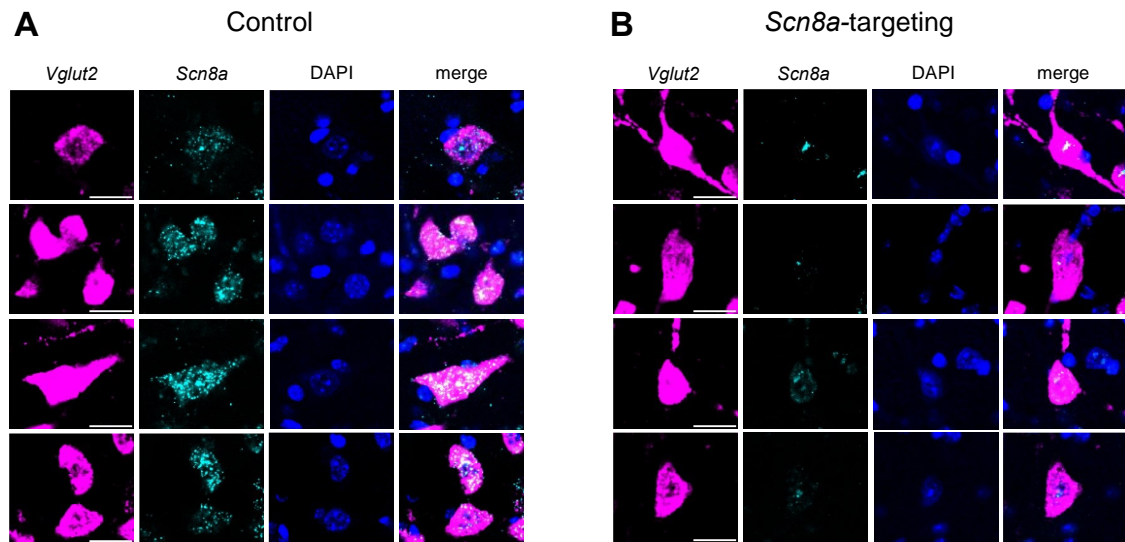


Supplementary Figure 2.6 | Short-hairpin RNA (shRNA) injection into the preBötC of Vglut2-ires-cre mice. Related to Figure 2.4.

- A** Top, schematic representation of the injection of the Adeno-associated virus serotype 9 (AAV9) carrying either a *Scn8a*-targeting or non-targeting (control) shRNA sequence. Dashed magenta line indicates anterior-posterior coordinate of the preBötC relative to Bregma. Bottom, parasagittal diagram of the ventral respiratory group in the brainstem showing the targeted injection site relative to the bregma and other landmarks. V: trigeminal cranial motor nucleus; VII: facial cranial motor nucleus; IRt: intermediate reticular formation; NTS: nucleus of the solitary tract; NA_c: nucleus ambiguus compact division; NA_{sc}: nucleus ambiguus semi-compact division; pFL: lateral parafacial respiratory group; BötC: Bötzing Complex; and preBötC: preBötzing Complex. Dashed gray lines indicate anterior-posterior coordinates relative to Bregma.
- B** Coronal section of the brainstem showing the injection site. Left, view of additional landmarks adjacent to the preBötC: XII: hypoglossal cranial motor nucleus; ROb: raphe obscurus; and IO_{loop}: loop of the inferior olive. Right, fluorescence image at 10x showing glutamatergic neurons identified by the mCherry (magenta) expression following viral infection. DAPI was used as nuclear marker to facilitate tissue visualization.
- C** Three coronal diagrams showing the distribution of viral infection at three different levels with respect to Bregma, indicated at the bottom of each diagram. Black solid lines outline the

brainstem borders, whereas the magenta shaded area represents the area covered by the mCherry-positive cells in that coronal section. Five slices, from 5 distinct animals, were superimposed at each level.

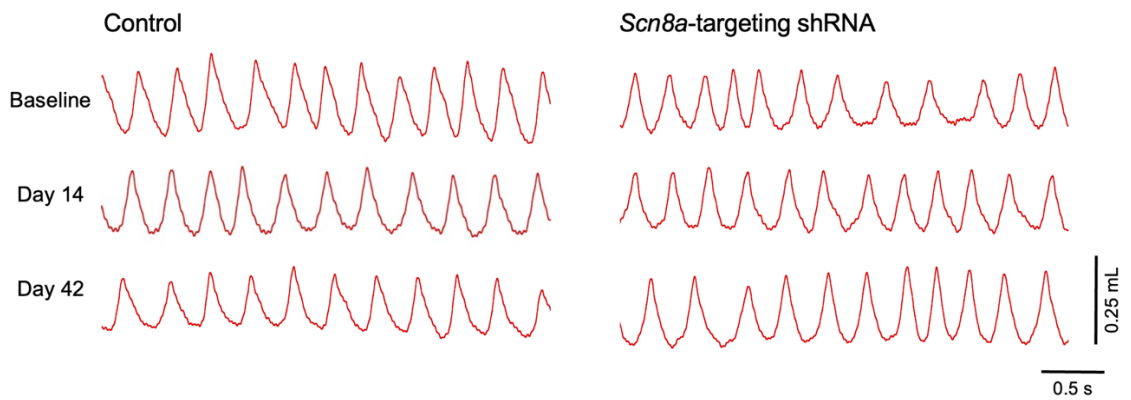
Figure S2.7



Supplementary Figure 2.7 | RNAscope of *Scn8a* transcripts following *Scn8a*-targeting and control shRNA injections in the preBötC. Related to Figure 2.4.

A, B *in situ* hybridization assay performed in brainstem coronal sections of mice injected with control **(A)** and *Scn8a*-targeting **(B)** shRNA. For each group, from left to right, first column shows *mCherry*-expressing glutamatergic (*Vglut2*, magenta) neurons; second column shows puncta of *Scn8a* transcripts (cyan); third column shows cell nuclei stained with DAPI (blue); and the fourth column shows the merge between the three previous columns. Calibration bars (20 μ m) apply to all images

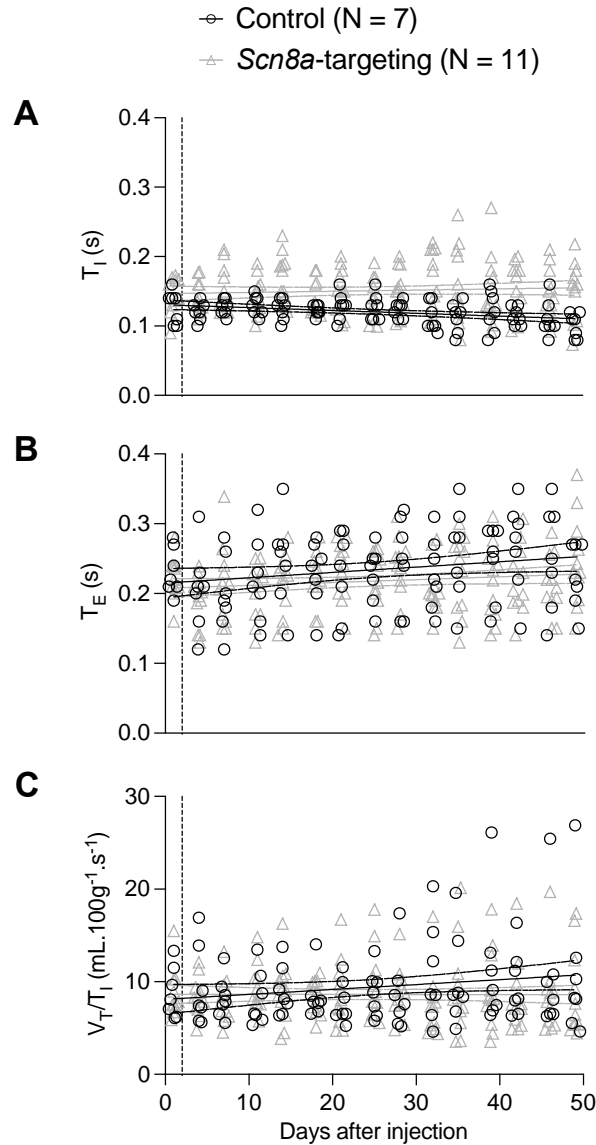
Figure S2.8



Supplementary Figure 2.8 | shRNA mediated *Scn8a* conditional knockdown does not affect ventilation in adult mice. Related to Figure 2.5.

Representative traces (red lines) of raw ventilatory measurements in mice injected with non-targeting (control, first column) or *Scn8a*-targeting (second column) shRNA, recorded in room air conditions (20.95% O₂ and 0.03% CO₂). Traces were sampled before (upper trace, baseline) and after the injection (middle and bottom traces). Upward deflections represent inspiration. Calibration bars for volume and time are shown at the lower right.

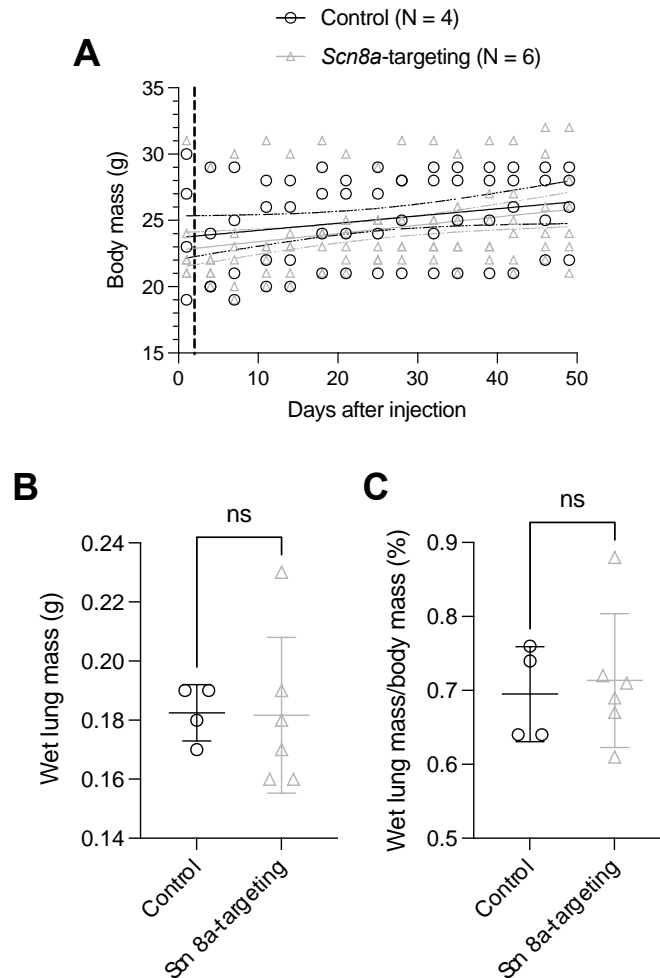
Figure S2.9



Supplementary Figure 2.9 | Breathing measurements in *Scn8a* conditional knockdown mice during the observation period. Related to Figure 5.

A, B, C Respiratory variables of mice injected with a non-targeting (control, black open circles) or *Scn8a*-targeting (gray open triangles) shRNA, measured for 49 days after injection. **(A)** Inspiratory time (T_I), **(B)** expiratory time (T_E), and **(C)** inspiratory drive (V_T/T_I). Vertical dashed lines indicate the day of the injection. Left of the vertical dashed lines are the baseline ventilatory parameters recorded before the injections, and values on the right were collected every 3 to 4 days, for 7 weeks. Individual symbols represent individual mice. Horizontal continuous lines represent the linear regression analyses for each group with dashed lines indicating the 95% confidence intervals.

Figure S2.10



Supplementary Figure 2.10 | Body mass of *Scn8a* conditional knockdown mice during the observation period and lung mass at the end of the study. Related to Figure 2.4 and Figure 2.5.

- A** Body mass of mice injected with a non-targeting (control, black open circles) or *Scn8a*-targeting (gray open triangles) shRNA, measured for 49 days after injection. Vertical dashed lines indicate the day of the injection. Left of the vertical dashed lines are the body masses before the injections, and values on the right were collected every 3 to 4 days, for 7 weeks. Individual symbols represent individual mice. Horizontal continuous lines represent the linear regression analyses for each group with dashed lines indicating the 95% confidence intervals.
- B, C** Wet lung mass (**B**) and wet lung mass scaled by the body mass (**C**) of *Vglut2-ires-cre* mice injected with non-targeting (control, black open circles) and *Scn8a*-targeting (gray open triangles) shRNA. Lungs were weighed at the end of the study. Each symbol represents one animal with mean \pm SD.

2.7. References

- Ashhad S & Feldman JL (2020). Emergent Elements of Inspiratory Rhythmogenesis: Network Synchronization and Synchrony Propagation. *Neuron* **106**, 482-497.e4.
- Ashhad S, Kam K, Negro CA del & Feldman JL (2022). Breathing Rhythm and Pattern and Their Influence on Emotion. *Annu Rev Neurosci*; DOI: 10.1146/ANNUREV-NEURO-090121-014424.
- Bankhead P, Loughrey MB, Fernández JA, Dombrowski Y, McArd DG, Dunne PD, McQuaid S, Gray RT, Murray LJ, Coleman HG, James JA, Salto-Tellez M & Hamilton PW (2017). QuPath: Open source software for digital pathology image analysis. *Sci Rep*; DOI: 10.1038/s41598-017-17204-5.
- Bellingham MC (2011). A review of the neural mechanisms of action and clinical efficiency of riluzole in treating amyotrophic lateral sclerosis: what have we learned in the last decade? *CNS Neurosci Ther* **17**, 4–31.
- Bielle F, Griveau A, Narboux-Nême N, Vigneau S, Sigrist M, Arber S, Wassef M & Pierani A (2005). Multiple origins of Cajal-Retzius cells at the borders of the developing pallium. *Nat Neurosci* **8**, 1002–1012.
- Bouvier J, Thoby-Brisson M, Renier N, Dubreuil V, Ericson J, Champagnat J, Pierani A, Chédotal A & Fortin G (2010). Hindbrain interneurons and axon guidance signaling critical for breathing. *Nat Neurosci* **13**, 1066–1074.
- Burbidge SA, Dale TJ, Powell AJ, Whitaker WRJ, Xie XM, Romanos MA & Clare JJ (2002). Molecular cloning, distribution and functional analysis of the NA(V)1.6. Voltage-gated sodium channel from human brain. *Brain Res Mol Brain Res* **103**, 80–90.
- Butera RJ, Rinzel J & Smith JC (1999). Models of respiratory rhythm generation in the pre-Bötzinger complex. I. Bursting pacemaker neurons. *J Neurophysiol* **82**, 382–397.
- Calin-Jageman RJ & Cumming G (2019). Estimation for Better Inference in Neuroscience. *eNeuro*; DOI: 10.1523/ENEURO.0205-19.2019.
- Chang K, Marran K, Valentine A & Hannon GJ (2013). Creating an miR30-based shRNA vector. *Cold Spring Harb Protoc* **2013**, 631–635.
- Chen Y, Yu FH, Sharp EM, Beacham D, Scheuer T & Catterall WA (2008). Functional properties and differential neuromodulation of Nav1.6 channels. *Molecular and Cellular Neuroscience* **38**, 607–615.

Chevalier M, Toporikova N, Simmers J & Thoby-Brisson M (2016). Development of pacemaker properties and rhythmogenic mechanisms in the mouse embryonic respiratory network. *Elife*; DOI: 10.7554/ELIFE.16125.

Cummings KJ, Hewitt JC, Li A, Daubenspeck JA & Nattie EE (2011). Postnatal loss of brainstem serotonin neurones compromises the ability of neonatal rats to survive episodic severe hypoxia. *J Physiol* **589**, 5247–5256.

David CK, Sugimura YK, Kallurkar PS, Picardo MCD, Saha MS, Conradi Smith GD & Del Negro CA (2022). Single cell transcriptome sequencing of inspiratory neurons of the preBötzinger complex in neonatal mice. *Sci Data* **9**, 457.

Do MTH & Bean BP (2004). Sodium currents in subthalamic nucleus neurons from Nav1.6-null mice. *J Neurophysiol* **92**, 726–733.

Doble A (1996). The pharmacology and mechanism of action of riluzole. *Neurology*; DOI: 10.1212/WNL.47.6_SUPPL_4.233S.

Dow LE, Premsrirut PK, Zuber J, Fellmann C, McJunkin K, Miething C, Park Y, Dickins RA, Hannon GJ & Lowe SW (2012). A pipeline for the generation of shRNA transgenic mice. *Nat Protoc* **7**, 374.

Drorbaugh JE & Fenn WO (1955). A barometric method for measuring ventilation in newborn infants. *Pediatrics* **16**, 81–87.

Enomoto A, Han JM, Hsiao CF & Chandler SH (2007). Sodium currents in mesencephalic trigeminal neurons from Nav1.6 null mice. *J Neurophysiol* **98**, 710–719.

Feldman JL & Kam K (2015). Facing the challenge of mammalian neural microcircuits: Taking a few breaths may help. *Journal of Physiology* **593**, 3–23.

Funk GD, Smith JC & Feldman JL (1993). *Generation and Transmission of Respiratory Oscillations in Medullary Slices: Role of Excitatory Amino Acids*.

Gray PA, Hayes JA, Ling GY, Llona I, Tupal S, Picardo MCD, Ross SE, Hirata T, Corbin JG, Eugenin J & Del Negro CA (2010). Developmental Origin of PreBotzinger Complex Respiratory Neurons. *Journal of Neuroscience* **30**, 14883–14895.

Guyenet PG, Stornetta RL, Souza GMPR, Abbott SBG, Shi Y & Bayliss DA (2019). The retrotrapezoid nucleus: central chemoreceptor and regulator of breathing automaticity. *Trends Neurosci* **42**, 807.

Hayes JA, Kottick A, Picardo MCD, Halleran AD, Smith RD, Smith GD, Saha MS & Del Negro CA (2017). Transcriptome of neonatal preBötzinger complex neurones in Dbx1 reporter mice. *Scientific Reports* 2017 7:1 **7**, 1–13.

Jacky JP (1978). A plethysmograph for long-term measurements of ventilation in unrestrained animals. *J Appl Physiol Respir Environ Exerc Physiol* **45**, 644–647.

Johnson SM, Smith JC, Funk GD & Feldman JL (1994). Pacemaker behavior of respiratory neurons in medullary slices from neonatal rat. *J Neurophysiol* **72**, 2598–2608.

Kallurkar PS, Grover C, Picardo MCD & Del Negro CA (2020). Evaluating the Burstlet Theory of Inspiratory Rhythm and Pattern Generation. *eNeuro*; DOI: 10.1523/ENEURO.0314-19.2019.

Kallurkar PS, Picardo MCD, Sugimura YK, Saha MS, Conradi Smith GD & Del Negro CA (2022). Transcriptomes of electrophysiologically recorded Dbx1-derived respiratory neurons of the preBötzinger complex in neonatal mice. *Sci Rep*; DOI: 10.1038/S41598-022-06834-Z.

Kam K, Worrell JW, Janczewski WA, Cui Y & Feldman JL (2013). Distinct Inspiratory Rhythm and Pattern Generating Mechanisms in the preBötzinger Complex. *The Journal of Neuroscience* **33**, 9235.

Kiehn O (2016). Decoding the organization of spinal circuits that control locomotion. *Nature Reviews Neuroscience* 2016 17:4 **17**, 224–238.

Koizumi H, John TT, Chia JX, Tariq MF, Phillips RS, Mosher B, Chen Y, Thompson R, Zhang R, Koshiya N & Smith JC (2018). Transient Receptor Potential Channels TRPM4 and TRPC3 Critically Contribute to Respiratory Motor Pattern Formation but not Rhythmogenesis in Rodent Brainstem Circuits. *eNeuro* **5**, 332–349.

Koizumi H & Smith JC (2008). Persistent Na⁺ and K⁺-Dominated Leak Currents Contribute to Respiratory Rhythm Generation in the Pre-Bötzinger Complex In Vitro. *The Journal of Neuroscience* **28**, 1773.

Koizumi H, Wilson CG, Wong S, Yamanishi T, Koshiya N & Smith JC (2008). Functional Imaging, Spatial Reconstruction, and Biophysical Analysis of a Respiratory Motor Circuit Isolated In Vitro. *The Journal of Neuroscience* **28**, 2353.

Koshiya N & Smith JC (1999). Neuronal pacemaker for breathing visualized in vitro. *Nature* 1999 400:6742 **400**, 360–363.

Koteja P (1996). Measuring Energy Metabolism with Open-Flow Respirometric Systems: Which Design to Choose? *Funct Ecol* **10**, 675.

Leary S, Underwood W, Anthony R, Cartner S, Grandin T, Greenacre C, Gwaltney-Brant S, McCrackin M, Meyer R, Miller D, Shearer J, Turner T & Yanong R (2020). *AVMA guidelines for the euthanasia of animals: 2020 edition*. American Veterinary Medical Association (AVMA), Schaumburg, IL.

- Levin SI & Meisler MH (2004). Floxed allele for conditional inactivation of the voltage-gated sodium channel *Scn8a* (NaV1.6). *Genesis* **39**, 234–239.
- Lu B, Su Y, Das S, Liu J, Xia J & Ren D (2007). The Neuronal Channel NALCN Contributes Resting Sodium Permeability and Is Required for Normal Respiratory Rhythm. *Cell* **129**, 371–383.
- MacIver MB, Amagasa SM, Mikulec AA & Monroe FA (1996). Riluzole anesthesia: use-dependent block of presynaptic glutamate fibers. *Anesthesiology* **85**, 626–634.
- Maurice N, Tkatch T, Meisler M, Sprunger LK & Surmeier DJ (2001). D1/D5 Dopamine Receptor Activation Differentially Modulates Rapidly Inactivating and Persistent Sodium Currents in Prefrontal Cortex Pyramidal Neurons. *The Journal of Neuroscience* **21**, 2268.
- Meisler MH, Kearney J, Escayg A, MacDonald BT & Sprunger LK (2001). Sodium channels and neurological disease: insights from *Scn8a* mutations in the mouse. *Neuroscientist* **7**, 136–145.
- Meisler MH, Plummer NW, Burgess DL, Buchner DA & Sprunger LK (2004). Allelic mutations of the sodium channel *SCN8A* reveal multiple cellular and physiological functions. *Genetica* **122**, 37–45.
- Moore JD, Deschênes M, Furuta T, Huber D, Smear MC, Demers M & Kleinfeld D (2013). Hierarchy of orofacial rhythms revealed through whisking and breathing. *Nature* **497**, 205–210.
- Moran-Rivard L, Kagawa T, Saueressig H, Gross MK, Burrill J & Goulding M (2001). *Evx1* is a postmitotic determinant of V0 interneuron identity in the spinal cord. *Neuron* **29**, 385–399.
- Mortola JP (1984). Breathing pattern in newborns. *J Appl Physiol Respir Environ Exerc Physiol* **56**, 1533–1540.
- Mortola JP & Frappell PB (1998). On the barometric method for measurements of ventilation, and its use in small animals. *Can J Physiol Pharmacol* **76**, 937–944.
- Mortola JP & Frappell PB (2013). Measurements of air ventilation in small vertebrates. *Respir Physiol Neurobiol* **186**, 197–205.
- National Research Council (2011). *Guide for the Care and Use of Laboratory Animals*. National Academies Press (US), Washington (DC). Available at: <https://www.ncbi.nlm.nih.gov/books/NBK54050/> [Accessed July 31, 2022].
- Del Negro CA, Funk GD & Feldman JL (2018). Breathing matters. *Neuroscience* **19**, 351–367.

- Del Negro CA, Koshiya N, Butera RJ & Smith JC (2002a). Persistent sodium current, membrane properties and bursting behavior of pre-Bötzinger complex inspiratory neurons in vitro. *J Neurophysiol* **88**, 2242–2250.
- Del Negro CA, Morgado-Valle C & Feldman JL (2002b). Respiratory rhythm: an emergent network property? *Neuron* **34**, 821–830.
- Del Negro CA, Morgado-Valle C, Hayes JA, Mackay DD, Pace RW, Crowder EA & Feldman JL (2005). Sodium and calcium current-mediated pacemaker neurons and respiratory rhythm generation. *Journal of Neuroscience* **25**, 446–453.
- Pace RW, Mackay DD, Feldman JL & Del Negro CA (2007). Role of persistent sodium current in mouse preBötzinger Complex neurons and respiratory rhythm generation. *Journal of Physiology* **580**, 485–496.
- Pagliardini S, Adachi T, Ren J, Funk GD & Greer JJ (2005). Fluorescent tagging of rhythmically active respiratory neurons within the pre-Bötzinger complex of rat medullary slice preparations. *J Neurosci* **25**, 2591–2596.
- Paton JFR, Abdala APL, Koizumi H, Smith JC & St-John WM (2006). Respiratory rhythm generation during gasping depends on persistent sodium current. *Nat Neurosci* **9**, 311–313.
- Paxinos G & Franklin KBJ (2019). *Paxinos and Franklin's the Mouse Brain in Stereotaxic Coordinates*, 5th edn. Academic Press. Available at: <https://www.elsevier.com/books/paxinos-and-franklins-the-mouse-brain-in-stereotaxic-coordinates-compact/franklin/978-0-12-816159-3> [Accessed October 26, 2021].
- Peña F, Parkis MA, Tryba AK & Ramirez JM (2004). Differential contribution of pacemaker properties to the generation of respiratory rhythms during normoxia and hypoxia. *Neuron* **43**, 105–117.
- Percie du Sert N et al. (2020). The ARRIVE guidelines 2.0: Updated guidelines for reporting animal research. *Exp Physiol* **105**, 1459–1466.
- Phillips RS, Koizumi H, Molkov YI, Rubin JE & Smith JC (2022). Predictions and experimental tests of a new biophysical model of the mammalian respiratory oscillator. *Elife* **11**, 74762.
- Phillips RS & Rubin JE (2019). Effects of persistent sodium current blockade in respiratory circuits depend on the pharmacological mechanism of action and network dynamics. *PLoS Comput Biol*; DOI: 10.1371/JOURNAL.PCBI.1006938.
- Picardo MCD, Sugimura YK, Dorst KE, Kallurkar PS, Akins VT, Ma X, Teruyama R, Guinamard R, Kam K, Saha MS & Negro CA Del (2019). Trpm4 ion channels in pre-Bötzinger complex interneurons are essential for breathing motor pattern but not rhythm. *PLoS Biol*; DOI: 10.1371/JOURNAL.PBIO.2006094.

- Picardo MCD, Weragalaarachchi KTH, Akins VT & Del Negro CA (2013). Physiological and morphological properties of Dbx1-derived respiratory neurons in the pre-Bötzinger complex of neonatal mice. *Journal of Physiology* **591**, 2687–2703.
- Ptak K, Zummo GG, Alheid GF, Tkatch T, Surmeier DJ & McCrimmon DR (2005). Sodium currents in medullary neurons isolated from the pre-Bötzinger complex region. *J Neurosci* **25**, 5159–5170.
- Purvis LK, Smith JC, Koizumi H & Butera RJ (2007). Intrinsic bursters increase the robustness of rhythm generation in an excitatory network. *J Neurophysiol* **97**, 1515–1526.
- Raman IM, Sprunger LK, Meisler MH & Bean BP (1997). Altered subthreshold sodium currents and disrupted firing patterns in Purkinje neurons of Scn8a mutant mice. *Neuron* **19**, 881–891.
- Ramirez JM & Baertsch N (2018a). Defining the rhythmogenic elements of mammalian breathing. *Physiology* **33**, 302–316.
- Ramirez JM & Baertsch NA (2018b). The Dynamic Basis of Respiratory Rhythm Generation: One Breath at a Time. *Annu Rev Neurosci* **41**, 475.
- Rekling JC, Champagnat J & Denavit-Saubié M (1996). Electroresponsive properties and membrane potential trajectories of three types of inspiratory neurons in the newborn mouse brain stem in vitro. *J Neurophysiol* **75**, 795–810.
- Ren D (2011). Sodium Leak Channels in Neuronal Excitability and Rhythmic Behaviors. *Neuron* **72**, 899.
- Revoll AL, Vann NC, Akins VT, Kottick A, Gray PA, Del Negro CA & Funk GD (2015). Dbx1 precursor cells are a source of inspiratory XII premotoneurons. *Elife*; DOI: 10.7554/eLife.12301.
- Ruangkittisakul A, Kottick A, Picardo MCD, Ballanyi K & Negro CA del (2014). Identification of the pre-Bötzinger complex inspiratory center in calibrated “sandwich” slices from newborn mice with fluorescent Dbx1 interneurons. *Physiol Rep*; DOI: 10.14814/PHY2.12111.
- Rybak IA, Ptak K, Shevtsova NA & McCrimmon DR (2003). Sodium currents in neurons from the rostroventrolateral medulla of the rat. *J Neurophysiol* **90**, 1635–1642.
- Schindelin J, Arganda-Carreras I, Frise E, Kaynig V, Longair M, Pietzsch T, Preibisch S, Rueden C, Saalfeld S, Schmid B, Tinevez JY, White DJ, Hartenstein V, Eliceiri K, Tomancak P & Cardona A (2012). Fiji - an Open Source platform for biological image analysis. *Nat Methods* **9**, 676–682.

Smith JC, Ellenberger HH, Ballanyi K, Richter DW & Feldman JL (1991). Pre-Bötzing complex: a brainstem region that may generate respiratory rhythm in mammals. *Science* **254**, 726–729.

Smith MR, Smith RD, Plummer NW, Meisler MH & Goldin AL (1998). Functional Analysis of the Mouse Scn8a Sodium Channel. *The Journal of Neuroscience* **18**, 6093.

Takatoh J, Prevosto V, Thompson PM, Lu J, Chung L, Harrahill A, Li S, Zhao S, He Z, Golomb D, Kleinfeld D & Wang F (2022). The whisking oscillator circuit. *Nature* **609**, 560–568.

Talpalar AE, Bouvier J, Borgius L, Fortin G, Pierani A & Kiehn O (2013). Dual-mode operation of neuronal networks involved in left–right alternation. *Nature* **500**, 85–88.

Thoby-Brisson M & Ramirez JM (2001). Identification of two types of inspiratory pacemaker neurons in the isolated respiratory neural network of mice. *J Neurophysiol* **86**, 104–112.

Wallén-Mackenzie Å, Gezelius H, Thoby-Brisson M, Nygård A, Enjin A, Fujiyama F, Fortin G & Kullander K (2006). Vesicular glutamate transporter 2 is required for central respiratory rhythm generation but not for locomotor central pattern generation. *Journal of Neuroscience* **26**, 12294–12307.

Wei XP, Collie M, Dempsey B, Fortin G & Yackle K (2022). A novel reticular node in the brainstem synchronizes neonatal mouse crying with breathing. *Neuron* **110**, 644-657.e6.

Yamanishi T, Koizumi H, Navarro MA, Milesescu LS & Smith JC (2018). Kinetic properties of persistent Na⁺ current orchestrate oscillatory bursting in respiratory neurons. *J Gen Physiol* **150**, 1523–1540.

Yang CF, Kim EJ, Callaway EM & Feldman JL (2020). Monosynaptic Projections to Excitatory and Inhibitory preBötzing Complex Neurons. *Front Neuroanat* **14**, 58.

Zybura A, Hudmon A & Cummins TR (2021). Distinctive properties and powerful neuromodulation of Nav 1.6 sodium channels regulates neuronal excitability. *Cells*; DOI: 10.3390/cells10071595.

Chapter 3: Evaluating the role of KCNQ ion channels in breathing rhythmogenesis and opioid-induced respiratory depression in adult mice

3.1. Abstract

Rhythm and pattern information for inspiratory breathing movements emanates from the preBötzinger Complex (preBötC). Although the ionic and synaptic mechanisms that initiate and sustain inspiratory bursts are well understood, those involved in burst termination remain unclear. Furthermore, the mechanisms by which opioids depress breathing are not well understood either.

KCNQ2/KCNQ3 heteromeric ion channels underlying M-type potassium currents have been associated with both burst termination and opioid-induced respiratory depression (OIRD) due to their subthreshold voltage dependence and non-inactivating kinetics. We tested those roles using short-hairpin RNA (shRNA) to knock down *Kcnq2* and *Kcnq3*, thus M-currents, in preBötC glutamatergic neurons. We predicted that this attenuation would slow down breathing by increasing inspiratory time and blunt the effects of opioid drugs. Surprisingly, we found that KCNQ2/KCNQ3 currents neither influence inspiratory breath duration nor mediate the depressant effects of opioid drugs because knockdown of *Kcnq2/Kcnq3* subunits by more than 50% in the preBötC of adult mice did not affect any measures of breathing including the depressant effects of fentanyl. Our results do not refute existing explanations for burst termination involving synaptic depression and non-M-type intrinsic currents, nor do they contradict the role of non-gated potassium channels and presynaptic inhibition in OIRD.

3.2. Introduction

Central pattern generator (CPG) networks produce rhythmic neural activity that drives motor behaviors like locomotion, swimming, chewing, and licking (Delcomyn, 1980; Grillner & El Manira, 2020; Northcutt & Schulz, 2020).

Likewise, breathing involves rhythmic movements of the diaphragm to ventilate the lungs. The core CPG for breathing resides in the preBötzinger Complex (preBötC), a bilateral site in the ventral medulla that specifically drives inspiration, the inexorable active phase of breathing (Smith *et al.*, 1991; Del Negro *et al.*, 2018; Ramirez & Baertsch, 2018*b*, 2018*a*; Ashhad *et al.*, 2022). preBötC rhythmogenic interneurons are glutamatergic (Funk *et al.*, 1993; Wallén-Mackenzie *et al.*, 2006), and derived from precursors cells expressing the transcription factor Developing Brain Homeobox 1 (Dbx1) (Bouvier *et al.*, 2010; Gray *et al.*, 2010; Wang *et al.*, 2014; Vann *et al.*, 2018).

The intrinsic ionic and synaptic mechanisms that initiate and sustain inspiratory bursts in preBötC neurons are well resolved, and they involve postsynaptic excitatory amino acid receptors, as well as persistent sodium and mixed cationic inward currents (Smith *et al.*, 1991; Del Negro *et al.*, 2005; Koizumi & Smith, 2008; Ashhad *et al.*, 2022; da Silva *et al.*, 2023; Phillips & Baertsch, 2024).

Nevertheless, we have only a limited understanding of how inspiratory bursts terminate.

Mechanisms that rely on synaptic inhibition for burst termination are analogous to locomotor “half-center” models (Stuart & Hultborn, 2008; Grillner & El Manira,

2020). They posit that mutual inhibition between the Böttinger Complex (BötC) and the preBötC compel inspiratory burst termination, thereby maintaining a normal respiratory rhythm (Burns, 1963; Richter *et al.*, 1992; Smith *et al.*, 2007; Rubin *et al.*, 2009; Feldman *et al.*, 2013; Marchenko *et al.*, 2016). However, inhibitory synaptic blockade does not preclude breathing *in vivo* or inspiratory rhythm and motor output *in vitro*, which contradicts the essential role proposed for synaptic inhibition in inspiratory burst termination (Janczewski *et al.*, 2013; Hülsmann *et al.*, 2021). Nonetheless, synaptic inhibition potently influences the breathing frequency *in vivo* and breathing-related activity *in vitro* (Sherman *et al.*, 2015; Cregg *et al.*, 2017; Baertsch *et al.*, 2018; Fortuna *et al.*, 2019).

Intrinsic currents that contribute to burst termination include electrogenic outward current generated by Na⁺/K⁺ ATPase (I_{pump}), Na⁺-dependent K⁺ current ($I_{\text{K-Na}}$), and ATP-dependent K⁺ current ($I_{\text{K-ATP}}$) (Del Negro *et al.*, 2009; Krey *et al.*, 2010). Synaptic depression is also involved in burst termination because repetitive spiking during a burst depletes presynaptic vesicles that would otherwise sustain recurrent excitation (Guerrier *et al.*, 2015; Kottick & Del Negro, 2015).

The subthreshold, non-inactivating M-current is attributed to the voltage-gated K⁺ channels of the Kv7 family, with five subunits (KCNQ1-KCNQ5) (Brown & Adams, 1980; Watanabe *et al.*, 2000; Rogawski & Bazil, 2008; Maljevic *et al.*, 2008). KCNQ2 and KCNQ3 are typically co-expressed, forming heterotetramers, and are present in the preBötC (Dalby-Brown *et al.*, 2006; Geiger *et al.*, 2006; Hayes *et al.*, 2017). M-current may contribute to inspiratory burst termination because KCNQ activator drugs decrease inspiratory frequency *in vitro* by

prolonging bursts (Wei & Ramirez, 2019; Revill *et al.*, 2021) and reduce breathing frequency of neonatal and adult mice (Wei & Ramirez, 2019). Moreover, M-current (i.e., KCNQ2/KCNQ3 ion channels) may also contribute to opioid-induced respiratory depression (OIRD) as well because KCNQ activator drugs and blockers mimicked and reversed a model of OIRD *in vitro*, respectively (Wei & Ramirez, 2019; Ramirez *et al.*, 2021).

Despite its apparent role in inspiratory burst termination and OIRD, the use of agonists and/or inhibitory drugs to modulate KCNQ2/KCNQ3 activity may have undesired off-target effects (i.e., modulation in other brainstem areas) that can be counteracted by using inhibitory genetic technology which provides better target specificity. Therefore, we hypothesize that if KCNQ2/KCNQ3-mediated M-currents play a role in terminating breaths and mediates OIRD, then their conditional knockdown would prolong breathing frequency by increasing inspiratory time and blunt the effects of exogenous opioid drugs.

3.3. Material & Methods

3.3.1. Mice

Vglut2-ires-cre mice (Jackson Laboratory [JAX] *Slc17a6^{tm2(cre)Low}/J*, strain #016963, RRID:IMSR_JAX:016963) of both sexes, 10-14 weeks old, were used. Up to 4 mice were housed together in colony cages on a 12 h:12 h light/dark cycle with controlled humidity and temperature at 24° C and fed *ad libitum* on a

standard commercial mouse diet (Teklad Global Diets, Envigo, Indianapolis, IN) with free access to water. Male wild-type mice (C57BL/6J, JAX strain #000664, RRID:IMSR_JAX:000664), with body mass of 27 ± 1 g, were used exclusively to test the ventilatory and metabolic responses to different doses of intraperitoneal (i.p) injection of fentanyl citrate (2,500 mg/50 mL, Covetrus, Dublin, Ohio). Wild-type mice were housed in the same conditions.

Three cohorts of *Vglut2-ires-cre* mice were used for RNAscope (one for each time point evaluated); two cohorts of *Vglut2-ires-cre* mice were used for ventilatory and metabolic recordings after *Kcnq2/Kcnq3*-targeting and non-targeting (control) shRNA injections (one for each injection group); and finally, four cohorts of *Vglut2-ires-cre* (2 doses x 2 injection groups) and 2 cohorts of C57BL6J mice (2 doses) were used to evaluate the role of *KCNQ2/KCNQ3*-mediated M-currents in the response to 200 μ g/Kg and 400 μ g/Kg doses of fentanyl.

The protocols were approved by the Institutional Animal Care and Use Committee (IACUC) at William & Mary (IACUC-2021-04-20-14958-cadeln), which conformed to the policies of the Office of Laboratory Animal Welfare (National Institutes of Health) and the guidelines of the National Research Council (National Research Council, 2011). Protocols also followed the Institutional Biosafety Committee for using infectious agents (virus) (IBC-2022-08-07-15768-mrdegu).

3.3.2. Surgical procedures

shRNA injections in the preBötC. We administered a Cre-dependent adeno-associated virus of serotype 9 (AAV9) containing genetic information to produce a shRNA to specifically target two sequences of *Kcnq2* (NCBI ID 16536):

- **GCCGTTCTGTGTGATTGATAT – CDS 695-715,**
- **CCAGGGAATGAACTCTAGTTT – 3' UTR 7991-8011**

As well as two sequences of *Kcnq3* (NCBI ID: 110862):

- **CCTACAGACAAGAATAGATAT – CDS 1692-1712,**
- **GCGCATCCAAACTTTGATCTA – CDS 318-338**

The two constructs were packaged together into AAV9 delivery vector, then ultra-purified and produced at a titer of $> 10^{13}$ GC/mL. The AAV9 also carried a gene to express *mCherry* fluorophore. The virus employed a FLEX construct with a synapsin promoter in a miR30 backbone. Both *mCherry* and *Kcnq2/Kcnq3* shRNA sequences were in reverse orientation and flanked by double *loxP* sites. The presence of Cre recombined the allele sequences, thus expressing both *mCherry* and shRNA.

Mice were separated into two injection groups: those receiving the *Kcnq2/Kcnq3*-targeting shRNA (knockdown group), and those receiving the virus in a scrambled version (control group). The person performing the injections was blinded to the content of each vial, which were labeled randomly by a third person.

Control and targeting shRNA viruses were injected in the preBötC via stereotaxic surgery. Mice were anesthetized via isoflurane (5% v/v for induction, and 2% v/v for maintenance), and positioned in a stereotaxic frame. The skull was exposed, aseptically cleaned, and then two holes were drilled at the coordinates: 6.9-6.8 mm caudal to bregma, \pm 1.2 mm lateral to midline (targeting left and right sides), at a dorsal-ventral depth of -5.2 mm from the brain surface (Picardo *et al.*, 2019; da Silva *et al.*, 2023). We injected 50 nL of the virus using a 30-gauge 0.5 μ L Hamilton Neurosyringe (Hamilton Company, Reno, NV). After 3 days of recovery from the surgery, whole-body plethysmography (WBP) was conducted according to the protocols below.

Additionally, three other cohorts of animals were also injected following the same protocol for a semi-quantitative evaluation of the *Kcnq2/Kcnq3* mRNA expression in glutamatergic preBötC neurons via *in situ* hybridization (RNAscope). One cohort was assessed at 2 weeks after the surgery, the second was evaluated at 4 weeks, and the last cohort was evaluated at 8 weeks after the injection. Different cohorts of animals were used for each time point because mice had to be sacrificed and their brainstem processed.

Implantation of the temperature sensors. Mice whose breathing was evaluated using whole-body plethysmography had their body temperature measured to calculate tidal volume (V_T). A \varnothing 2.12 mm x 13 mm temperature sensing transponder (BioTherm 13, Biomark, Boise, Idaho) was inserted in the abdominal

cavity to via laparotomy. Mice were anesthetized using isoflurane (5% v/v for induction, and 2% v/v for maintenance) and positioned dorsally. Hair of the abdominal region was shaved, and the skin was aseptically cleaned with chlorhexidine (2%) and alcohol (70%). A 1 cm-wide incision was made at the level of right and left lower quadrant in the abdomen and sensor was inserted there. The incision was closed using a surgical monofilament suture. Male mice had the temperature sensor stitched to the abdominal muscle to prevent it from moving down to the scrotum. The procedure duration did not exceed 10 min.

3.3.3. Evaluation of mRNA through *in-situ* hybridization (RNAscope)

The multiplex *in situ* hybridization (RNAscope, Advanced Cell Diagnostics, Newark, California) was used for semi-quantitative evaluation of the *Kcnq2/Kcnq3* mRNA expression per glutamatergic neurons (*mCherry*-positive) after shRNA injection. The expression of the mRNA was evaluated at 2, 4 and 8 weeks after the virus injection, matching the time window for the ventilation experiments.

At the end of the virus incubation period, animals were deeply anesthetized with isoflurane, until toe or tail pinch reflexes were no longer evoked, then perfused through their right atrium with a phosphate-buffered saline solution (PBS) 0.1X, followed by 4% paraformaldehyde (PFA). Their brains were removed and kept in 4% PFA in the refrigerator overnight (~18 h). On the next day, brains were sectioned using a vibratome (7000smz-2, Campden Instruments, Loughborough,

Leicestershire, England), and 30 µm-thick fresh sections were saved in duplicates. The first section of each duplicate was used to check virus (*mCherry*) expression under the fluorescent microscope (Axioscope 5 Upright Microscope, ZEISS, Thornwood, New York) in the following morning. The second duplicates were saved in a well-plate with Tris-buffered saline solution with Tween 20 (TBST) 0.5X, for maximum of 48 hours in the refrigerator (4° C) and used for RNAscope.

After checking for the presence of *mCherry*-positive neurons, ~9 slices containing the preBötC from the second duplicate were selected and proceeded to a 2-day RNAscope protocol.

On the first day, sections were washed in TBST 0.5X, then mounted onto superfrost slides, and followed a pre-treatment protocol for fixation, dehydration and target recovering. On the second day, the RNAscope Multiplex Fluorescent Reagent Kit v2 Assay was used to label the mRNA molecules for the *Kcnq3* (channel 1 [C1]) and *Kcnq2* genes (channel 2 [C2]), and to identify *mCherry*-positive glutamatergic neurons (channel 3 [C3]). Labeling protocol was performed according to the instructions of the manufacturer. Fluorescent dyes Opal 520, Opal 690 and Opal 570 were added to label *Kcnq3*, *Kcnq2*, and *mCherry*, respectively, and DAPI solution was added for nuclei labeling. ProLong Gold Antifade Mountant (Invitrogen, ThermoFisher Scientific, Waltham, Massachusetts) was used to preserve the fluorescent signal, and a glass coverslip was placed over the samples. The slides were stored up to 2 weeks in the fridge for imaging.

Samples were visualized under the four-channel, upright confocal microscope (Cerna, ThorLabs, Newton, New Jersey), and images were acquired using the ThorImage LS Data Acquisition Software.

3.3.4. Ventilatory measurements

Ventilation (\dot{V}_E) was measured in *Vglut2-ires-cre* and wild-type adult mice using the flow-through whole-body plethysmography (Jacky, 1978; Mortola & Frappell, 1998; da Silva *et al.*, 2023), which enables continuous respiratory recordings of a freely behaving mouse. The mouse was placed in a 300 mL acrylic plethysmograph chamber (SCIREQ, Emka Technologies, Québec, Canada) where the airflow was controlled by a pressurized air breathing tank (21% O₂ and N₂ balance) connected to an inlet port, and by a mass flow controller at the outlet port. Inlet and outlet flow were maintained at $\pm 250 \text{ mL}\cdot\text{min}^{-1}$ and were periodically regulated using a flowmeter (Brooks Instrument, Hatfield, Pennsylvania) to maintain pressure within the chamber, which was also connected to a temperature sensor (Traceable Pocket-Size K, Fisherbrand). The opening through which the sensor wire passed was covered using a high vacuum grease, and an additional small leak was intentionally made at this passage. The leak worked as high-resistance bias flow filter (i.e., increased the time constant of the chamber) and helped controlling the flow [and the pressure] inside the chamber. Thus, flow was controlled in such a way that the time it takes for the chamber's pressure to stabilize (time constant) after a step change in pressure is

applied, is sufficiently longer than the mouse's breathing, which prevents pressure leakage from interfering with accurate measurement of respiratory variables (Hernandez *et al.*, 2012). The ambient temperature was measured by a general-purpose liquid-in-glass thermometer.

Here, respiration was indicated as barometric pressure oscillations proportional to changes in temperature and humidity in the air (Drorbaugh & Fenn, 1955). The inspired tidal volume was heated from the chamber's temperature to the body temperature and saturated with water vapor, and the exhaled tidal volume was again cooled to the chamber's temperature, and these alterations caused changes in the chamber pressure (Drorbaugh & Fenn, 1955; Mortola & Frappell, 1998).

Pressure oscillations in the plethysmography chamber were collected at a 1 kHz by a pressure differential transducer (Spirometer, ADInstruments, Colorado Springs, Colorado), connected to the 300 mL chamber, passing through an analog-to-digital data converter (PowerLab, ADInstruments), then digitized on a computer equipped with a data acquisition and analysis program (LabChart v.8, ADInstruments).

We measured respiratory frequency (f_R) quantified as the number of breaths per minute (breaths.min⁻¹), and tidal volume (V_T), calculated using the Drorbaugh & Fenn (1955) formula:

$$V_T = \frac{V_K \times \left(\frac{P_T}{P_K}\right) \times T_B \times (P_B - P_C)}{T_B \times (P_B - P_C) - T_C \times (P_B - P_b)} \quad (1)$$

Where V_K is the volume of air injected in the chamber for mV-to-volume calibration, P_T is the pressure deflection associated with each volume of air flowing, P_K is the pressure deflection associated with the injected volume for calibration, T_B is mouse's body temperature (in Kelvin), T_C is the temperature inside the chamber (in Kelvin), P_b is the water vapor pressure at T_B , P_B is the barometric pressure, and P_C is the vapor pressure of water vapor in the chamber, which was presumed to be fully saturated because the bottom of the chamber was filled with thin layer of water.

Ventilation was then calculated as the product of f_R and V_T and is presented with respect to body mass as a fraction of 100 grams. \dot{V}_E and V_T are presented at standard conditions of **B**ody **T**emperature, **P**ressure, water **S**aturated (BTSPS, (Hochscule *et al.*, 1973)). V_K was obtained by injecting 0.3 mL ($r^2=0.9$) ~20 times in 5 sets using a syringe connected to the chamber at a similar rate to the respiratory frequency of the animal. P_C and P_b were obtained using appropriate lookup tables (Dejours, 1981).

3.3.5. Oxygen consumption

Metabolism was determined using indirect calorimetry (oxygen consumption, ($\dot{V}O_2$)) by the pull-mode configuration, through the open respirometry system (Koteja, 1996; Cummings *et al.*, 2011).

A fraction of the oxygen inside of the chamber containing the subject was sampled by the gas analyzer (ADInstruments, Colorado Springs, Colorado)

connected in series, digitally acquired at 1 kHz (PowerLab, ADInstruments), while the flow was kept at $\pm 120 \text{ mL}\cdot\text{min}^{-1}$ via a suction pump from the analyzer, and measured by a flowmeter (PFMV530-1, SMCpneumatics, Yorba Linda, California). The sampled gas was dried through a 10-cm desiccant column (W.A. Hammond Drierite, Xenia, Ohio) connected between the chamber and the gas analyzer.

The oxygen consumption was calculated using the following formula (Depocas & Hart, 1957; Koteja, 1996):

$$\dot{V}O_2 = \frac{[Fl \times (F_iO_2 - F_eO_2)]}{(1 - F_iO_2) \times (1 - RQ)} \quad (2)$$

Where FI is the input flow rate, F_iO_2 is the fraction of O_2 inspired; F_eO_2 is the fraction of O_2 expired. The respiratory quotient (RQ) is the ratio of carbon dioxide released to oxygen consumed ($\dot{V}CO_2/\dot{V}O_2$) (assumed to be 0.85 (Raurich *et al.*, 1989)). The $\dot{V}O_2$ is presented with respect to body mass as a fraction of 100 grams, and in **Standard conditions of Temperature, Pressure, and Dry air** (STPD).

3.3.6. Experimental protocols

in situ hybridization and injection site imaging. shRNA knockdown was evaluated via RNAscope. Following transcatheter perfusion and brain removal procedures, the brainstem of the injected animals was trimmed off to the desired bregma

level. Landmarks such as the change in the shape of the area postrema and the fourth ventricle at the dorsal side, and the presence of the inferior olives and the nucleus ambiguus at the ventral side, were used to determine the bregma coordinate of that section, and the mouse brain atlas (Paxinos & Franklin, 2019) was used as a reference. Subsequently, 30 μm -thick slices were cut in duplicates, and sections immediately caudal, at, and rostral to the preBötC were saved. This allowed tracking the coordinates to later evaluate the accuracy of the injection site.

Slices were processed according to the labeling assay protocol as described previously, and then imaged. For mRNA quantification, images were taken using a 40X objective lens, with a 1X digital optical zoom, at a resolution of 1024 x 1024 pixels. *mCherry*-positive glutamatergic neurons were identified, and images were taken from 5 adjacent quadrants within the region circumscribed by the presence of those cells. Each image was captured at a single z-level, with microscope focus adjusted between quadrants. To ensure robust expression levels, we established a criterion whereby each quadrant contained a minimum of 20 distinct and identifiable neurons. At least 3 animals were imaged per time point, and ~9 slices per animal were imaged. Due to the presence of multiple targets of interest, 4 color channels with distinct excitation/emission parameters were used: Opal 520 (green) was excited with 488 nm (blue) wavelength, Opal 690 (far-red) with 642 nm (red), Opal 570 (red) with 561 nm (green), and DAPI (blue) was excited with 405 nm (UV) wavelength. Pictures were later pseudo-colored using the open-source software Fiji (v. 2.14.0) (Schindelin *et al.*, 2012).

Conversely, photomicroscopies used for evaluation of the injection site were acquired using a 10X objective lens, with a 1X digital optical zoom, at a resolution of 512 x 512 pixel. One slice at a time was positioned within a 3 x 6 array, and each grid was imaged. Individual tiles were then assembled in Fiji. Besides of the slices at the bregma level of the preBötC, caudal and rostral sections were also imaged to assess the dispersion of the virus to proximal nuclei. Only 561 nm and 405 nm wavelength were used.

evaluation of the normocapnic/normoxic ventilatory and metabolic responses to *Kcnq2/Kcnq3* knockdown. *Vglut2-ires-cre* mice had their ventilatory and metabolic responses recorded before (baseline) and after the shRNA-targeting and control injections. The person performing this protocol was blinded to the injection received by each group.

Mice were placed in an acrylic plethysmography chamber and were let 30 minutes for acclimation. Next, their respiratory parameters were recorded for an additional 30 minutes. Ventilation and metabolism were recorded continuously, whereas body temperature, room temperature and chamber temperature were verified every 5 minutes throughout the whole hour of recording. Barometric pressure was checked at the end of the day. Mice were returned to their cage at the end of the recording.

After 7 weeks of recordings, mice had their injection site verified as described previously.

evaluation of the ventilatory responses of C57BL/6J and Vglut2-ires-cre mice to fentanyl. The role of *KCNQ2/KCNQ3*-mediated M-currents on the opioid-induced respiratory depression (OIRD) was assessed by evaluating the ventilatory and metabolic responses of *Kcnq2/Kcnq3*-targeting and control Vglut2-ires-cre mice to fentanyl.

First, two different doses of fentanyl (200 µg/Kg and 400 µg/Kg) were administered to wild-type mice (C57BL/6J). Animals were placed in the plethysmograph chamber for an acclimation period of 30 minutes. Next, they were quickly removed from the chamber, fentanyl was injected, and they were recorded again for additional 60 minutes.

The second round of experiments consisted in administering 200 µg/Kg and 400 µg/Kg of fentanyl to *Kcnq2/Kcnq3*-targeting and control Vglut2-ires-cre mice after 3 weeks of virus incubation. Similarly, mice were placed in the plethysmograph chamber for an acclimation period of 30 minutes, then fentanyl was administered i.p., and they were recorded for another 60 minutes.

For all cases, ventilation and metabolism were recorded continuously, whereas body temperature, room temperature and chamber temperature were verified every 5 minutes throughout the whole recording. Barometric pressure was checked daily at the end of the protocol. Vglut2-ires-cre mice were sacrificed to confirm the injection site.

3.3.7. Data analysis

RNAscope and injection site. Images of *Kcnq2* and *Kcnq3* transcripts were analyzed using the using the open-source software Quantitative Pathology (QuPath, v. 0.4.4) (Bankhead *et al.*, 2017). *mCherry*-positive glutamatergic neurons were identified and used to delimitate the area to select the transcripts.

We defined as a criterion that each dot inside of a *mCherry*-positive neuron was considered as a single transcript. However, due to the limitation of the RNAscope in labeling single transcripts exclusively, some can appear in conglomerates, which were considered multi-transcript clusters in our analysis. Therefore, besides calculating the number of transcripts per neuron, we also evaluated the number of clusters per neuron, and the mean cluster area. Because neurons and clusters can occur in different sizes, calculated the ratio of the cluster area per neuron area, which allowed us to compare the relative density of the clusters and minimizing the impact of variations of the neuron size on the analysis. The detection threshold used to identify neurons, dots and clusters were kept the same throughout the analyzes and the groups.

We plotted the number of each parameter analyzed using Prism software (Prism, Graphpad Software, Boston, Massachusetts). Multiple slices (n) and mice (N) were photographed and analyzed. Nonparametric unpaired t-test, with Holm-Sidak multiple comparisons test, was used to evaluate the statistical difference between the *Kcnq2/Kcnq3*-knockdown and control group. We applied a significance threshold of $\alpha = 0.05$.

Moreover, we also evaluated the extension of the injection qualitatively. For that purpose, 10X photomicrographies were used. The sites of the microinjections were manually sketched on top of photographed slices and colored in magenta, and the margins of the tissues were also manually drawn and colored in black. We used at least 3 slices of the same bregma level, and individual sections were superimposed. The virus expression area with a darker magenta indicates that more *mCherry*-positive neurons were found at that same location in different animals.

Ventilation and metabolism. For protocol 1.2, we computed various respiratory parameters (dependent variables), including \dot{V}_E , V_T , f_R , inspiratory time (T_I), expiratory time (T_E), inspiratory drive (V_T/T_I), $\dot{V}O_2$, and ventilatory equivalent ($\dot{V}_E/\dot{V}O_2$). The absolute values of the respiratory variables of each animal, at each day of recording, were plotted on the y-axis against the days post-shRNA injection (independent variable) using Prism software (Prism, Graphpad Software, Boston, Massachusetts). We performed linear regression analysis to determine the best-fit slope (r^2) for each parameter, along with the corresponding 95% confidence intervals (CIs). F-test was used to evaluate the slope of the respiratory variables. If there's no relationship (i.e., slope equals zero), the F-statistic returns to a P-value that indicates the likelihood of the slope deviating from zero. Then, we also calculated whether the slopes of different lines (here representing each treatment group) were equal. We applied a significance

threshold of $\alpha = 0.05$, indicating that the slopes were different, thus there was a treatment effect.

Besides analyzing the ordinary respiratory parameters above, we also evaluated the respiratory variability using Poincaré plots (Tulppo *et al.*, 1996; Li & Nattie, 2006; Golińska, 2013). Therefore, the duration of each breath (T_{TOTn}) was plotted versus the duration of the next breath (T_{TOTn+1}). This returns to a plot of scattered dots from where we calculated the width of the variation perpendicular to (standard deviation 1, SD1) and along (standard deviation 2, SD2) the line of identity (Li & Nattie, 2006; Patrone *et al.*, 2018). SD1 measures the short-term variability, whereas SD2 measures the long-term variability, and they are descriptors commonly used in quantifying Poincaré plot geometry. They were calculated using the following formulas (Golińska, 2013):

$$SD1 = \frac{\sqrt{2}}{2} SD(x_n - x_{n+1}) \quad (3)$$

$$SD2 = \sqrt{2SD(x_n)^2 - \frac{1}{2}SD(x_n - x_{n+1})^2} \quad (4)$$

For protocol 1.3, we analyzed the f_R , T_I and T_E , which are common descriptors that indicate OIRD. Similarly, we also performed linear regression analysis to determine the best-fit slope (r^2) for each parameter and plotted the corresponding 95% confidence intervals (CIs). F-test was also used to evaluate the likelihood of

the slope deviating from zero. Finally, we also calculated whether the slopes of different lines (here representing each treatment group) were equal. We applied a significance threshold of $\alpha = 0.05$.

3.4. Results

3.4.1. *shRNA effectively knocks down Kcnq2/Kcnq3 in preBötC glutamatergic neurons*

We used adeno-associated virus serotype 9 (AAV9) to carry short-hairpin RNA (shRNA) designed to decrease the expression of *Kcnq2/Kcnq3* and drive *mCherry* expression in a *Cre*-dependent fashion. We injected either *Kcnq2/Kcnq3*-targeting shRNA or control shRNA with the same set of nucleotides but in a scrambled, non-targeting order, into the preBötC of Vglut2-ires-cre mice. *mCherry*-positive glutamatergic neurons were identified in the preBötC (Fig. 3.1a, bottom). To further identify whether viral infection spread to neighboring nuclei, we examined sections throughout the rostro-caudal extent of the ventral medulla (Supplementary Fig. S3.1). Although *mCherry*-positive neurons were visible dorsally, their strongest expression, which indicates the overlapping of injection sites for multiple mice, is concentrated ventrally at the levels -7.1 mm to -6.8 mm caudal to bregma, which encompasses the whole extent of the preBötC (Fig. 3.1a).

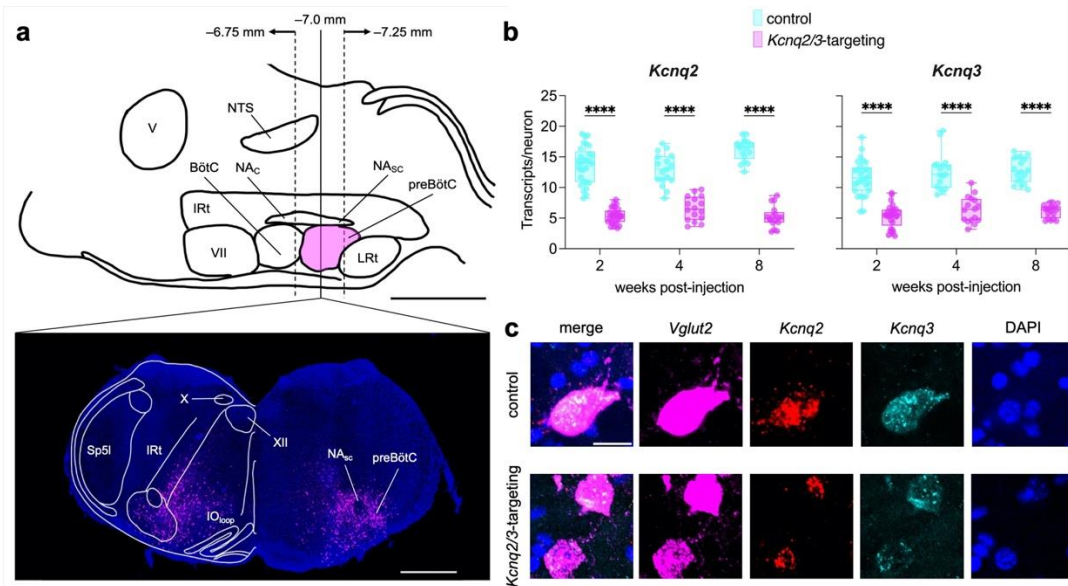


Fig. 3.1 – shRNA decreases *Kcnq2/Kcnq3* expression in glutamatergic preBötC neurons. **(a)** Parasagittal (lateral = -1.2 mm) view of mouse brainstem (top). At the bottom, a 10X photomicrograph shows the presence of *mCherry*-positive glutamatergic neurons at the ventral border of the brainstem in transverse section at -6.9 mm caudal to bregma, at the level of the preBötzingner Complex (preBötC). Known landmarks are shown: fifth (trigeminal) nucleus (V), seventh (facial) nucleus (VII), dorsal motor nucleus of the vagus (X), hypoglossal nucleus (XII), spinal trigeminal interpolaris nucleus (Sp5l), nucleus of the solitary tract (NTS), medullary intermediate reticular nucleus (IRt), nucleus ambiguous compact (NAc) and semi-compact (NA_{sc}) parts, Bötzingner Complex (BötC), and lateral reticular nucleus (LRt). In both figures, scale bars at the right bottom corner represent 1 mm. **(b)** Box plot quantifying *Kcnq2* (left) and *Kcnq3* (right) transcripts per glutamatergic neuron from control (cyan) and *Kcnq2/Kcnq3*-targeting (magenta) shRNA, at 2, 4 and 8 weeks post-injection (x-axis). Each filled circle represents the average transcript/neuron of one slice (“n”, 2 weeks: control, n = 29, *Kcnq2/3*-targeting: 17; 4 and 8 weeks: control, n = 17, *Kcnq2/3*-targeting, n = 17). **(c)** 40X photomicrographs showing *Kcnq2* (red) and *Kcnq3* (cyan) expression in glutamatergic neurons (magenta), and DAPI (blue) labels nuclei. Scale bar (20 μm) applies to all panels.

Next, we evaluated *Kcnq2* expression in glutamatergic neurons. We analyzed the number of individual transcripts per neuron (Fig. 3.1b, left) as well as multi-transcript clusters because of their high prevalence (Supplementary Figs. S3.1 and S3.2, Table 3.1).

Table 3.1 – *Kcnq2* expression decreases in glutamatergic preBötC neurons in *Kcnq2/Kcnq3*-knockdown mice. Quantification of *Kcnq2* transcripts in mice that received either non-targeting (control) or *Kcnq2/Kcnq3*-targeting (targeting) shRNA. Each row represents a different type of measurement. Each column represents the time points of transcript quantification and the experimental groups. Columns also report p-values for the disparity in expression levels between experimental groups (unpaired t-tests). Values are presented as mean \pm s.d.

	2 weeks			<i>Kcnq2</i> 4 weeks			8 weeks		
	control (n=29)	targeting (n=29)	<i>p</i>	control (n=17)	targeting (n=16)	<i>p</i>	control (n=17)	targeting (n=17)	<i>p</i>
Transcripts/neuron	13.7 \pm 2.9	5.4 \pm 1.3	1.0×10^{-14} *	12.9 \pm 2.6	6.6 \pm 1.9	4.9×10^{-8} *	16.2 \pm 1.8	5.2 \pm 1.7	1.0×10^{-14} *
Clusters/neuron	2.0 \pm 0.6	1.1 \pm 0.3	6.9×10^{-11} *	2.0 \pm 0.4	1.3 \pm 0.6	6.2×10^{-4} *	2.4 \pm 0.4	0.9 \pm 0.4	2.9×10^{-12} *
Cluster area (μm^2)	982.5 \pm 477.9	472.7 \pm 216.7	3.0×10^{-5} *	984.1 \pm 459.6	651.0 \pm 310.5	1.6×10^{-2} *	892.6 \pm 543.3	349.3 \pm 201.2	8.4×10^{-4} *
Cluster area/neuron area (%)	11.4 \pm 5.1	4.7 \pm 1.6	9.3×10^{-9} *	15.1 \pm 8.3	8.8 \pm 5.9	1.3×10^{-2} *	13.6 \pm 6.3	4.3 \pm 2.1	7.1×10^{-6} *

*Indicates statistically significant.

The *Kcnq2* transcripts (Table 3.1, and Fig. 3.1b, left) were knocked down by 60.7 % at 2 weeks ($p = 1 \times 10^{-14}$), 49.2 % at 4 weeks ($p = 4.9 \times 10^{-8}$), and 67.8 % at 8 weeks ($p = 1 \times 10^{-14}$) in the *Kcnq2/Kcnq3*-targeting group compared to their matched control group. Similarly, we also observed that the average number of clusters per neuron, the cluster area, and the ratio of cluster area with respect to neuron area for *Kcnq2* was lower at all time points for the cohort receiving *Kcnq2/Kcnq3*-targeting shRNA (Table 3.1, Supplementary Fig. S3.2).

Additionally, it can be observed qualitatively that *Kcnq2* transcripts are more prevalent in the control group and the transcript clusters are larger in representative neurons (Fig. 3.1c and Supplementary Fig. S3.1).

Because Kv7 channels are usually heterodimers consisting of *Kcnq2* and *Kcnq3* subunits, we also analyzed the effect of the shRNA knockdown on *Kcnq3* (Table 3.2, Fig. 3.1b, right).

Table 3.2 – *Kcnq3* expression decreases in glutamatergic preBötC neurons in *Kcnq2/Kcnq3*-knockdown mice. Quantification of *Kcnq3* transcripts in mice that received either non-targeting (control) or *Kcnq2/Kcnq3*-targeting (targeting) shRNA. Each row represents a different type of measurement. Each column represents the time points of transcript quantification and the experimental groups. Columns also report p-values for the disparity in expression levels between experimental groups (unpaired t-tests). Values are presented as mean \pm s.d.

	2 weeks			<i>Kcnq3</i> 4 weeks			8 weeks		
	control (n=29)	targeting (n=29)	<i>p</i>	control (n=17)	targeting (n=16)	<i>p</i>	control (n=17)	targeting (n=17)	<i>p</i>
Transcripts/neuron	11.6 \pm 2.8	5.3 \pm 1.9	$4.3 \times 10^{-13*}$	12.6 \pm 2.9	6.4 \pm 2.1	$9.8 \times 10^{-7*}$	12.8 \pm 2.0	6.2 \pm 1.0	$4.2 \times 10^{-14*}$
Clusters/neuron	0.5 \pm 0.3	0.3 \pm 0.2	$3.3 \times 10^{-3*}$	1.0 \pm 0.4	0.5 \pm 0.3	$2.1 \times 10^{-3*}$	0.8 \pm 0.2	0.5 \pm 0.2	$4.8 \times 10^{-4*}$
Cluster area (μm^2)	132.7 \pm 105.7	121.8 \pm 76.3	0.7	193.8 \pm 166.0	116.0 \pm 96.7	0.1	129.7 \pm 63.9	118.7 \pm 65.0	0.6
Cluster area/neuron area (%)	1.3 \pm 1.1	1.0 \pm 0.5	0.2	2.5 \pm 1.6	1.6 \pm 1.2	0.07	2.1 \pm 1.1	1.5 \pm 0.7	0.04*

*Indicates statistically significant.

Similarly, *Kcnq3* transcripts were reduced by 54.1% at 2 weeks ($p = 4.3 \times 10^{-13}$), 49.3 % at 4 weeks ($p = 9.8 \times 10^{-7}$), and 51.9 % at 8 weeks ($p = 4.2 \times 10^{-14}$) in the cohort receiving *Kcnq2/Kcnq3*-targeting shRNA compared to the matched control group. Additionally, the number of clusters per neuron was also reduced at all time points (Table 3.2, Supplementary Fig. S3.2). Likewise, a greater abundance of *Kcnq3* transcripts in the control relative to the *Kcnq2/Kcnq3*-targeting shRNA group can be observed qualitatively in representative neurons in Fig. 3.1c (and Supplementary Fig. S3.1).

3.4.2. *Kcnq2/Kcnq3* knockdown does not impact breathing of *Vglut2-ires-cre* mice

Having confirmed that shRNA-carrying viruses infect the preBötC and substantially diminish *Kcnq2/Kcnq3* expression in glutamatergic neurons, we

evaluated the role of M-currents in breathing by measuring the tidal volume (V_T), respiratory frequency (f_R), and ventilation (\dot{V}_E) of control and *Kcnq2/Kcnq3*-knockdown mice breathing in normocapnic and normoxic air, every 7 days, for 7 weeks (Fig. 3.2). Representative traces of whole-body plethysmography recordings are shown (Fig. 3.2a, b) and linear regression was used to determine whether these breathing measures changed during the time course of the experiment (Fig. 3.2c-e, Table 3.3). Daily values are reported in Supplementary Table S3.1.

In summary, we observed no effects whatsoever. Initially, we predicted that if M-currents contributed to burst termination *in vitro*, then its attenuation via *Kcnq2/Kcnq3* knockdown would decrease f_R of the targeting group *in vivo*.

Table 3.3 – Linear regression analysis shows no change in breathing measurements in *Kcnq2/3*-knockdown (*Kcnq2/3*-KD) mice. Linear regression parameters include: r^2 , coefficient of determination; slope (m) in units per day of observation, i.e., unit.d⁻¹; and the probability (p) of obtaining a slope of the reported value if there is no relationship between the independent variable (time point following virus injection) and tidal volume (V_T), respiratory frequency (f_R), and ventilation (\dot{V}_E).

	control (N=8)			<i>Kcnq2/3</i> -KD (N=9)			probability of slope disparity? (p)
	m	r^2	p	m	r^2	p	
V_T (mL.100g ⁻¹)	-5.9 x 10 ⁻⁴	0.002	0.7	-0.002	0.03	0.1	0.5
f_R (breaths.min ⁻¹)	0.05	9.6 x 10 ⁻⁴	0.8	0.2	0.007	0.5	0.7
\dot{V}_E (mL.min ⁻¹ .100g ⁻¹)	-0.05	2.1 x 10 ⁻⁴	0.9	-0.1	8.1 x 10 ⁻⁴	0.8	0.9

*Indicates statistically significant.

Surprisingly, our data revealed that diminution of *Kcnq2/Kcnq3* expression in preBötC glutamatergic neurons did not modify breathing. Indeed, the respiratory

variables of *Kcnq2/Kcnq3*-knockdown mice remained unchanged throughout the observation period (Fig. 3.2c-e), i.e., the slopes of the regression lines did not differ from zero (Table 3.3).

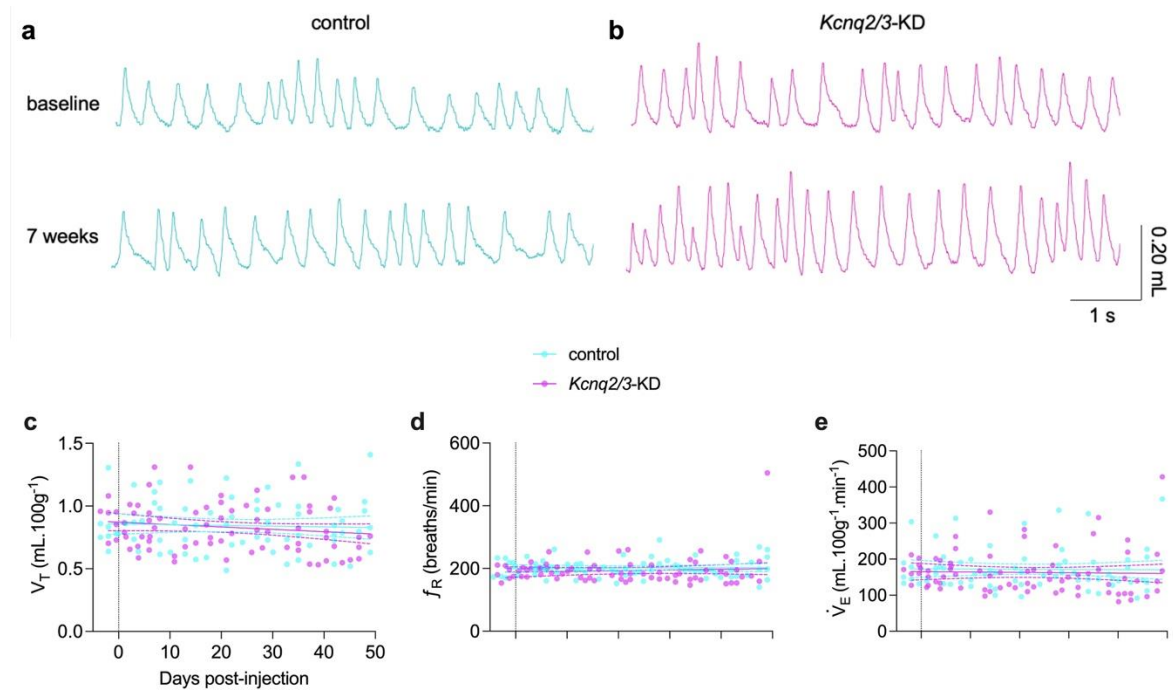


Fig. 3.2 – *Kcnq2/Kcnq3* knockdown does not affect breathing. Representative traces of whole-body plethysmography recordings from (a) control and (b) *Kcnq2/Kcnq3*-knockdown (*Kcnq2/3-KD*) mice at baseline (top) and 7 weeks (bottom) post-injection. Dot-scatter plots of (c) tidal volume (V_T), (d) respiratory frequency (f_R), and (e) ventilation (\dot{V}_E) of control (cyan, $N = 8$) and *Kcnq2/3-KD* (magenta, $N = 9$) groups. Vertical dashed lines indicate the day when *Vglut2-ires-cre* mice were injected with virus. Left to the vertical dashed lines are the baseline respiratory variables, values to the right of day 0 were measured every 7 days, for 7 weeks. Individual symbols represent one mouse. Horizontal lines represent the best-fitted slope (r^2), and horizontal dashed lines show the 95% confidence intervals (CIs).

We further hypothesized that attenuating the M-currents would affect termination the inspiratory phase of one breathing cycle, therefore affecting the inspiratory-expiratory phase transition. Thus, we analyzed the inspiratory time (T_I), expiratory time (T_E), and metabolism via indirect calorimetry (oxygen

consumption, $\dot{V}O_2$). We also calculated their ventilatory equivalent ($\dot{V}_E/\dot{V}O_2$). We evaluated whether these measures changed during the observation period using linear regression (Table 3.4, Fig. 3.3).

Table 3.4 – Inspiratory and expiratory duration, as well as metabolism, do not change in *Kcnq2/Kcnq3*-knockdown (*Kcnq2/3*-KD) mice. Linear regression parameters include: r^2 , coefficient of determination; slope (m) in units per day of observation, i.e., unit.d⁻¹; and the probability of obtaining a slope of the reported value if there is no relationship between the independent variable (time point following virus injection) and inspiratory time (T_I), expiratory time (T_E), oxygen consumption ($\dot{V}O_2$), and ventilatory equivalent ($\dot{V}_E/\dot{V}O_2$).

	control (N=8)			<i>Kcnq2/3</i> -KD (N=9)			probability of slope disparity? (p)
	m	r^2	p	m	r^2	p	
T _I (s)	-2.9 x 10 ⁻⁴	0.02	0.2	1.9 x 10 ⁻⁴	0.01	0.4	0.1
T _E (s)	3.4 x 10 ⁻⁴	0.02	0.2	6.8 x 10 ⁻⁵	0.001	0.8	0.5
$\dot{V}O_2$ (mL.min ⁻¹ .100g ⁻¹)	0.006	0.02	0.24	0.003	0.006	0.5	0.8
$\dot{V}_E/\dot{V}O_2$	-0.2	0.03	0.2	-0.2	0.04	0.06	0.9

*Indicates statistically significant.

Our analyses revealed that none of the measures showed a regression line with a slope that differed from zero, and there were no differences between the groups (Fig. 3.3, Table 3.4, and Supplementary Table S3.2).

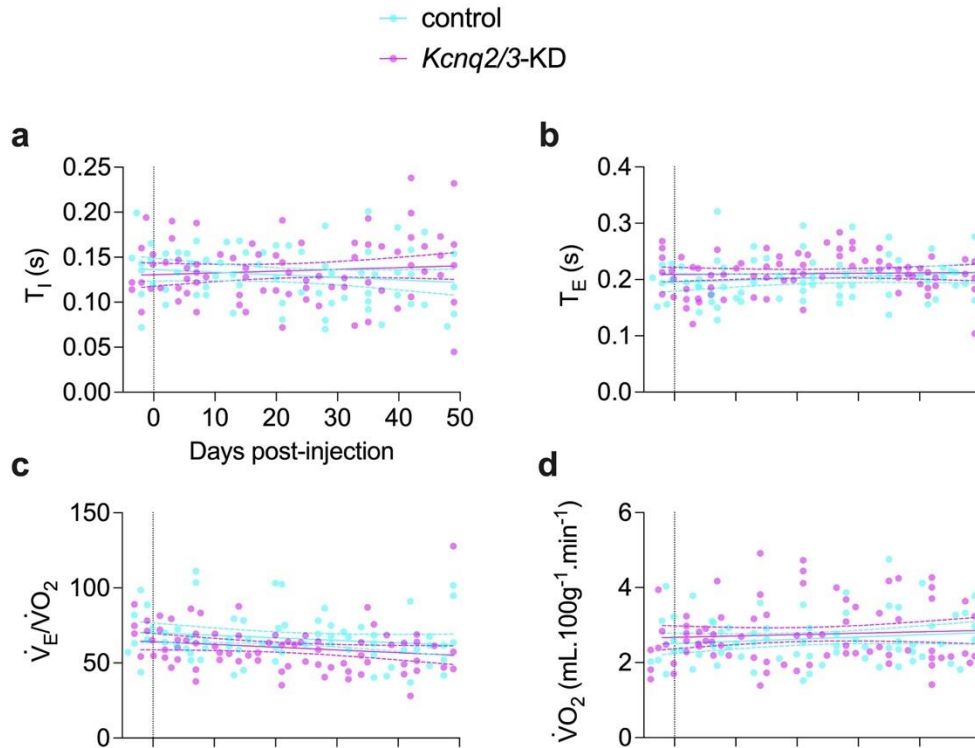


Fig. 3.3 – Breathing phase and metabolism of Vglut2-ires-cre mice do not change after *Kcnq2/Kcnq3* knockdown. (a) Inspiratory time (T_I), (b) expiratory time (T_E), (c) ventilatory equivalent ($\dot{V}_E/\dot{V}O_2$), and (d) oxygen consumption ($\dot{V}O_2$) of control (cyan, $N = 8$) and *Kcnq2/Kcnq3*-knockdown (*Kcnq2/3*-KD, $N = 9$) (magenta) groups. Vertical dashed lines indicate the day when Vglut2-ires-cre mice were injected with virus. Left to the vertical dashed lines are the baseline respiratory variables, values to the right of day 0 were measured every 7 days, for 7 weeks. Individual symbols represent one mouse. Horizontal lines represent the best-fitted slope (r^2), and horizontal dashed lines show the 95% confidence intervals (CIs).

3.4.3. *Kcnq2/Kcnq3* knockdown in the glutamatergic preBötC neurons

does not change the respiratory drive or breathing variability

Because no increments in T_I were observed following *Kcnq2/Kcnq3* knockdown, challenging our initial prediction, we sought to examine related aspects of breathing like the rate of air movement into the lungs during the inspiratory

phase, i.e., respiratory drive (V_T/T_I), which could also be affected by M-currents to the extent that these currents are recruited during inspiration.

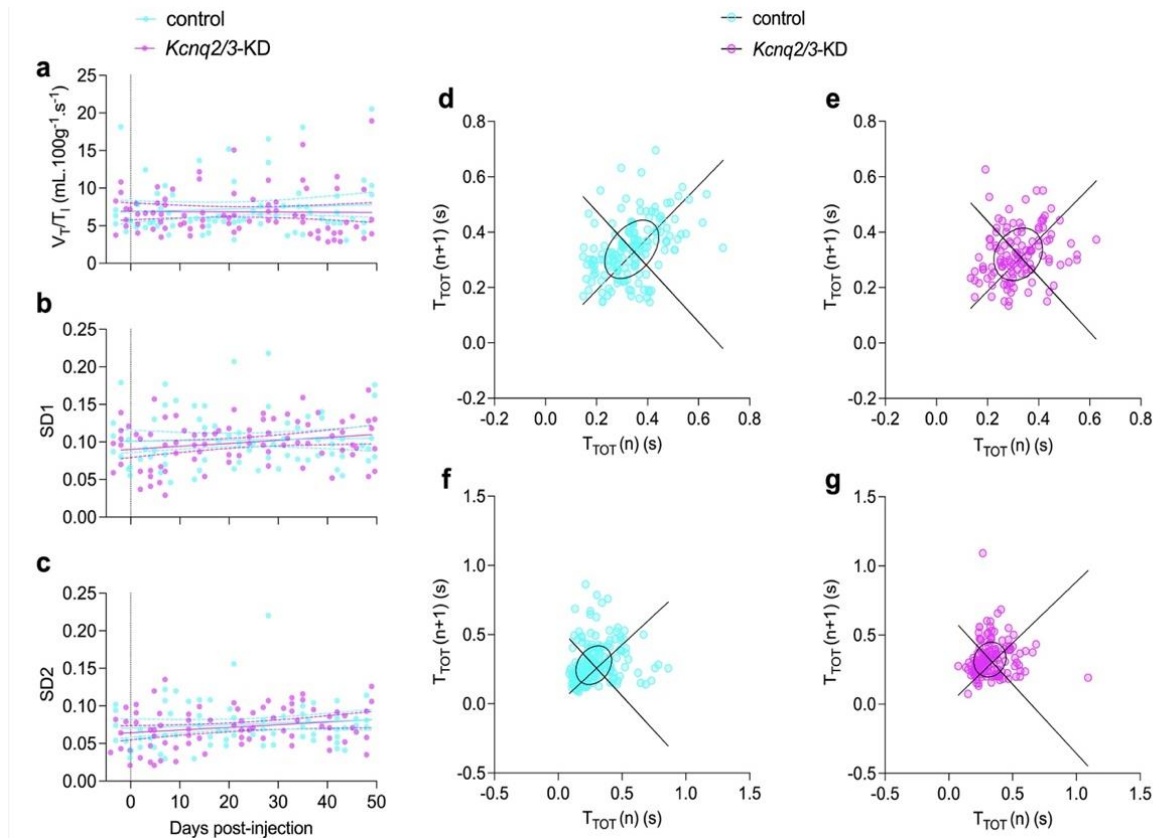


Fig. 3.4 – *Kcnq2/Kcnq3* diminution does not affect respiratory drive and breathing variability. (a) Respiratory drive (V_T/T_I), (b) short-term variability (standard deviation 1, SD1), and (c) long-term variability (standard deviation 2, SD2) of control (cyan, $N = 8$) and *Kcnq2/Kcnq3*-knockdown (*Kcnq2/Kcnq3*-KD) (magenta, $N = 9$) mice. Vertical dashed lines indicate the day when *Vglut2-ires-cre* mice were injected with virus. Left to the vertical dashed lines are the baseline respiratory variables, values to the right of day 0 were measured every 7 days, for 7 weeks. Individual symbols represent one mouse. Horizontal lines represent the best-fitted slope (r^2), and horizontal dashed lines show the 95% confidence intervals (CIs). (d-g) Poincaré plots of cycle time duration (T_{TOT}) of two consecutive breathing events (i.e., x-axis: $T_{TOT}(n)$ versus y-axis: $T_{TOT}(n+1)$) of control (cyan) and *Kcnq2/Kcnq3*-KD (magenta) mice before (d and e) and post-injection (f and g). Ellipse was fitted to the plot along with the perpendicular line to the line of identity (SD1) and the parallel line to the line of identity (SD2).

We performed linear regression to evaluate whether the respiratory drive changed during the observation period, however neither control nor *Kcnq2/Kcnq3*-knockdown mice exhibited slopes that deviated from zero, and

the groups did not differ from one another (Fig. 3.4a, Table 3.5, Supplementary Table S3.3).

Table 3.5 – Respiratory drive as well as short- and long-term variability changes in *Kcnq2/Kcnq3*-knockdown (*Kcnq2/Kcnq3*-KD) mice. Linear regression parameters include: r^2 , coefficient of determination; slopes (m) in units per day of observation, i.e., $\text{unit}\cdot\text{d}^{-1}$; and the probability of obtaining a slope of the reported value if there is no relationship between the independent variable (time point following virus injection) and respiratory drive (V_T/T_I), standard deviation 1 (SD1) and standard deviation 2 (SD2).

	control (N=8)			<i>Kcnq2/3</i> -KD (N=9)			probability of slope disparity? (p)
	m	r^2	p	m	r^2	p	
V_T/T_I ($\text{mL}\cdot 100\text{g}^{-1}\cdot\text{s}^{-1}$)	0.02	0.008	0.5	-0.003	2.6×10^{-4}	0.9	0.5
SD1 (s)	7.9×10^{-5}	0.001	0.8	3.9×10^{-4}	0.05	0.04*	0.3
SD2 (s)	2.3×10^{-4}	0.02	0.3	3.5×10^{-4}	0.05	0.04*	0.6

*Indicates statistically significant.

We further evaluated whether M-currents contribute to cycle-to-cycle phase transitions using Poincaré plots (a.k.a., joint interval-return maps) to analyze the breath-to-breath variability of breathing cycle time (T_{TOT}). A Poincaré plot maps the current cycle time ($T_{TOT}[n]$) on the x-axis versus the next cycle time ($T_{TOT}[n+1]$). The geometric structure of the map gives insight into cycle-to-cycle dynamics. Variability is demonstrated by the relative dispersion of the points in the map.

There was no recognizable shape to the Poincaré plots (Fig. 3.4d-g), such as rings or distinct clustering of dots, which would indicate multi-periodic or quasi-periodic behavior (Del Negro *et al.*, 2002c), so we considered the Poincaré plots to reflect single periodic behaviors. We further used two descriptors to quantify the dispersion of points contained in the cluster shown in the Poincaré plots, thus

representing variability via the width (short-term variability, SD1), and the length (long-term variability, SD2) of an ellipse fitted to the point cluster (Tulppo *et al.*, 1996; Golińska, 2013).: standard deviation 1 (SD1), and standard deviation 2 (SD2).

By fitting an ellipse to the Poincaré plots (Fig. 3.4-g) at each day of observation, we could track the breath-to-breath variability during the experiment by changes in SD1 and SD2. We then plotted a time series of SD1 (Fig. 3.4b) and SD2 (Fig. 3.4c) and analyzed them by linear regression. The positive slope (m) of SD1 and SD2 of *Kcnq2/Kcnq3*-knockdown mice deviated from zero and exceeded the threshold for statistical significance (i.e., $\alpha < 0.05$). While the conventional interpretation would be that short- and long-term breathing variability change during the study, we do not attribute any physiological importance to this otherwise statistically significant p-value because the slope for control and *Kcnq2/Kcnq3*-knockdown groups are not statistically different from one another and the effect size is small. Thus, the most parsimonious conclusion is that *KCNQ2/KCNQ3*-mediated M-currents in glutamatergic preBötC neurons do not influence breathing phase transitions in such a way that their attenuation affects breath-to-breath variability (Fig. 3.4b-g).

3.4.4. Opioid-induced respiratory depression is not prevented in *Kcnq2/Kcnq3*-knockdown mice

M-current putatively contributes to OIRD. Therefore, we evaluated whether the *Kcnq2/Kcnq3* knockdown could revert the depressant effects of fentanyl, which is a μ -opioid receptor agonist, by removing the postsynaptic target for opioid modulation of cellular excitability in the preBötC.

We first used C57BL/6J (wild-type) mice to evaluate the OIRD at two fentanyl doses (200 μ g/Kg and 400 μ g/Kg) injected intraperitoneally (i.p.). This approach was necessary to ascertain whether these doses would depress breathing but not being fatal, because we ultimately needed *Vglut2-ires-cre* mice to survive until the end of the experiment to verify the viral infection in the preBötC after receiving either control or *Kcnq2/Kcnq3*-targeting shRNA.

Linear regression was used to determine whether breathing changed following fentanyl injection in wild-type mice (Fig. 3.5, Table 3.6).

Table 3.6 – High dose of fentanyl causes OIRD in wild-type mice. Linear regression parameters include: r^2 , coefficient of determination; slopes (m) in units per minute, i.e., $\text{unit}\cdot\text{min}^{-1}$; and the probability (p) of obtaining a slope of the reported value if there is no relationship between the independent variable (time point following fentanyl injection) and respiratory frequency (f_R), inspiratory time (T_I), expiratory time (T_E).

	wild-type – 200 μ g/Kg (N=4)			wild-type – 400 μ g/Kg (N=4)			probability of slope disparity? (p)
	m	r^2	p	m	r^2	p	
f_R (breaths. min^{-1})	-5.5	0.03	0.5	-22.1	0.6	3.0×10^{-4} *	0.08
T_I (s)	0.01	0.4	0.008*	0.01	0.5	0.003*	0.7
T_E (s)	0.003	0.04	0.4	0.01	0.4	0.01*	0.1

*Indicates statistically significant.

Mice injected with 200 $\mu\text{g}/\text{Kg}$ of fentanyl did not decrease f_R (Fig. 3.5a and c); linear regression analysis did not return a slope statistically different from zero ($p = 0.5$). Mice receiving a dose of 400 $\mu\text{g}/\text{Kg}$ (Fig. 3.5b and c) decreased f_R ($p = 3.0 \times 10^{-4}$). At both doses, T_I increased following fentanyl throughout the 10 min period of observation (Fig. 3.5d); the slope of the regression line significantly deviated from zero (200 $\mu\text{g}/\text{Kg}$: $p = 0.008$; 400 $\mu\text{g}/\text{Kg}$: $p = 0.003$). Lastly, T_E did not increase in response to 200 $\mu\text{g}/\text{Kg}$ fentanyl, whereas T_E in mice injected with 400 $\mu\text{g}/\text{Kg}$ fentanyl presented a small increment, and the slope of the regression line significantly deviated from zero ($p = 0.01$).

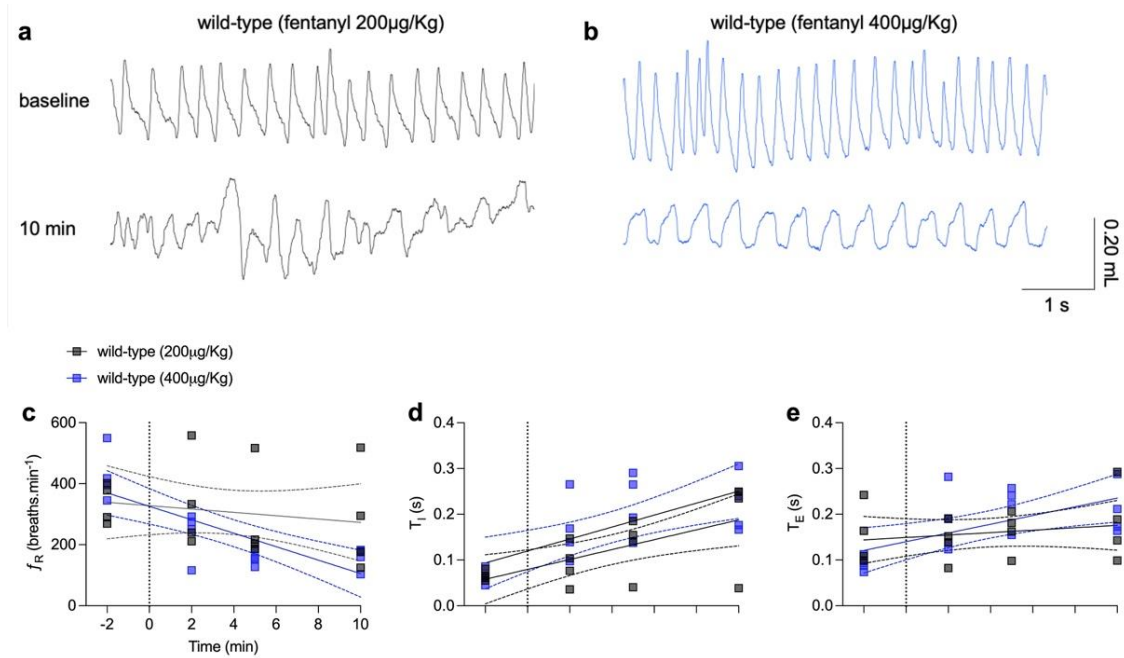


Fig. 3.5 – Fentanyl causes respiratory depression. Representative traces of whole-body plethysmography recordings from C57BL/6J (wild-type) mice injected with **(a)** 200 µg/Kg (N = 4) and **(b)** 400 µg/Kg (N = 4) dose of fentanyl (i.p.). Linear regression plots of **(c)** frequency (f_R), **(d)** inspiratory time (T_I), and **(e)** expiratory time (T_E). Vertical dashed lines indicate the moment of fentanyl injection. Values left to the vertical dashed lines were measured at baseline, values to the right were measured at 2, 5 and 10 minutes after fentanyl administration. Individual symbols represent one mouse. Horizontal lines represent the best-fitted slope (r^2), and dashed lines show the 95% confidence intervals (CIs).

Because all doses exerted some depressant effect in breathing, with the higher dose affecting all the variables more profoundly, we evaluated the same respiratory variables of *Vglut2-ires-cre* mice injected with either control or *Kcnq2/Kcnq3*-targeting shRNA, at both doses of fentanyl (Fig. 3.6). Similarly, we used linear regression to determine whether breathing variables changed during the time course of the experiment (Table 3.7).

Table 3.7 – Inspiratory time in control and *Kcnq2/Kcnq3*-knockdown (*Kcnq2/Kcnq3*-KD) mice increase in response to fentanyl. Linear regression parameters include: r^2 , coefficient of determination; slopes (m) in units per minute, i.e., $\text{unit}\cdot\text{min}^{-1}$; and the probability (p) of obtaining a slope of the reported value if there is no relationship between the independent variable (time point following fentanyl injection) and breathing measurement (f_R , T_I , T_E). The columns are organized according to experimental group and fentanyl dose.

	200 $\mu\text{g}/\text{Kg}$						400 $\mu\text{g}/\text{Kg}$							
	control (N=5)			<i>Kcnq2/3</i> -KD (N=5)			p	control (N=5)			<i>Kcnq2/3</i> -KD (N=3)			p
	m	r^2	p	m	r^2	p		m	r^2	p	m	r^2	p	
f_R (breaths. min^{-1})	1.2	0.004	0.8	-1.0	0.003	0.8	0.7	-6.1	0.1	0.1	-10.8	0.4	0.03*	0.4
T_I (s)	-7.8×10^{-4}	0.01	0.7	0.001	0.03	0.5	0.5	0.009	0.4	0.004*	0.01	0.6	0.004*	0.3
T_E (s)	0.001	0.02	0.5	-0.003	0.08	0.2	0.2	5.8×10^{-4}	0.004	0.8	-3.5×10^{-4}	0.003	0.9	0.8

*Indicates statistically significant.

Control and *Kcnq2/Kcnq3*-knockdown mice that received 200 $\mu\text{g}/\text{Kg}$ of fentanyl did not present any changes in f_R , T_I and T_E (Fig. 3.6, Table 3.7). This was surprising because we expected T_I to increase, as it did in wild-type administered the same dose of fentanyl. At a dose of 400 $\mu\text{g}/\text{Kg}$ fentanyl, only the *Kcnq2/Kcnq3*-knockdown mice presented a statistically significant decrease in f_R as determined by the slope of the regression line ($p = 0.03$). The control group showed a negative slope too ($m = -6.1$), which suggests a progressive diminution in f_R , but that fitted slope did not cross the threshold for statistical significance, by which criterion we fail to reject the null hypothesis. Finally, the T_I of both groups increased (control: $p = 0.004$; *Kcnq2/Kcnq3*-knockdown: $p = 0.004$), but the slope of both lines is not different ($p = 0.3$), which suggests that attenuation of M-current in the experimental group had no particular influence on opioid modulation of inspiratory duration. T_E remained unchanged in both cohorts following 400 $\mu\text{g}/\text{Kg}$ fentanyl.

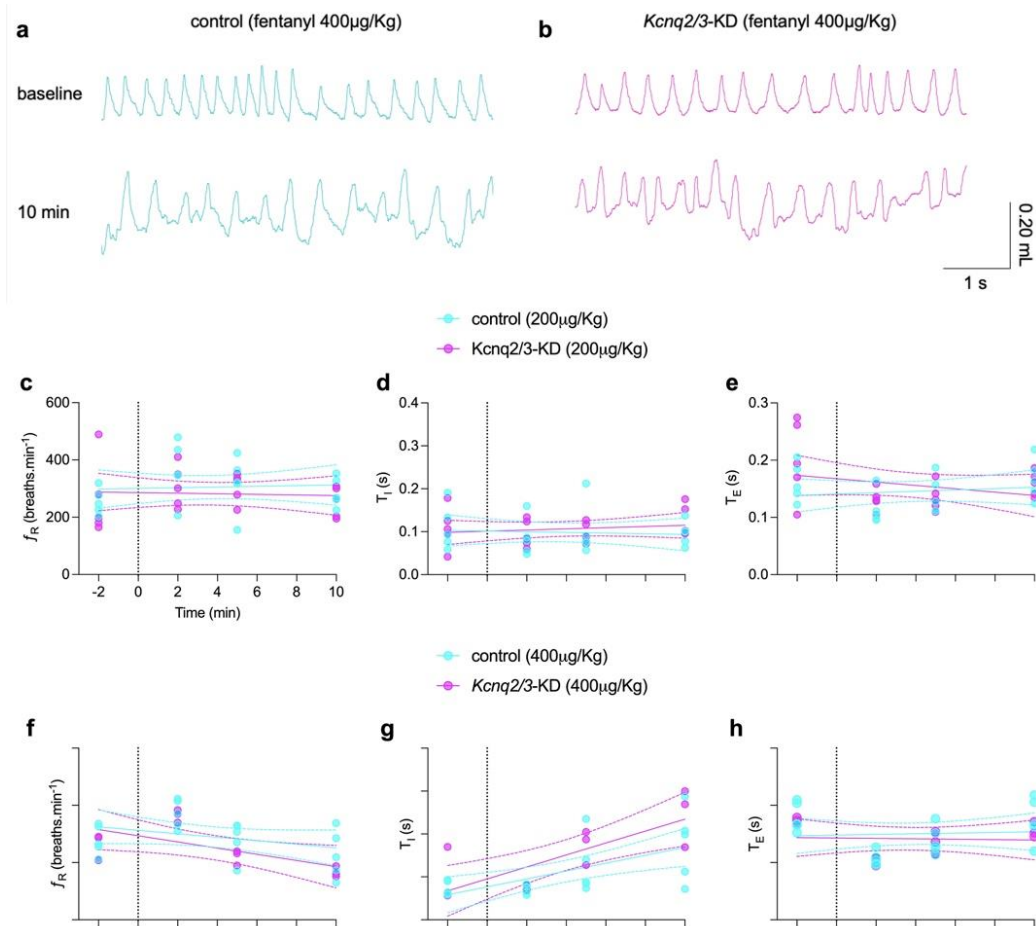


Fig. 3.6 – Vglut2-ires-cre mice only show OIRD at a higher dose of fentanyl. Representative traces of whole-body plethysmography recordings from (a) control and (b) *Kcnq2/Kcnq3*-knockdown (*Kcnq2/Kcnq3*-KD) mice receiving a dose of 400 µg/Kg of fentanyl. Linear regression plots of (c, f) frequency (f_R), (g, e) inspiratory time (T_i), and (e, h) expiratory time (T_E) of control (cyan) and *Kcnq2/Kcnq3*-KD (magenta) mice injected with 200 µg/Kg (top panels, control: N = 5; *Kcnq2/3*-KD: N = 5) and 400 µg/Kg (bottom panels, control: N = 5; *Kcnq2/3*-KD: N = 3) dose of fentanyl (i.p.). Vertical dashed lines indicate the moment of fentanyl injection. Values left to the vertical dashed lines were measured at baseline, and values to the right were measured at 2, 5 and 10 minutes after fentanyl administration. Individual symbols represent one mouse. Horizontal lines represent the best-fitted slope (r^2), and dashed lines show the 95% confidence intervals (CIs).

3.5. Discussion

Inspiratory bursts depend on recurrent synaptic excitation which evokes inward currents in the preBötC interneurons that sustain the burst (Del Negro *et al.*, 2018; Ramirez & Baertsch, 2018*b*, 2018*a*; Ashhad *et al.*, 2022). Then, the

inspiratory burst is followed by a transient refractory period originally characterized *in vitro* (Guerrier *et al.*, 2015; Kottick & Del Negro, 2015), which is also recognized *in vivo* after termination of inspiration (Baertsch *et al.*, 2018). KCNQ-mediated M-currents are hypothesized to contribute to these events due to their unique biophysical properties. Their role was recently explored using agonist (retigabine and ICA 69673) and antagonist (XE991 and linopirdine) drugs in rhythmically active transverse slices from neonatal mice that retain the preBötC (Wei & Ramirez, 2019; Revill *et al.*, 2021) and in freely behaving adult mice (Wei & Ramirez, 2019).

However, retigabine acts on a tryptophan residue in the transmembrane segment 5 segment present in KCNQ2-5 channels (Schenzer *et al.*, 2005), which can reduce excitability throughout the entire slice when applied in the bath medium, masking the role of M-currents in the preBötC specifically. Besides, this drug is known for its metabolic instability and effects on M-currents in peripheral tissues (Tykocki *et al.*, 2019; Groseclose & Castellino, 2019), which can influence the phenotype observed after its administration *in vivo*. Regarding XE991 and linopirdine, they are not efficacious on cells at resting membrane potentials (Greene *et al.*, 2017), and their inhibitory action *in vitro* and *in vivo* depends on previous channel activation. Thus, a partial block of KCNQ could have occurred in the aforementioned studies, which would underestimate the contributions of this current.

Therefore, we sought to address the issues inherent in pharmacological approaches and inhibit M-currents by using conditional knockdown of KCNQ

subunits via genetic technology, i.e., shRNA, expressed in a Cre-specific manner in core rhythmogenic glutamatergic neurons. That approach allows us to interrogate the contributions of specific KCNQ subunits in burst termination, while avoiding off-target effects on other types of preBötC neurons, as well as neurons elsewhere in the brain and central nervous system.

Kcnq1-Kcnq5 encode five members of the voltage-dependent potassium channel family, namely the Kv7, also known as M-currents for their classic activation by muscarinic acetylcholine receptor agonists (Brown & Adams, 1980). Although all subunits are expressed in the central nervous system, heteromeric channels composed of KCNQ2 and KCNQ3 subunits are expressed predominantly in most neurons (Brown & Passmore, 2009; Springer *et al.*, 2021).

Previous studies using next-generation single-cell mRNA sequencing showed that both KCNQ2 and KCNQ3 subunits are highly expressed in Dbx1 neurons in the preBötC, whereas KCNQ4, KCNQ5 and KCNQ1 are much less prevalent (Hayes *et al.*, 2017). Besides, KCNQ1 is generally expressed in the heart and KCNQ4 is mostly restricted to areas involved in the central auditory pathway. KCNQ3 and KCNQ5 can form heteromeric channels, but the role and expression pattern of KCNQ5 are underestimated and have not been elucidated (Kharkovets *et al.*, 2000; Robbins, 2001; Wang & Li, 2016; Springer *et al.*, 2021). Therefore, KCNQ2 and KCNQ3 are better candidates because the contemporary consensus is that they mediate the classical M-currents (Springer *et al.*, 2021), and our RNAscope data revealed that those two characteristic subunits are expressed and that shRNA conditional knockdown partially precludes their expression.

KCNQ channels present slow kinetics (tens to hundreds of milliseconds) at subthreshold membrane potentials, and do not inactivate (Brown & Adams, 1980; Brown & Passmore, 2009). Their activation during inspiratory bursts counteracts the inward currents that sustain bursts, including persistent sodium current (I_{NaP}) and calcium-activated non-specific mixed cation current (I_{CAN}) (Del Negro *et al.*, 2002*b*, 2002*a*, 2005; Pace *et al.*, 2007; Ramirez & Baertsch, 2018*a*; Yamanishi *et al.*, 2018; Picardo *et al.*, 2019; da Silva *et al.*, 2023). Therefore M-currents have the appropriate voltage-dependence and kinetics to contribute to inspiratory burst termination.

If KCNQ-mediated M-currents are important to dampen the ongoing depolarization promoted by inward currents, then one predicts that (1) inhibition of these channels, either by antagonists or conditional knockdown, would increase burst duration by removing activity dependent outward current, and (2) augmentation of KCNQ channels pharmacologically would decrease burst duration, by enhancing the outward current and terminating the inspiratory cycle more quickly. However, distinct groups have tested the role of M-currents in burst termination and results are inconsistent. Further, our present findings do not recapitulate either set of discrepant results.

Application of XE991 or linopirdine (KCNQ channel blockers) increased inspiratory burst duration and decreased burst frequency *in vitro* (Revill *et al.*, 2021), as expected. Note, the decrease in burst frequency was attributed to longer overall cycle time as a consequence of longer burst duration. However, our present findings are different because we did not observe a change in the

inspiratory time during normal breathing in unanesthetized adult mice with genetically inhibited *Kcnq2* and *Kcnq3* expression. Rather, all breathing measures of *Kcnq2/Kcnq3*-knockdown mice remain unchanged, which resonates with findings by Wei & Ramirez (2019) who showed that XE991 and Chromanol 293B, another KCNQ channel blocker, did not affect baseline inspiratory burst frequency of rhythmic preBötC slices (Wei & Ramirez, 2019). Those authors, however, did not evaluate whether XE991 and Chromanol 293B affected inspiratory burst duration via intracellular recordings *in vitro* or inspiratory time *in vivo* (they only examined frequency).

Interestingly, both studies reported that retigabine, a KCNQ channel activator, decreased burst frequency in rhythmically active slice preparations (Wei & Ramirez, 2019; Revill *et al.*, 2021) and breathing frequency in neonate and adult mice *in vivo* (Wei & Ramirez, 2019). These results are at first counterintuitive according to our initial prediction because one would expect that activation of these currents would speed up the rhythm by shortening the inspiratory time. However, there is a simple explanation that both sets of authors (Wei & Ramirez, 2019; Revill *et al.*, 2021) agree on: activator drugs like retigabine and ICA 69673 enhance the M-current in part by shifting its activation range (such that channel recruitment occurs at lower membrane potentials) and enhancing the M-current active at baseline, (Vervaeke *et al.*, 2006; Peretz *et al.*, 2007; Springer *et al.*, 2021), which hyperpolarizes the constituent neurons and thus impacts frequency by hyperpolarizing neurons in the preBötC, as well as neurons that provide tonic drive to the preBötC, such as the raphe neurons (Ptak *et al.*, 2009), or

hyperpolarizing other network elements such as XII pre- and motoneurons (Revill *et al.*, 2021).

Although we did not measure breathing under pharmacological conditions that enhance KCNQ channel activation, nothing in our present results contradict or call into question the results mentioned above and their interpretation.

Furthermore, the attenuation of frequency in rhythmic slices *in vitro* by retigabine and ICA 69673 reported by Wei & Ramirez (2019) could also be attributed to the activation of KCNQ channel subunits in the presynaptic terminals, which would lower presynaptic release probability by hyperpolarizing the terminals. That putative KCNQ-mediated presynaptic inhibition would operate in conjunction with KCNQ-mediated hyperpolarization of the baseline membrane potential, where the pre- and postsynaptic effects would operate in cumulatively, in tandem, to lower preBötC, and thus breathing, frequency.

The discrepancy in the phenotypes reported by Revill *et al.* (2021) and Wei & Ramirez (2019) compared to the present study may be attributable due to differences in experimental perturbations.

First, it is possible that reduction, rather than complete elimination, of the *Kcnq2/Kcnq3* expression in the present study might not recapitulate the phenotype observed in the previous studies, and thus cause one to underestimate the role of the targeted genes and their cognate ion channel proteins (Fellmann & Lowe, 2014). Indeed, one caveat in our approach is that the levels of *Kcnq2* and *Kcnq3* transcript knockdown achieved by shRNA expression

is on the order of ~50%, which may not be sufficient to impede the role of M-current in breathing phase transition *in vivo*. That is, one must knockdown *Kcnq2/Kcnq3* much more than 50% to cause a phenotype, which was not possible in the present study because of the limitations of reverse genetic technologies.

The preserved respiratory network in our model might also activate compensatory pathways, i.e., perhaps *Kcnq1/Kcnq4/Kcnq5* levels increase (not evaluated here), in response to *Kcnq2/Kcnq3* knockdown, whereas rhythmic slice preparations allow one to study the biophysical contributions of KCNQ-mediated M-currents on burst termination via drugs that act acutely without time for gene regulation and indeed indiscriminately target all subunits that can contribute to M-currents.

The recruitment of the inspiratory-induced vagally mediated inhibitory feedback to the preBötC (Janczewski *et al.*, 2013), electrogenic outward currents as well as I_{K-ATP} and I_{K-Na} (Del Negro *et al.*, 2009; Krey *et al.*, 2010) and synaptic depression (Guerrier *et al.*, 2015; Kottick & Del Negro, 2015), cannot be excluded in our freely behaving mice, and can still terminate inspiration and indeed may be enhanced following *Kcnq2/Kcnq3* knockdown.

KCNQ channels are also proposed as putative mediators of OIRD (Wei & Ramirez, 2019), independent of the classical intracellular signaling mediated by μ -opioid receptor 1 (MOR1) and the G protein-coupled inwardly rectifying potassium (GIRK) channel (consult Gray *et al.*, 1999; Montandon *et al.*, 2011,

2016b, 2016a for review). The mechanism by which KCNQ modulates the depressant effects of opioids is hypothesized to occur as follows: $G\beta/\gamma$ bind to the α_1 subunit of P/Q-type and N-type calcium channels after MOR1 activation by opioids; this intracellular event shifts the voltage-dependence activation of calcium channels towards depolarized potentials; hyperpolarization of presynaptic terminals due to M-currents further precludes calcium channel activity and breathing is impaired (Zamponi & Currie, 2013; Wei & Ramirez, 2019).

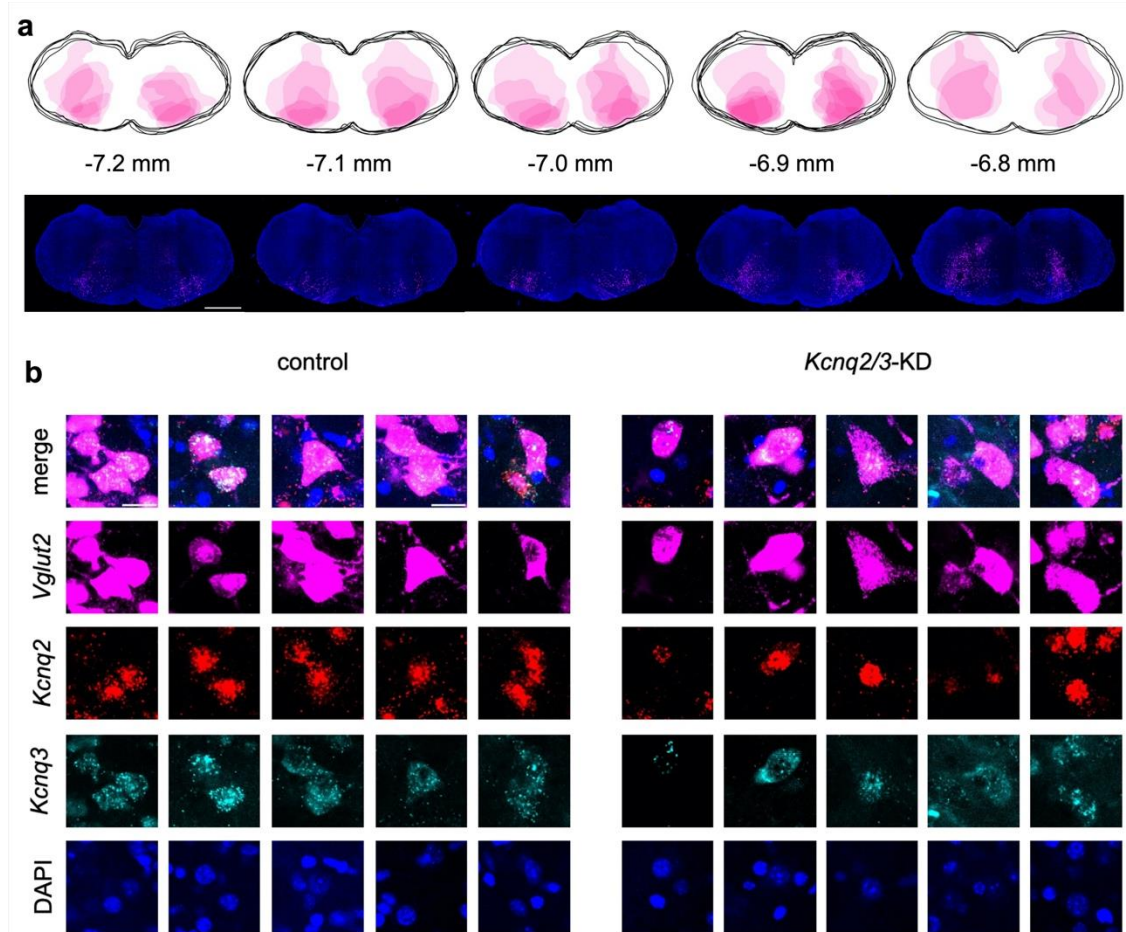
Intraperitoneal application of XE991 in neonate and adult mice reversed the OIRD, supporting the previous hypothesis. Nonetheless, this effect was state-dependent because XE991 only recovered respiratory rate when morphine doses were strong enough to reduce breathing below 2.9 Hz in neonates and below 2.0 Hz in adults. We found no OIRD modulation whatsoever in *Kcnq2/kcnq3*-knockdown mice at the doses of fentanyl we tested. This might be attributable to our fentanyl doses that did not depress breathing rhythm to the point where M-currents would be relevant given the state-dependent effects characterized by Wei & Ramirez (2019). Rather, the doses administered in this study were chosen to specifically depress breathing but not kill the mice. We had to take a conservative approach with fentanyl because mouse survival was absolutely needed to verify viral expression in the preBötC. Nonetheless, we found no evidence for KCNQ-mediated M-currents in OIRD.

Another factor that could explain why our *Kcnq2/Kcnq3*-knockdown mice showed no OIRD could be due to the ~50% knockdown levels we achieved, and in that context perhaps the residual M-current is sufficient to evoke mild OIRD, which we observed after knockdown. Perhaps, the effect of M-currents in OIRD would only be noticed when stronger doses of opioids severely slow breathing down and the M-current is reduced to levels less than 50%.

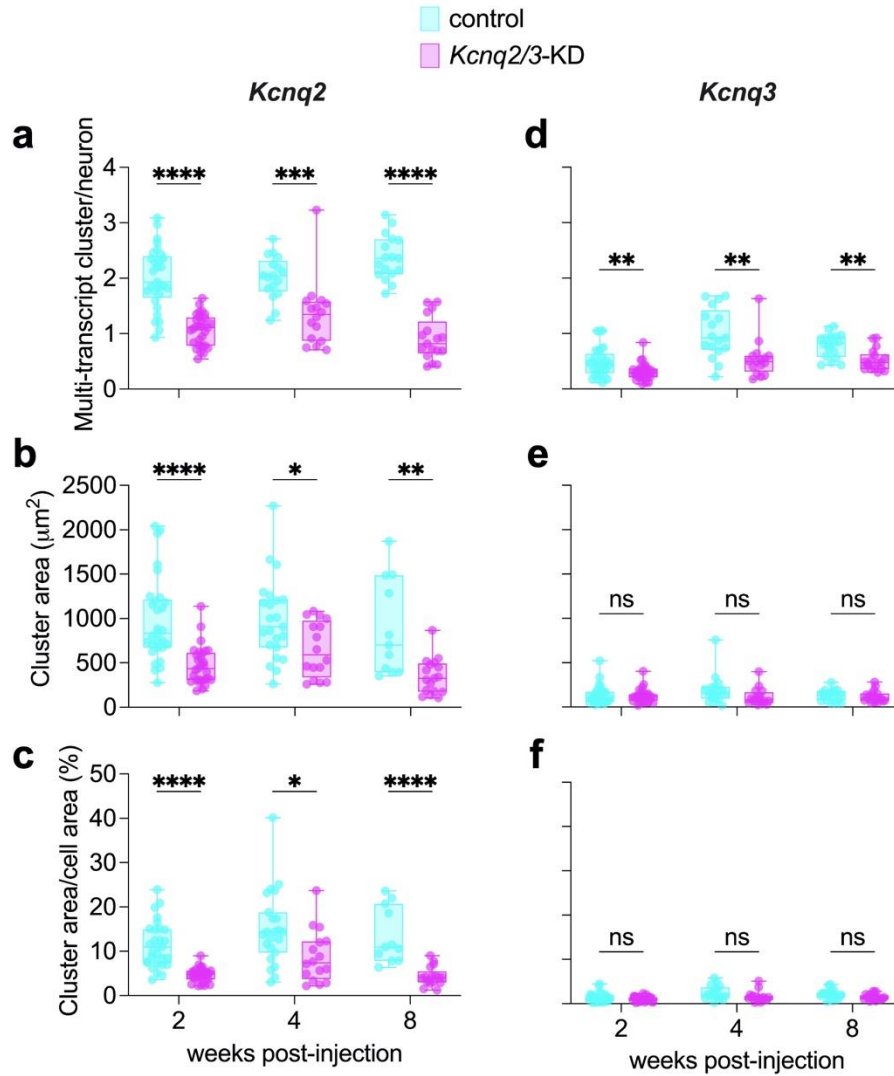
We also attribute the lack of OIRD recover in *Kcnq2/kcnq3*-knockdown mice to action of opioids elsewhere in the brain, such as the parabrachial (PBN)/Kolliker-Fuse (KF) nuclear complex of the midbrain, which our experiments did not perturb but has been demonstrated to provide excitatory drive to breathing and is hyperpolarized by opioid activation of inwardly rectifying K⁺ channels, which induces respiratory disturbances (Lalley *et al.*, 2014; Levitt *et al.*, 2015; Bachmutsky *et al.*, 2020; Liu *et al.*, 2021).

Therefore, even though our results do not support the putative role of KCNQ channels as mediators of termination of inspiration and OIRD *in vivo*, we cannot rule out a limited contribution of M-type potassium currents in mediating these events in conjunction with other synaptic and cellular-ionic mechanisms not evaluated here.

3.6. Supplementary Information



Supplementary Fig. S3.1 – (a) Schematic representation of the injection site of the adeno-associated virus serotype 9 (AAV9) carrying either a non-targeting or *Kcnq2/Kcnq3*-targeting short-hairpin RNA (shRNA) sequences. Top, coronal diagrams showing the distribution of the viral injection at five different Bregma coordinates. Black solid lines outline the brainstem borders, and the magenta shaded area represents the area covered by *mCherry*-positive glutamatergic neurons. Five slices (*n*) at -7.2 mm, *n* = 5 at -7.1 mm, *n* = 5 at -7.0 mm, *n* = 7 at -6.9 mm and *n* = 3 at -6.8 mm were superimposed. Bottom, 10X photomicrographs of brainstem coronal sections showing the injection across five different levels of the ventral respiratory column with respect to Bregma. Scale bar at the right bottom corner represents 1 mm. **(b)** 40X photomicrographs of the RNAscope for transcripts of the vesicular glutamate transporter 2 (*Vglut2*, magenta, second row), *Kcnq2* (red, third row), *Kcnq3* (cyan, fourth row), and nuclear staining with DAPI (blue, fifth row). First row displays images merged. RNAscope was performed in control (left) and *Kcnq2/Kcnq3*-knockdown (*Kcnq2/3*-KD, right) mice. Scale bar (20 μ m) apply to all images.



Supplementary Fig. S3.2 – Box plots with average, minimum, and maximum values for each variable associated with the expression pattern of the *Kcnq2* (a-c) and *Kcnq3* (d-f) after 2 (29 slices), 4 (17 slices) and 8 (17 slices) weeks post-injection of a non-targeting (control, cyan) and a *Kcnq2/Kcnq3*-targeting (*Kcnq2/3*-KD, magenta) short-harping RNA (shRNA) in the preBötC. Each symbol represents one slice (“n”). *Indicates statistically significant; “ns” indicates non-significant.

Supplementary Table S1 – Daily absolute values for tidal volume (V_T), respiratory frequency (f_R), and ventilation (\dot{V}_E) of *Vglut2-ires-cre* mice injected with AAVs carrying non-targeting (control) or *Kcnq2/Kcnq3*-targeting (*Kcnq2/3*-KD) short-hairpin RNA (shRNA) sequences. Measurements were performed every 7 days, for 7 weeks after the injections. Values are expressed as mean \pm s.d.

		V_T (mL.100g ⁻¹)		f_R (breaths.min ⁻¹)		\dot{V}_E (mL.min ⁻¹ .100g ⁻¹)	
		control (N=8)	<i>Kcnq2/3</i> - KD (N=9)	control (N=8)	<i>Kcnq2/3</i> - KD (N=9)	control (N=8)	<i>Kcnq2/3</i> - KD (N=9)
Baseline		0.85 \pm 0.19	0.88 \pm 0.12	199.85 \pm 28.52	183.56 \pm 18.76	171.26 \pm 57.48	162.28 \pm 33.68
				203.66			
Post-injection days	7	0.87 \pm 0.24	0.89 \pm 0.24	191.99 \pm 28.98	197.55 \pm 25.04	176.87 \pm 62.15	175.29 \pm 49.55
	14	0.80 \pm 0.22	0.83 \pm 0.23	191.59 \pm 19.81	191.06 \pm 29.19	153.37 \pm 42.02	162.77 \pm 71.88
	21	0.86 \pm 0.23	0.83 \pm 0.17	191.59 \pm 25.75	195.50 \pm 38.65	166.63 \pm 62.43	166.53 \pm 63.63
	28	0.89 \pm 0.18	0.86 \pm 0.17	218.42 \pm 37.66	177.64 \pm 16.57	196.41 \pm 61.54	154.57 \pm 41.60
	35	0.82 \pm 0.26	0.87 \pm 0.25	197.34 \pm 21.48	191.94 \pm 35.93	164.99 \pm 70.53	170.07 \pm 74.55
	42	0.76 \pm 0.16	0.72 \pm 0.19	193.31 \pm 27.49	184.41 \pm 30.59	144.67 \pm 31.61	137.58 \pm 60.44
	49	0.88 \pm 0.26	0.78 \pm 0.15	210.68 \pm 44.77	219.79 \pm 110.52	189.07 \pm 83.59	175.82 \pm 105.36

Supplementary Table S3.2 – Daily absolute values for inspiratory time (T_I), expiratory time (T_E), oxygen consumption ($\dot{V}O_2$) and ventilatory equivalent ($\dot{V}_E/\dot{V}O_2$) of *Vglut2-ires-cre* mice injected with AAVs carrying non-targeting (control) or *Kcnq2/Kcnq3*-targeting (*Kcnq2/3-KD*) short-hairpin RNA (shRNA) sequences. Measurements were performed every 7 days, for 7 weeks after the injections. Values are expressed as mean \pm s.d.

	T_I (s)		T_E (s)		$\dot{V}O_2$ (mL.min ⁻¹ .100g ⁻¹)		$\dot{V}_E/\dot{V}O_2$		
	control (N=8)	<i>Kcnq2/3-KD</i> (N=9)	control (N=8)	<i>Kcnq2/3-KD</i> (N=9)	control (N=8)	<i>Kcnq2/3-KD</i> (N=9)	control (N=8)	<i>Kcnq2/3-KD</i> (N=9)	
Baseline	0.14 \pm 0.04	0.13 \pm 0.03	0.20 \pm 0.03	0.23 \pm 0.03	2.48 \pm 0.75	2.34 \pm 0.73	70.84 \pm 17.79	71.73 \pm 11.41	
Post-injection days	7	0.13 \pm 0.02	0.13 \pm 0.03	0.20 \pm 0.06	0.20 \pm 0.03	2.54 \pm 0.38	2.77 \pm 0.62	70.50 \pm 23.30	64.53 \pm 15.65
		0.14 \pm 0.03	0.13 \pm 0.03	0.20 \pm 0.04	0.21 \pm 0.03	2.56 \pm 0.57	2.79 \pm 1.12	62.07 \pm 13.62	59.53 \pm 11.72
	21	0.13 \pm 0.03	0.13 \pm 0.04	0.21 \pm 0.04	0.21 \pm 0.03	2.32 \pm 0.67	3.02 \pm 1.13	73.15 \pm 19.93	56.80 \pm 11.42
		0.12 \pm 0.04	0.12 \pm 0.01	0.20 \pm 0.04	0.25 \pm 0.02	2.73 \pm 0.59	2.92 \pm 0.73	71.56 \pm 8.07	53.58 \pm 9.37
	35	0.12 \pm 0.04	0.14 \pm 0.04	0.21 \pm 0.04	0.22 \pm 0.02	2.85 \pm 0.99	2.90 \pm 0.86	58.52 \pm 12.38	58.50 \pm 16.39
		0.14 \pm 0.03	0.16 \pm 0.04	0.20 \pm 0.03	0.20 \pm 0.02	2.57 \pm 0.70	2.67 \pm 1.03	58.83 \pm 16.28	52.71 \pm 13.10
	49	0.12 \pm 0.04	0.14 \pm 0.05	0.21 \pm 0.01	0.20 \pm 0.04	2.95 \pm 0.77	2.68 \pm 0.70	64.85 \pm 22.26	63.08 \pm 25.47

Supplementary Table S3.3 – Daily absolute values for respiratory drive (V_T/T_I), standard deviation 1 (SD1), and standard deviation 2 (SD2) of *Vglut2*-ires-cre mice injected with AAVs carrying non-targeting (control) or *Kcnq2/Kcnq3*-targeting (*Kcnq2/3*-KD) short-hairpin RNA (shRNA) sequences. Measurements were performed every 7 days, for 7 weeks after the injections. Values are expressed as mean \pm s.d.

	V_T/T_I (mL.100g ⁻¹ .s ⁻¹)		SD1 (s)		SD2 (s)		
	control (N=8)	<i>Kcnq2/3</i> - KD (N=9)	control (N=8)	<i>Kcnq2/3</i> - KD (N=9)	control (N=8)	<i>Kcnq2/3</i> - KD (N=9)	
Baseline	7.06 \pm 4.58	7.34 \pm 2.21	0.11 \pm 0.03	0.10 \pm 0.02	0.07 \pm 0.02	0.08 \pm 0.02	
Post-injection days	7	6.82 \pm 2.43	7.13 \pm 2.33	0.11 \pm 0.05	0.09 \pm 0.04	0.08 \pm 0.04	0.07 \pm 0.04
	14	6.18 \pm 3.14	6.75 \pm 2.96	0.11 \pm 0.04	0.10 \pm 0.02	0.08 \pm 0.03	0.07 \pm 0.02
	21	7.25 \pm 3.87	6.99 \pm 3.37	0.11 \pm 0.04	0.10 \pm 0.02	0.08 \pm 0.03	0.07 \pm 0.02
	28	8.76 \pm 4.00	7.58 \pm 1.76	0.11 \pm 0.05	0.11 \pm 0.02	0.08 \pm 0.06	0.08 \pm 0.02
	35	7.61 \pm 4.71	7.38 \pm 4.11	0.10 \pm 0.02	0.12 \pm 0.03	0.08 \pm 0.02	0.09 \pm 0.02
	42	5.86 \pm 1.65	5.40 \pm 3.17	0.09 \pm 0.03	0.10 \pm 0.03	0.07 \pm 0.02	0.07 \pm 0.02
	49	8.81 \pm 5.45	7.16 \pm 5.06	0.11 \pm 0.04	0.10 \pm 0.04	0.09 \pm 0.02	0.08 \pm 0.03

3.7. References

Ashhad S, Kam K, Del Negro CA & Feldman JL (2022). Breathing Rhythm and Pattern and Their Influence on Emotion. *Annu Rev Neurosci* **45**, 223.

Bachmutsky I, Wei XP, Kish E & Yackle K (2020). Opioids depress breathing through two small brainstem sites. *Elife*; DOI: 10.7554/ELIFE.52694.

Baertsch NA, Baertsch HC & Ramirez JM (2018). The interdependence of excitation and inhibition for the control of dynamic breathing rhythms. *Nat Commun* **9**, 1–17.

Bankhead P, Loughrey MB, Fernández JA, Dombrowski Y, McArt DG, Dunne PD, McQuaid S, Gray RT, Murray LJ, Coleman HG, James JA, Salto-Tellez M & Hamilton PW (2017). QuPath: Open source software for digital pathology image analysis. *Sci Rep*; DOI: 10.1038/s41598-017-17204-5.

Bouvier J, Thoby-Brisson M, Renier N, Dubreuil V, Ericson J, Champagnat J, Pierani A, Chédotal A & Fortin G (2010). Hindbrain interneurons and axon guidance signaling critical for breathing. *Nat Neurosci* **13**, 1066–1074.

Brown DA & Adams PR (1980). Muscarinic suppression of a novel voltage-sensitive K⁺ current in a vertebrate neurone. *Nature* **283**, 673–676.

Brown DA & Passmore GM (2009). Neural KCNQ (Kv7) channels. *Br J Pharmacol* **156**, 1185.

Burns BD (1963). The central control of respiratory movements. *Br Med Bull* **19**, 7–9.

Cregg JM, Chu KA, Dick TE, Landmesser LT & Silver J (2017). Phasic inhibition as a mechanism for generation of rapid respiratory rhythms. *Proc Natl Acad Sci U S A* **114**, 12815–12820.

Cummings KJ, Hewitt JC, Li A, Daubenspeck JA & Nattie EE (2011). Postnatal loss of brainstem serotonin neurones compromises the ability of neonatal rats to survive episodic severe hypoxia. *J Physiol* **589**, 5247–5256.

Dalby-Brown W, Hansen H, Korsgaard M, Mirza N & Olesen S-P (2006). K(v)7 channels: function, pharmacology and channel modulators. *Curr Top Med Chem* **6**, 999–1023.

Dejours Pierre (1981). *Principles of comparative respiratory physiology*. Elsevier/North-Holland Biomedical Press ; Sole distributors for the U.S.A. and Canada, Elsevier North-Holland, Amsterdam; New York; New York.

- Delcomyn F (1980). Neural Basis of Rhythmic Behavior in Animals. *Science* (1979) **210**, 492–498.
- DEPOCAS F & HART JS (1957). Use of the Pauling oxygen analyzer for measurement of oxygen consumption of animals in open-circuit systems and in a short-lag, closed-circuit apparatus. *J Appl Physiol* **10**, 388–392.
- Drorbaugh JE & Fenn WO (1955). A barometric method for measuring ventilation in newborn infants. *Pediatrics* **16**, 81–87.
- Feldman JL, Del Negro CA & Gray PA (2013). Understanding the rhythm of breathing: so near yet so far. *Annu Rev Physiol* **75**, 423.
- Fellmann C & Lowe SW (2014). Stable RNA interference rules for silencing. *Nat Cell Biol* **16**, 10.
- Fortuna MG, Kügler S & Hülsmann S (2019). Probing the function of glycinergic neurons in the mouse respiratory network using optogenetics. *Respir Physiol Neurobiol* **265**, 141–152.
- Funk GD, Smith JC & Feldman JL (1993). *Generation and Transmission of Respiratory Oscillations in Medullary Slices: Role of Excitatory Amino Acids*.
- Geiger J, Weber YG, Landwehrmeyer B, Sommer C & Lerche H (2006). Immunohistochemical analysis of KCNQ3 potassium channels in mouse brain. *Neurosci Lett* **400**, 101–104.
- Golińska AK (2013). Poincaré plots in analysis of selected biomedical signals. *Studies in Logic, Grammar and Rhetoric* **35**, 117–127.
- Gray PA, Hayes JA, Ling GY, Llona I, Tupal S, Picardo MCD, Ross SE, Hirata T, Corbin JG, Eugenin J & Del Negro CA (2010). Developmental Origin of PreBotzinger Complex Respiratory Neurons. *Journal of Neuroscience* **30**, 14883–14895.
- Gray PA, Rekling JC, Bocchiaro CM & Feldman JL (1999). Modulation of Respiratory Frequency by Peptidergic Input to Rhythmogenic Neurons in the PreBöttinger Complex. *Science* **286**, 1566.
- Greene DL, Kang S & Hoshi N (2017). XE991 and linopirdine are state-dependent inhibitors for Kv7/KCNQ channels that favor activated single subunits. *Journal of Pharmacology and Experimental Therapeutics* **362**, 177–185.
- Grillner S & El Manira A (2020). Current principles of motor control, with special reference to vertebrate locomotion. *Physiol Rev* **100**, 271–320.

- Groseclose MR & Castellino S (2019). An Investigation into Retigabine (Ezogabine) Associated Dyspigmentation in Rat Eyes by MALDI Imaging Mass Spectrometry. *Chem Res Toxicol* **32**, 294–303.
- Guerrier C, Hayes JA, Fortin G & Holcman D (2015). Robust network oscillations during mammalian respiratory rhythm generation driven by synaptic dynamics. *Proc Natl Acad Sci U S A* **112**, 9728–9733.
- Hayes JA, Kottick A, Picardo MCD, Halleran AD, Smith RD, Smith GD, Saha MS & Del Negro CA (2017). Transcriptome of neonatal preBötzinger complex neurones in Dbx1 reporter mice. *Scientific Reports* 2017 7:1 **7**, 1–13.
- Hernandez AB, Kirkness JP, Smith PL, Schneider H, Polotsky M, Richardson RA, Hernandez WC & Schwartz AR (2012). Novel whole body plethysmography system for the continuous characterization of sleep and breathing in a mouse. *J Appl Physiol* **112**, 671.
- Hochsule M, Institut P, Labora PD, Physiologic D, National C, Recherche D & Mead J (1973). Glossary on respiration and gas exchange. *J Appl Physiol* **34**, 549–558.
- Hülsmann S, Hagos L, Eulenburg V & Hirrlinger J (2021). Inspiratory Off-Switch Mediated by Optogenetic Activation of Inhibitory Neurons in the preBötzinger Complex In Vivo. *Int J Mol Sci* **22**, 1–11.
- Jacky JP (1978). A plethysmograph for long-term measurements of ventilation in unrestrained animals. *J Appl Physiol Respir Environ Exerc Physiol* **45**, 644–647.
- Janczewski WA, Tashima A, Hsu P, Cui Y & Feldman JL (2013). Role of Inhibition in Respiratory Pattern Generation. *The Journal of Neuroscience* **33**, 5454.
- Kharkovets T, Hardelin JP, Safieddine S, Schweizer M, El-Amraoui A, Petit C & Jentsch TJ (2000). From the Cover: KCNQ4, a K⁺ channel mutated in a form of dominant deafness, is expressed in the inner ear and the central auditory pathway. *Proc Natl Acad Sci U S A* **97**, 4333.
- Koizumi H & Smith JC (2008). Persistent Na⁺ and K⁺-Dominated Leak Currents Contribute to Respiratory Rhythm Generation in the Pre-Bötzinger Complex In Vitro. *The Journal of Neuroscience* **28**, 1773.
- Koteja P (1996). Measuring Energy Metabolism with Open-Flow Respirometric Systems: Which Design to Choose? *Funct Ecol* **10**, 675.
- Kottick A & Del Negro CA (2015). Synaptic Depression Influences Inspiratory–Expiratory Phase Transition in Dbx1 Interneurons of the preBötzinger Complex in Neonatal Mice. *Journal of Neuroscience* **35**, 11606–11611.

- Krey RA, Goodreau AM, Arnold TB & del Negro CA (2010). Outward Currents Contributing to Inspiratory Burst Termination in preBötzing Complex Neurons of Neonatal Mice Studied in Vitro. *Front Neural Circuits*; DOI: 10.3389/FNCIR.2010.00124.
- Lalley PM, Pilowsky PM, Forster H V. & Zuperku EJ (2014). CrossTalk opposing view: The pre-Bötzing complex is not essential for respiratory depression following systemic administration of opioid analgesics. *J Physiol* **592**, 1163.
- Levitt ES, Abdala AP, Paton JFR, Bissonnette JM & Williams JT (2015). μ opioid receptor activation hyperpolarizes respiratory-controlling Kölliker–Fuse neurons and suppresses post-inspiratory drive. *J Physiol* **593**, 4453.
- Li A & Nattie E (2006). Catecholamine neurones in rats modulate sleep, breathing, central chemoreception and breathing variability. *Journal of Physiology* **570**, 385–396.
- Maljevic S, Wuttke T V. & Lerche H (2008). Nervous system KV7 disorders: breakdown of a subthreshold brake. *J Physiol* **586**, 1791–1801.
- Marchenko V, Koizumi H, Mosher B, Koshiya N, Tariq MF, Bezdudnaya TG, Zhang R, Molkov YI, Rybak IA & Smith JC (2016). Perturbations of respiratory rhythm and pattern by disrupting synaptic inhibition within pre-Bötzing and Bötzing complexes. *eNeuro* **3**, 3033–3046.
- Montandon G, Liu H & Horner RL (2016a). Contribution of the respiratory network to rhythm and motor output revealed by modulation of GIRK channels, somatostatin and neurokinin-1 receptors. *Sci Rep*; DOI: 10.1038/SREP32707.
- Montandon G, Qin W, Liu H, Ren J, Greer JJ & Horner RL (2011). PreBötzing Complex Neurokinin-1 Receptor-Expressing Neurons Mediate Opioid-Induced Respiratory Depression. *The Journal of Neuroscience* **31**, 1292.
- Montandon G, Ren J, Victoria NC, Liu H, Wickman K, Greer JJ & Horner RL (2016b). G-protein-gated inwardly rectifying potassium channels modulate respiratory depression by opioids. *Anesthesiology* **124**, 641.
- Mortola JP & Frappell PB (1998). On the barometric method for measurements of ventilation, and its use in small animals. *Can J Physiol Pharmacol* **76**, 937–944.
- National Research Council (2011). *Guide for the Care and Use of Laboratory Animals*. National Academies Press (US), Washington (DC). Available at: <https://www.ncbi.nlm.nih.gov/books/NBK54050/> [Accessed July 31, 2022].
- Del Negro CA, Funk GD & Feldman JL (2018). Breathing matters. *Neuroscience* **19**, 351–367.

Del Negro CA, Kam K, Hayes JA & Feldman JL (2009). Asymmetric control of inspiratory and expiratory phases by excitability in the respiratory network of neonatal mice in vitro. *J Physiol* **587**, 1217.

Del Negro CA, Koshiya N, Butera RJ & Smith JC (2002a). Persistent sodium current, membrane properties and bursting behavior of pre-Bötzinger complex inspiratory neurons in vitro. *J Neurophysiol* **88**, 2242–2250.

Del Negro CA, Morgado-Valle C & Feldman JL (2002b). Respiratory rhythm: an emergent network property? *Neuron* **34**, 821–830.

Del Negro CA, Morgado-Valle C, Hayes JA, Mackay DD, Pace RW, Crowder EA & Feldman JL (2005). Sodium and calcium current-mediated pacemaker neurons and respiratory rhythm generation. *Journal of Neuroscience* **25**, 446–453.

Del Negro CA, Wilson CG, Butera RJ, Rigatto H & Smith JC (2002c). Periodicity, Mixed-Mode Oscillations, and Quasiperiodicity in a Rhythm-Generating Neural Network. *Biophys J* **82**, 206–214.

Northcutt AJ & Schulz DJ (2020). Molecular mechanisms of homeostatic plasticity in central pattern generator networks. *Dev Neurobiol* **80**, 58–69.

Pace RW, Mackay DD, Feldman JL & Del Negro CA (2007). Role of persistent sodium current in mouse preBötzinger Complex neurons and respiratory rhythm generation. *Journal of Physiology* **580**, 485–496.

Patrone LGA, Biancardi V, Marques DA, Bicego KC & Gargaglioni LH (2018). Brainstem catecholaminergic neurones and breathing control during postnatal development in male and female rats. *J Physiol* **596**, 3299–3325.

Paxinos G & Franklin KBJ (2019). *Paxinos and Franklin's the Mouse Brain in Stereotaxic Coordinates*, 5th edn. Academic Press. Available at: <https://www.elsevier.com/books/paxinos-and-franklins-the-mouse-brain-in-stereotaxic-coordinates-compact/franklin/978-0-12-816159-3> [Accessed October 26, 2021].

Peretz A, Sheinin A, Yue C, Degani-Katzav N, Gibor G, Nachman R, Gopin A, Tam E, Shabat D, Yaari Y & Attali B (2007). Pre- and postsynaptic activation of M-channels by a novel opener dampens neuronal firing and transmitter release. *J Neurophysiol* **97**, 283–295.

Phillips RS & Baertsch NA (2024). Interdependence of cellular and network properties in respiratory rhythm generation. *Proc Natl Acad Sci U S A* **121**, 2318757121.

Picardo MCD, Sugimura YK, Dorst KE, Kallurkar PS, Akins VT, Ma X, Teruyama R, Guinamard R, Kam K, Saha MS & Negro CA Del (2019). Trpm4 ion channels

in pre-Böttinger complex interneurons are essential for breathing motor pattern but not rhythm. *PLoS Biol*; DOI: 10.1371/JOURNAL.PBIO.2006094.

Ptak K, Yamanishi T, Aungst J, Milescu LS, Zhang R, Richerson GB & Smith JC (2009). Raphe neurons stimulate respiratory circuit activity by multiple mechanisms via endogenously released serotonin and substance p. *Journal of Neuroscience* **29**, 3720–3737.

Ramirez JM & Baertsch N (2018a). Defining the Rhythmogenic Elements of Mammalian Breathing. *Physiology* **33**, 302.

Ramirez JM & Baertsch NA (2018b). The Dynamic Basis of Respiratory Rhythm Generation: One Breath at a Time. *Annu Rev Neurosci* **41**, 475.

Ramirez JM, Burgraff NJ, Wei AD, Baertsch NA, Varga AG, Baghdoyan HA, Lydic R, Morris KF, Bolser DC & Levitt ES (2021). Neuronal mechanisms underlying opioid-induced respiratory depression: our current understanding. *J Neurophysiol* **125**, 1899–1919.

Raurich JM, Ibañez J & Marse P (1989). Validation of a new closed circuit indirect calorimetry method compared with the open Douglas bag method. *Intensive Care Med* **15**, 274–278.

Revill AL, Katzell A, Del Negro CA, Milsom WK & Funk GD (2021). KCNQ Current Contributes to Inspiratory Burst Termination in the Pre-Böttinger Complex of Neonatal Rats in vitro. *Front Physiol* **12**, 626470.

Richter DW, Ballanyi K & Schwarzacher S (1992). Mechanisms of respiratory rhythm generation. *Curr Opin Neurobiol* **2**, 788–793.

Robbins J (2001). KCNQ potassium channels: physiology, pathophysiology, and pharmacology. *Pharmacol Ther* **90**, 1–19.

Rogawski MA & Bazil CW (2008). New Molecular Targets for Antiepileptic Drugs: $\alpha 2\delta$, SV2A, and Kv7/KCNQ/M Potassium Channels. *Curr Neurol Neurosci Rep* **8**, 345.

Rubin JE, Shevtsova NA, Bard Ermentrout G, Smith JC & Rybak IA (2009). Multiple Rhythmic States in a Model of the Respiratory Central Pattern Generator. *J Neurophysiol* **101**, 2146.

Schenzer A, Friedrich T, Pusch M, Saftig P, Jentsch TJ, Grötzinger J & Schwake M (2005). Molecular Determinants of KCNQ (Kv7) K⁺ Channel Sensitivity to the Anticonvulsant Retigabine. *Journal of Neuroscience* **25**, 5051–5060.

Schindelin J, Arganda-Carreras I, Frise E, Kaynig V, Longair M, Pietzsch T, Preibisch S, Rueden C, Saalfeld S, Schmid B, Tinevez JY, White DJ, Hartenstein

V, Eliceiri K, Tomancak P & Cardona A (2012). Fiji - an Open Source platform for biological image analysis. *Nat Methods* **9**, 676–682.

Sherman D, Worrell JW, Cui Y & Feldman JL (2015). Optogenetic perturbation of preBötzing Complex inhibitory neurons modulates respiratory pattern. *Nat Neurosci* **18**, 408.

da Silva CA, Grover CJ, Picardo MCD & Del Negro CA (2023). Role of NaV1.6-mediated persistent sodium current and bursting-pacemaker properties in breathing rhythm generation. *Cell Rep*; DOI: 10.1016/j.celrep.2023.113000.

Smith JC, Abdala APL, Koizumi H, Rybak IA & Paton JFR (2007). Spatial and Functional Architecture of the Mammalian Brain Stem Respiratory Network: A Hierarchy of Three Oscillatory Mechanisms. *J Neurophysiol* **98**, 3370–3387.

Smith JC, Ellenberger HH, Ballanyi K, Richter DW & Feldman JL (1991). Pre-Bötzing complex: a brainstem region that may generate respiratory rhythm in mammals. *Science* **254**, 726–729.

Springer K, Varghese N & Tzingounis A V. (2021). Flexible stoichiometry: implications for KCNQ2 and KCNQ3 associated neurodevelopmental disorders. *Dev Neurosci* **43**, 191.

Stuart DG & Hultborn H (2008). Thomas Graham Brown (1882--1965), Anders Lundberg (1920-), and the neural control of stepping. *Brain Res Rev* **59**, 74–95.

Tulppo MP, Mäkikallio TH, Takala TES, Seppänen T & Huikuri H V. (1996). Quantitative beat-to-beat analysis of heart rate dynamics during exercise. *Am J Physiol*; DOI: 10.1152/AJPHEART.1996.271.1.H244.

Tykocki NR, Heppner TJ, Dalsgaard T, Bonev AD & Nelson MT (2019). The K V 7 channel activator retigabine suppresses mouse urinary bladder afferent nerve activity without affecting detrusor smooth muscle K + channel currents. *Journal of Physiology* **597**, 935–950.

Vann NC, Pham FD, Dorst KE & Del Negro CA (2018). Dbx1 Pre-Bötzing Complex Interneurons Comprise the Core Inspiratory Oscillator for Breathing in Unanesthetized Adult Mice. *eNeuro*; DOI: 10.1523/ENEURO.0130-18.2018.

Vervaeke K, Gu N, Agdestein C, Hu H & Storm JF (2006). Kv7/KCNQ/M-channels in rat glutamatergic hippocampal axons and their role in regulation of excitability and transmitter release. *J Physiol* **576**, 235.

Wallén-Mackenzie Å, Gezelius H, Thoby-Brisson M, Nygård A, Enjin A, Fujiyama F, Fortin G & Kullander K (2006). Vesicular glutamate transporter 2 is required for central respiratory rhythm generation but not for locomotor central pattern generation. *Journal of Neuroscience* **26**, 12294–12307.

Wang JJ & Li Y (2016). KCNQ potassium channels in sensory system and neural circuits. *Acta Pharmacol Sin* **37**, 25.

Wang X, Hayes JA, Revill AL, Song H, Kottick A, Vann NC, LaMar MD, Picardo MCD, Akins VT, Funk GD & Del Negro CA (2014). Laser ablation of Dbx1 neurons in the pre-Bötzinger complex stops inspiratory rhythm and impairs output in neonatal mice. *Elife* **3**, e03427.

Watanabe H, Nagata E, Kosakai A, Nakamura M, Yokoyama M, Tanaka K & Sasai H (2000). Disruption of the epilepsy KCNQ2 gene results in neural hyperexcitability. *J Neurochem* **75**, 28–33.

Wei AD & Ramirez JM (2019). Presynaptic Mechanisms and KCNQ Potassium Channels Modulate Opioid Depression of Respiratory Drive. *Front Physiol* **10**, 1407.

Yamanishi T, Koizumi H, Navarro MA, Milescu LS & Smith JC (2018). Kinetic properties of persistent Na⁺ current orchestrate oscillatory bursting in respiratory neurons. *J Gen Physiol* **150**, 1523–1540.

Zamponi GW & Currie KPM (2013). Regulation of CaV2 calcium channels by G protein coupled receptors. *Biochim Biophys Acta* **1828**, 1629.

VITA

Carlos Aparecido da Silva Junior was born on March 20th, 1995, in Serrana, São Paulo, Brazil. He received a Teaching Degree (Licentiate) and a Bachelor in Biological Science from the São Paulo State University, in 2016 and 2017, respectively. He was recognized twice as the best ranked student of his graduation class. Later, he started his master program in Physiological Sciences at the Federal University of São Carlos in partnership with São Paulo State University, in the Interinstitutional Graduate Program in Physiological Sciences. He completed his master in August 2020. In parallel, he worked as a science teacher for public, private, and vocational schools. While as a master student, he was granted an international fellowship from the São Paulo Research Foundation and developed a 6-month project in Christopher Del Negro's lab, at William & Mary, Williamsburg, VA, in 2019. After concluding his studies in Brazil, he began his doctoral program in the Department of Applied Science in Fall 2020 under the supervision of Christopher A. Del Negro. Concurrently, he taught Human Anatomy & Physiology classes at Christopher Newport University, Newport News, VA. His research has focused on the neural control of breathing, studying the exogenous factors that influence the normal development of the respiratory network, the underlying ion channel mechanisms for inspiratory rhythm generation, as well the mechanisms for inspiratory burst termination.

Publications

da Silva Junior, C.A., Grover, C.J., Picardo, M.C.D., Del Negro, C.A. (2023). Role of Na_v1.6-mediated persistent sodium current and bursting-pacemaker properties in breathing rhythm generation. *Cell Reports*, 42. <https://10.1016/j.celrep.2023.113000>.

da Silva Junior, C.A., Marques, D.A., Patrone, L.G.A., Biancardi, V., Bicego, K.C., Gargaglioni, L.H. (2023). Intra-uterine diazepam exposure decreases the number of catecholaminergic and serotonergic neurons of neonate rats. *Neuroscience letters*, 795. <https://doi.org/10.1016/j.neulet.2022.137014>.

da Silva Junior, C.A., Patrone, L.G.A., Biancardi, V., Vilela-Costa, H.H., Marques, D.A., Cristina-Silva, C., da Costa Silva, K.S., Bicego, K.C., Szawka, R.E., Gargaglioni, L.H. (2022). Sexually dimorphic effects of prenatal diazepam exposure on respiratory control and the monoaminergic system of neonate and young rats. *Pflugers Arch.* 474 (11), 1185-1200. <https://doi.org/10.1007/s00424-022-02730-7>.

da Silva Junior, C.A., Picardo, M.C., Del Negro, C. (2022). RNA interference via shRNA decreases the number of transcripts of *Scn8a* in glutamatergic interneurons in the preBötC. *The FASEB Journal*, 36. <https://doi.org/10.1096/fasebj.2022.36.S1.R2948>.

da Silva Junior, C.A., Biancardi, V., Patrone, L.G.A., Bicego, K.C. and Gargaglioni, L.H. (2020). Intra-uterine exposure to Diazepam decrease the ventilatory response and impairs the motor behavior of males and females at post-natal life. *The FASEB Journal*, 34. <https://doi.org/10.1096/fasebj.2020.34.s1.06981>.

Leirão, I. P., **Silva, C. A. Jr**, Gargaglioni, L. H., da Silva, G. (2018). Hypercapnia-induced active expiration increases in sleep and enhances ventilation in unanaesthetized rats. *The Journal of Physiology*, 596 (15), 3271–3283. <https://doi.org/10.1113/JP274726>.

Augusto, T. G. da S., **Silva Junior, C. A.** (2020). A trajetória do sangue no corpo humano: a história da ciência na formação continuada de professores de biologia. [EN: The path of blood in the human body: history of science in the training of in-service biology teachers]. *Revista Brasileira de História Da Ciência*, 13 (2), p. 250-260. <https://doi.org/10.53727/rbhc.v13i2.37>.

Silva, C. A., Vicente, M. C., Tenorio-Lopes, L., Soliz, J., Gargaglioni, L. H. (2017). Erythropoietin in the Locus coeruleus attenuates the ventilatory response to CO₂ in rats. *Respiratory physiology & neurobiology*, 236, 11–18. <https://doi.org/10.1016/j.resp.2016.10.011>.

da Silva Junior, C. A., G. da S. A. Thaís. (2017). História Das Ideias Sobre circulação sanguínea: Concepções De Professores De Biologia. [EN: The history of the Blood Circulation: Conceptions of Biology Teachers]. *Enseñanza De Las Ciencias: Revista De investigación Y Experiencias didácticas*, Extra, 3007-12. <https://raco.cat/index.php/Ensenanza/article/view/339797>